



Group of Electronics and
Instrumentation

IMPEDANCE CARDIOGRAPHY

Dissertation presented to the University of Coimbra in order to complete the necessary requirements to obtain the Master's degree in Biomedical Engineering.

CANDIDATE

Name Neide Carina Simões Capela

Student number 2008113669

PROJECT COORDINATION

Advisor PhD Professor Carlos M. B. A. Correia

Co-Advisor PhD João Manuel Rendeiro Cardoso

Technical supervisor MsC Elisabeth Sofia Borges Ferreira

Physics Department
Faculty of Sciences and Technology
University of Coimbra

Coimbra, September 2013

Aos meus avós,

Basílio Simões e Maria do Céu Miguéis.

(2013)

Acknowledgments

I would like to express my gratitude to the GEI team for their guidance and the knowledge base provided, of whom I must name Prof. Dr. Carlos Correia, Prof. Dr. Requicha Ferreira, Dr. João Cardoso, Eng. Elisabeth Borges, Eng. Vânia Almeida, Eng. Mariana Sequeira, Eng. Pedro Santos and Eng. Pedro Vaz. Mentioning a special thanks to Prof. Carlos Correia for the help provided throughout this project.

Also, I thank my good old friends that were an active part of the adaptation during the first years in the city of Coimbra, impelling me to continue.

The last but definitely not the least, I must acknowledge my deepest gratitude to my family: my parents and grandparents for all the sacrifices they made to support me over the last five years, helping me whenever they could and my aunts – not all of them present at this time - for all the patience.

Abstract

The development of diagnostic technics for early detection of cardiovascular risk factors allows the anticipated treatment of the cardiac diseases, increasing the survival probability. The cardiac output monitoring by invasive methods have been one standard criterion for the evaluation of hemodynamics. In this context, the Impedance Cardiography technic appears as a simple, non-invasive and cost-effective alternative to monitor relative changes in the cardiac output, as well systolic time intervals.

An Impedance Cardiography system prototype was developed based on the AD5933-integrated impedance meter, adapted to perform in a tetrapolar electrode configuration while allowing the injection of a safe excitation current into the subject and sensing the voltage differential generated to assess the thoracic impedance value. The synchronous Electrocardiogram register was also tested. For the control of the system operation the firmware running on an Arduino® microcontroller board and the graphical user interface based on Matlab® were developed.

The results of the system performance evaluation, including the validation tests performed on volunteers to assess relevant physiological parameters are presented, as well as the abbreviated signal analysis methodology applied.

Keywords

Electrical bioimpedance, Impedance Cardiography, Cardiac Output, AD5933, Arduino.

Resumo

O desenvolvimento de técnicas de diagnóstico para detecção prematura de fatores de risco cardiovascular permite o tratamento antecipado das doenças cardíacas, aumentando a probabilidade de sobrevivência. A monitorização do débito cardíaco com base em métodos invasivos tem sido um padrão para avaliação hemodinâmica. Neste contexto, a técnica de Cardiografia de Impedância surge como uma alternativa simples, não-invasiva e de baixo custo que permite monitorizar variações do débito cardíaco, assim como determinar os tempos sistólicos.

Foi desenvolvido um protótipo para realização de Cardiografia de Impedância baseado num impedancímetro integrado, o AD5933, adaptando-o para operar numa configuração tetrapolar, de modo a injetar uma corrente de excitação controlada no sujeito e medir a diferença de potencial elétrico gerada, para obter o valor de impedância torácica. A recolha paralela do sinal de Eletrocardiograma foi também testada. Para controlar a operação do sistema foram desenvolvidos o *firmware*, que corre numa placa Arduino®, e a interface gráfica baseada em Matlab®.

São apresentados os resultados da avaliação de performance do sistema, incluindo os testes de validação realizados em voluntários para obter parâmetros com relevância fisiológica, assim como a descrição da metodologia aplicada à análise dos sinais recolhidos.

Palavras-chave

Bioimpedância elétrica, Cardiografia de impedância, Débito cardíaco, AD5933, Arduino.

Contents

Acknowledgments.....	i
Abstract	iii
Resumo.....	v
Contents	vii
List of Figures	xi
List of Tables.....	xv
Acronyms.....	xix
Chapter 1: Introduction.....	1
1.1. Introduction.....	2
1.2. Motivation.....	2
1.3. Goals.....	3
1.4. Thesis content	3
Chapter 2: Theoretical Background	5
2.1. Circulatory system overview	6
2.1.1. Systolic times.....	7
2.1.2. Cardiac output.....	7
2.2. Electrical properties of biological tissues.....	8
2.3. Electrocardiogram	9
2.4. Impedance Cardiography	10
2.4.1. Current limits.....	11
2.5. Measurement methods.....	12
2.5.1. Electrodes: type and topography	13
2.5.1.1. Anteroposterior configuration	14
2.5.1.2. Posterolateral configuration	14
2.5.1.3. Electrode polarity.....	15
2.5.2. Electrode-Skin interface	15
2.6. Source of the ICG signal	16
2.6.1. Simplified model of the human thorax	17
2.6.2. Method for stroke volume calculation.....	18
2.6.2.1. Blood resistivity value	18
2.7. Impedance Cardiography signal analysis	19
2.7.1. Characteristic points and periods.....	20
2.7.2. Hemodynamic parameters.....	22
Chapter 3: Phantom Setup.....	23
3.1. Materials and methods	24
3.1.1. Electing the materials.....	24
3.1.2. Phantom models and Practical limitations	26
3.1.3. Final formulation	27
3.2. Results and discussion.....	32
Chapter 4: Impedance Cardiography Acquisition System.....	37
4.1. Hardware.....	38
4.1.1. Arduino® Mega 2560 – microcontroller board	39

4.1.2.	Impedance meter unit.....	39
4.1.2.1.	AD5933 - Integrated impedance analyzer	40
4.1.2.1.1.	Calibration procedure and impedance calculation	42
4.1.2.1.2.	Operation parameters.....	43
4.1.2.2.	Signal conditioning circuit	43
4.1.2.2.1.	Calibration procedure revised and impedance calculation	46
4.1.2.2.2.	Calibration procedure assumptions and limitations.....	49
4.1.3.	ECG unit.....	51
4.1.3.1.	ECG calibration method	52
4.1.4.	Electrode construction	52
4.1.5.	Printed Circuit Board Specifications.....	54
4.2.	Firmware	54
4.3.	Software	57
Chapter 5: System Evaluation		61
5.1.	Current source evaluation.....	62
5.2.	AC and DC performance and security limits.....	66
5.3.	Calibration procedure evaluation	69
5.3.1.	Automated calibration procedure.....	74
5.3.2.	System measurement limits and errors	74
5.4.	ECG time delay	75
Chapter 6: Validation Tests		79
6.1.	Methodology	80
6.1.1.	Data Acquisition protocol.....	80
6.1.2.	Signal-to-noise ratio	81
6.1.3.	Signal pre-processing	82
6.1.4.	QRS detection.....	83
6.1.5.	Wave segmentation and Ensemble average	85
6.1.6.	Feature extraction	86
6.1.7.	Assessment of Hemodynamic Parameters	86
6.2.	Results and discussion.....	87
6.2.1.	Signal-to-Noise Ratio	88
6.2.2.	Thoracic impedance signal	91
6.2.2.1.	ECG/ICG crosstalk influence.....	96
6.2.3.	Impedance Cardiography signals and hemodynamic parameters.....	97
Chapter 7: Conclusions and Future Work		101
7.1.	General conclusions	102
7.2.	Future work	102
Bibliographic References.....		105
Appendix A: Reference Values for Thoracic Impedance.....		113
Appendix B: Reference values for Hemodynamic Parameters.....		115
Appendix C: Circuit Schematics		117
Appendix D: Current evaluation on board		121
Appendix E: Calibration model fitting curves		123
Appendix F: Uncertainties of the automated calibration procedure.....		125
Appendix G: Relevant parameters from the signal analysis and respective uncertainties ...		129

Appendix H:	Impedance data resume from simultaneous acquisitions of impedance and ECG	131
Appendix I:	Averaged ICG waves	137

List of Figures

Figure 1) Human heart chambers and valves [6] and aorta detail [7].	6
Figure 2) Heart cycle [8].	6
Figure 3) Equivalent electrical circuit for biological tissues. Adapted from [17].	9
Figure 4) ECG signal showing the characteristic points and waves in one cardiac cycle [19].	10
Figure 5) Permissible AC-current (peak-to-peak values) through the human body in accordance to the Standard EN60601 for medical devices. Extracted from [17].	11
Figure 6) Bipolar configuration, equivalent circuit and impedance mathematical description. The blocks represent complex impedances.	12
Figure 7) Tetrapolar configuration, equivalent circuit and impedance mathematical description.	13
Figure 8) Kubicek band electrode system.	13
Figure 9) Tetrapolar electrode configuration from Qu et al.	14
Figure 10) Tetrapolar electrode configuration from Penney et. al.	15
Figure 11) Electrode-skin interface circuit for the typical spot electrode. Adapted from [17].	16
Figure 12) Parallel conductor model for the human thorax impedance, with uniform blood and tissue compartments with crosssectional areas A_b and A_l , respectively and constant length L . Extracted from [13].	17
Figure 13) Influence of breathing on the thoracic impedance [52].	20
Figure 14) ICG typical waves (ΔZ , dZ/dt presented in the upward direction) and ECG reference signal. Adapted from [13].	21
Figure 15) Agar-agar cylindrical masses (1)/(3) and molds (2) used to cut them ($\varnothing=6.63$ cm, 5.59 cm, 5 cm and 4.02 cm, from left to right).	28
Figure 16) Set up for measuring the impedance (left) of 20 ml samples of solution and agar-agar inside PP containers (right): (1) holder claw, (2) EIS system grip and (3) needle electrodes. (Mean $d_e=3.71$ cm and ~ 0.5 cm from the point of contact with the grip to the electrode top.)	28
Figure 17) Agar-Agar impedance evaluation on 20 mL samples: Average values from two phantoms with similar formulations. The error bars reflect the standard error of the mean.	29
Figure 18) Aqueous solution impedance evaluation on 20 mL samples: Average values based on samples taken from two phantoms with similar formulations. The error bars reflect the standard error of the mean.	30
Figure 19) EIS system and experimental set-up: (1) laptop running a Matlab® based user interface for data processing; (2) PicoScope® acquisition interface and signal conditioning unit of the EIS system with electrode grips to grab the needle electrodes in contact with the samples; (3) Phantom.	31
Figure 20) Detail of the phantom setup: central mass of agar surrounded by the aqueous solution. The needle electrodes are held beneath the marks location on the bottom of the container.	31
Figure 21) Impedance evaluation on individual agar-agar volumes from phantom 1: Resistance (left) and reactance (right) as a function of the excitatory frequency. The distances between the electrodes during the measurements where: 3.54 cm, 4.4 cm, 4.95 cm, 6.21 cm for v_1 , v_2 , v_3 and v_4 , respectively.	33
Figure 22) Impedance evaluation on individual agar-agar volumes from phantom 2: Resistance (left) and reactance (right) as a function of the excitatory frequency. The distances between the electrodes during the measurements where: 3.5 cm, 4.41 cm, 5.01 cm, 6.15 cm for v_1 , v_2 , v_3 and v_4 , respectively.	34

Figure 23) Phantom resistance as a function of the conductive volume for measurements after adjustment of the liquid volume (left) and with the total liquid content of approximate 250 mL (right). Each label indicates the resistance value at 70 kHz.	34
Figure 24) Phantom reactance as a function of the conductive volume for measurements after adjustment of the liquid volume (left) and with the total liquid content of approximate 250 mL (right).	35
Figure 25) ICG system: simplified functional diagram describing the information flow between software, firmware and hardware.	38
Figure 26) Arduino® Mega 2560 board relevant components.....	39
Figure 27) AD5933 simplified functional block diagram depicting its basic operation configuration.	40
Figure 28) Signal conditioning circuit. Current injection and voltage sensing electrodes are presented in green and blue, respectively.	44
Figure 29) Simplified impedance unit with relevant quantities and simplified presentation of stray components equivalent (Z_e).	47
Figure 30) Equivalent electric circuit of all parasitic impedance components affecting the thoracic impedance measurement (Z_{chest}) [58, 66]: Z_{cables} corresponds to the effect of the electrode cables; Z_{e-s} is the electrode-skin interface impedance; Z_{tissue} represents the tissue in between the application and sensing electrodes.	50
Figure 31) ECG front-end [82] and the 3-lead ECG configuration.....	52
Figure 32) ICG (left) and ECG (right) electrode components: (1) plug for connection with the device, (2) plug for connection with the subject and (3) plug adapter for clip electrodes.	53
Figure 33) Pre-gelled disposable electrodes for ECG.	53
Figure 34) PCB board (middle) mounted on a test platform with voltage converting module (left), showing the frontal panel with sockets to connect the electrodes and the Arduino® board on the PCB back, and multichannel platform (right).	54
Figure 35) Process diagram for the firmware operation.....	56
Figure 36) Graphic User Interface after a measurement presenting the raw impedance and the ECG signals and the pre-visualization of pre-processed data: respiratory impedance, cardiac impedance, base impedance, ICG signal and ECG.	57
Figure 37) Graphic interface after acquisition of calibration data.....	59
Figure 38) Voltage controlled current source (OPA860) basic configuration. B represents the base where an AC voltage is injected, E is the emitter where the current output is defined by the resistor R_E and C is the collector where the current output is delivered to the load resistor (R_{load}).	62
Figure 39) VCCS: current amplitude variation with the load resistance value. The vertical line represents $R_{load}=388 \Omega$. The statistic values consider only the stable region to the right of 388Ω	63
Figure 40) VCCS: DC bias variation with the load resistance value. The vertical line represents $R_{load}=388 \Omega$. The statistic values consider only the stable region to the right of 388Ω	64
Figure 41) VCCS: internal resistance variation with the load resistance value. The vertical line represents $R_{load}=388 \Omega$. For $R_{load}<388 \Omega$ the internal resistance is presented in module (absolute value). The statistic values consider only the stable region to the right of 388Ω	65
Figure 42) PCB: current amplitude through the grounded resistor of 390Ω	67
Figure 43) PCB: DC bias through the grounded resistor of 390Ω	67
Figure 44) PCB: Current amplitude as a result of applying the Ohm's law to the AD8220 output voltage and the actual load resistor value.	69
Figure 45) Variation of non-calibrated amplitude (left) and phase - system phase - (right) with the test resistor value.....	70

Figure 46) Variation of amplitude gain factor (left) and system phase (right) with the non-calibrated amplitude value.....	72
Figure 47) ECG front-end block diagram [82]: only components that are considered to introduce delay are identified. The delay evaluation was made in the identified test points.....	76
Figure 48) Low pass filter circuit simulated using Orcad® (left) and graphical representation of the input and output voltage over 1 s (right). The blue circle indicates the zero crossings where the delay was evaluated.....	76
Figure 49) Normalized notch filter input signal and ECG front-end output. The lack of synchronization between the ECG peaks in both signal is visible despite the noise (related to the antenna effect from the direct measurement).....	77
Figure 50) Pre-processing.....	82
Figure 51) QRS detection algorithm steps (based on the Pan and Tompkins algorithm). Band-pass filtering: removes interferences; Derivative filtering: enhances peaks; SquaringxSquaring: turns the signal positive and reinforces the peaks in a non-linear way; Moving window integration: merges nearby peaks.	84
Figure 52) Ensemble average: ICG beats segmented by the R-ECG peak and averaged ΔZ , ICG and ECG signals over N beats.	85
Figure 53) Feature extraction panel with relevant points on the ICG averaged signal. The ΔZ and ECG, normalized to the ICG maximum amplitude, were only used as references to correctly identify the characteristic points.	86
Figure 54) ECG signal without pre-processing and noise level obtained with the electrodes unplugged. The DC-level is not relevant in either case. The signal was acquired on subject #3 at a sampling frequency of 400 Hz.	89
Figure 55) ECG signal's power spectrum in dB, after removing the irrelevant baseline.	89
Figure 56) Impedance signal without pre-processing and noise level obtained by applying a stop-band filter to the signal frequencies. The DC level is relevant in the impedance case. The signal was acquired at a sampling frequency of 400 Hz, using the anteroposterior configuration, without the ECG parallel acquisition, while applying an excitatory AC current with a frequency of 50 kHz on subject #3.....	90
Figure 57) Impedance signal's power spectrum in dB.	90
Figure 58) Cardiac impedance de-noised signals: impedance (ΔZ_c) and ICG (dZ_c/dt).	93
Figure 59) Respiratory impedance amplitude.....	95
Figure 60) Impedance cardiography signals (cardiac impedance, ICG) and ECG. Results from both electrode configurations while applying an excitatory AC current with frequency of 50 and 100 kHz, respectively.....	98
Figure 61) Signal conditioning circuit schematic. All the resistor values are in units of ohm (Ω) and the capacitors in farads (F).	117
Figure 62) AD8220 reference generation circuit. The resistors values are presented in units of ohm (Ω) and the capacitors values are in farad (F).	118
Figure 63) ECG front-end circuit scheme [82], directly extracted from the producers web page. The squares represent test points (T1, T2, T3).....	119
Figure 64) PCB: Current amplitude through the path to the ground on the DC blocking capacitor output.....	121
Figure 65) PCB: DC bias current through the path to the ground on the DC blocking capacitor output.....	121
Figure 66) Gain factor at 50, 70 and 100 kHz: fitting results from Eureka mathematical software (left) and the relation between the real gain factor and the result from the model (right).The mathematical expression for each frequency is presented.	123
Figure 67) System phase at 50, 70 and 100 kHz: fitting results from Eureka mathematical software (left) and the relation between the real gain factor and the result from the	

	mode (right).The mathematical model for each frequency is presented and are defined in radians.	124
Figure 68)	Averaged ICG waves based on the impedance amplitude, for different configurations and different frequencies of the excitatory AC current applied on subject #1.	138
Figure 69)	Averaged ICG waves based on the impedance amplitude, for different configurations and different frequencies of the excitatory AC current applied on subject #2.	139
Figure 70)	Averaged ICG waves based on the impedance amplitude, for different configurations and different frequencies of the excitatory AC current applied on subject #3.	140

List of Tables

Table 1) Effects of the DC current in the human body. Extracted from [22].	12
Table 2) Characteristic points on the ICG signal [4].	21
Table 3) Characteristic periods in ICG [4].	22
Table 4) Hemodynamic parameters [4].	22
Table 5) Idealized phantom models	26
Table 6) Phantoms volumetric description: the volumes of aqueous solution and agar-agar are indicated.	30
Table 7) Impedance properties of the aqueous solution alone on the phantom container, at the beginning and at the end of the measurements. The uncertainties reflect the standard error of the mean.	33
Table 8) Corrected phase angles [62].	42
Table 9) AD5933 operation parameters – typical values.	43
Table 10) Test resistor (R_{load}) values for evaluation of the current source. The values cover all the working range of the current source.	62
Table 11) Signal generator output characteristics: frequency (F), peak-to-peak voltage (V_{p-p}) and DC offset (V_{DC}). Average values on the input B from each the measurement performed on the test resistors. The error is evaluated in terms of the standard error of the mean.	62
Table 12) Test resistor (R_{load}) values. These resistors cover the full impedance measurement of the system.	66
Table 13) VCCS voltage input characteristics on board: Frequency (F), peak-to-peak voltage (V_{p-p}) and DC offset (V_{DC}). Average values from each measurement performed on the test resistors. The error is evaluated in terms of the standard error of the mean.	66
Table 14) RRC circuit for testing purposes and impedance characteristics.	70
Table 15) Absolute errors from the evaluation of the calibration parameters on test data from the same resistors: Average values from all the resistances at the same frequency. ...	71
Table 16) Average impedance values measured on the RRC test circuit obtained with a calibration resistance of 24.8Ω and relative absolute errors (Δ).	71
Table 17) Absolute errors from the evaluation of the calibration model on the test resistors: average values from all the resistances at the same frequency.	73
Table 18) Average impedance values from the RRC test circuit obtained from calibration parameters based on the calibration algorithm models and relative absolute errors (Δ).	73
Table 19) Summary of system capabilities.	75
Table 20) QRS detection algorithm's performance.	85
Table 21) Subject data summary. The heart rate values presented are only indicative values, since they were not monitored throughout the long acquisition periods.	88
Table 22) ECG system's SNR. The presented value results from averaging the results of two acquisitions.	89
Table 23) Impedance system's SNR. The presented values result in each case from averaging the values of two acquisitions.	91
Table 24) Thoracic impedance average (Z_0) values from the calibrated curves obtained from two acquisitions at each frequency.	91
Table 25) Peak-to-peak values of the de-noised cardiac impedance component (ΔZ_c) obtained from the thoracic impedance curves. The uncertainties were estimated using the standard error of the mean.	93
Table 26) Maximum peak value of the first derivative of the cardiac impedance component (ICG). The uncertainties were estimated using the standard error of the mean.	94

Table 27) Peak-to-peak values of the de-noised respiratory impedance component (ΔZ_r) obtained from the thoracic impedance curves. The uncertainties were estimated using the standard error of the mean.	95
Table 28) Effect of the ECG/ICG crosstalk: mean absolute error and maximum error percentage introduced. The results were evaluated on the average of two acquisitions at each frequency for each configuration studied.....	97
Table 29) Average impedance values for the same electrode configuration, employed to calculate the hemodynamic parameters. The uncertainties are evaluated in terms of the standard error of the mean.	99
Table 30) Average hemodynamic parameters for the same electrode configuration. The uncertainties are evaluated in terms of the standard error of the mean.....	99
Table 31) Thoracic impedance typical values: compilation from several sources.....	113
Table 32) Hemodynamic parameters reference values compilation [94, 102] and interval of reported values while sitting [97, 98].	115
Table 33) Data set resume: average calibrated reference values from two data sets and standard error of the mean.....	125
Table 34) Maximum discrepancy of the data calibrated using the simulated 10 second period influence of $\pm 2\%$ on the raw amplitude relative to the reference amplitude and phase.	126
Table 35) Maximum discrepancy between the maximum raw values of the data set calibrated using maximum raw amplitude and those same values calibrated using the mean raw amplitude. Also the 10 second period influence of $\pm 2\%$ of the raw amplitude was simulated in both cases and compared.....	126
Table 36) Maximum discrepancy between the minimum raw values of the data set calibrated using minimum raw amplitude and those same values calibrated using the mean raw amplitude. Also the 10 second period influence of $\pm 2\%$ of the raw amplitude was simulated in both cases and compared.....	126
Table 37) Maximum overall discrepancy detected by studding the effect of a single pair of calibration values based on a 10 second period. This table resumes the last three tables.	126
Table 38) Hemodynamic parameters and resume of relevant values for their calculation, with the associated uncertainties.	129
Table 39) Thoracic impedance average (Z_0) values obtained from two acquisitions at each frequency for the <u>anteroposterior configuration</u> . The uncertainties for the amplitude and phase are the constants determined on section 5.3.2, in the case of the real and imaginary values an error propagation was performed.	131
Table 40) Peak-to-peak values of the de-noised cardiac impedance component (ΔZ_c) obtained from the thoracic impedance signal for the <u>anteroposterior configuration</u> . The uncertainties were estimated from the standard error of the mean.	131
Table 41) Peak-to-peak values of the de-noised respiratory impedance component (ΔZ_r) obtained from the thoracic impedance waves for the <u>anteroposterior configuration</u> . The uncertainties were estimated from the standard error of the mean.	132
Table 42) Values used to calculate the hemodynamic parameters from the <u>anteroposterior configuration</u>	132
Table 43) Hemodynamic parameters from the <u>anteroposterior configuration</u>	132
Table 44) Thoracic impedance average (Z_0) values from the calibrated curves obtained from two acquisitions at each frequency for the <u>posterolateral configuration</u> . The uncertainties for the amplitude and phase are the constants determined on section 5.3.2, for the real and imaginary values an error propagation was made.....	133
Table 45) Peak-to-peak values of the de-noised cardiac impedance component (ΔZ_c) obtained from the thoracic impedance signal for the <u>posterolateral configuration</u> . The uncertainties were estimated from the standard error of the mean.	133

Table 46) Peak-to-peak values of the de-noised respiratory impedance component (ΔZ_r) obtained from the thoracic impedance signal for the <u>posterolateral configuration</u> . The uncertainties were estimated from the standard error of the mean.	134
Table 47) Values used to calculate the hemodynamic parameters from the <u>posterolateral configuration</u>	134
Table 48) Hemodynamic parameters from the <u>posterolateral configuration</u>	134

Acronyms

AC	Alternated Current
ADC	Analog-to-Digital Converter
BP	Band Pass
BPS	Bits Per Second
CO	Cardiac Output
DAC	Digital-to-Analog Converter
DC	Direct Current
DFT	Discrete Fourier Transform
DSP	Digital Signal Processor
ECG	Electrocardiography
EIS	Electrical Impedance Spectroscopy
FFT	Fast Fourier Transform
GUI	Graphical User Interface
HPF	High Pass Filter
HR	Heart Rate
I²C	Inter-Integrated Circuit bus
ICG	Impedance Cardiography
LPF	Low Pass Filter
LVET	Left Ventricular Ejection Time
MAC	Multiply Accumulate
PCB	Printed Circuit Board
PEP	Pre-Ejection Time
RF	Radio Frequency
RMS	Root Mean Square
SCL	Serial Clock
SDA	Serial Data
SNR	Signal-to-Noise Ratio
SPS	Samples Per Second
SV	Stroke Volume
USB	Universal Serial Bus
VCCS	Voltage Controlled Current Source

Chapter 1

Introduction

Contents

1.1.	Introduction	2
1.2.	Motivation.....	2
1.3.	Goals.....	3
1.4.	Thesis Content.....	3

1.1. Introduction

The characteristic electrical impedance of a biological tissue depends on its structure and composition and the variation of such parameters over time reflects itself on the impedance value.

Impedance Cardiography studies the impedance changes in the human chest cavity, arising from volumetric variations of fluids, mostly related to blood translocations during the cardiac cycle. It presents a non-invasive option to continuously monitoring hemodynamic parameters, such as systolic time intervals and cardiac volumes.

1.2. Motivation

According to the World Health Organization, cardiovascular diseases are the number one cause of death worldwide and are expected to remain in the future. The development of diagnostic technics for early detection of cardiovascular risk factors that allow the anticipated treatment can lead to higher survival rates.

The evaluation of the hemodynamic state of the patients in clinical emergency environments is required. The standard vital signs monitored in every medical procedure are heart rate, blood pressure, respiration rate and body temperature [1]. After the pulse oximetry proved to be a fit fifth vital sign, other authors considered the cardiac output from Impedance Cardiography (ICG) appropriated to be used as the next vital sign [2].

In this context, the cardiac output obtained by thermodilution has been a standard parameter for hemodynamic evaluation. Nevertheless, such method is invasive, expensive and time-consuming. Patient comfort, simplicity and cost-effectiveness are desirable characteristics presented by the Impedance Cardiography technic, that exhibits the potential to monitor relative changes in the cardiac output, providing long-term continuous monitoring of the myocardial contractility, as well reliable systolic time intervals [3].

The impedance measurement, although, is affected by several distinct factors, which increase the complexity of its interpretation and difficult the reliable quantification of isolated physiological parameters, imposing restrictions on its use. Despite the ICG's current use in clinical environment, certain points still need to be addressed in what concerns with the methodological standardization, improvement of signal processing methods to eliminate non-blood related effects, validation of realistic chest models applied to calculate hemodynamic parameters, reduce the uncertainties of blood resistivity estimation [4, 5], as well as the

acquaintance of the ICG signal source. On this basis, the interpretations of impedance cardiographic information are still reserved, and the technic is not of general acceptance [2, 5].

The Impedance Cardiography clinical potential, its relatively simple and economic implementation and the need to overcome its present limitations constitute the motivation to further study this seemingly valuable diagnostic technic.

1.3. Goals

This project aimed to develop a prototype system to monitor ICG signals, including the hardware for signal acquisition, the firmware controllers and the user interface to exhibit the relevant data while presenting basic operation options. The offline analysis of the data retrieved by the system can give information about physiological parameters.

1.4. Thesis content

This dissertation is divided into seven chapters. The **first chapter** comprises the framework and objectives of this project, describing its relevance, main goals and the thesis structure. The **second chapter** presents the theoretical background relevant to this project, addressing the main concepts behind electrical bioimpedance measurements, the outlines of the ICG signals, their acquisition and analysis for hemodynamic parameter extraction. The **third chapter** explains the development of a simple phantom produced in order to verify the ICG concept, relating the increase of blood in the chest vessels with the decay of thoracic impedance. The **fourth chapter** includes the description of the ICG acquisition system developed: the impedance unit, the commercial ECG unit included, the firmware operation and the user interface capabilities. In the **fifth chapter** the tests conducted at the hardware level to evaluate its general performance and the calibration procedure developed are presented. The **sixth chapter** reports the validation tests performed in order to verify the effectiveness of the developed system related to the ICG signal monitoring: the methodological guidelines for acquisition and analysis of ICG signals to obtain physiological information and the results of their application to acquisitions on volunteers are presented. In the **seventh chapter** the general conclusions from this work are summarized and future improvements are discussed.

Chapter 2

Theoretical Background

This chapter begins with a physiological contextualization about the heart dynamics, followed by an introduction to the concept of Bioimpedance. The Electrocardiography (ECG) is presented in the terms relevant for the Impedance Cardiography (ICG) analysis. The general concept of the ICG technic is then explained, with a description of the electrical current limitations for human application, the method for measuring the thoracic impedance and the specific electrode dispositions that were applied in the studies during this project. The simplified impedance model of the human thorax and its relation to the Stroke Volume (SV) calculation is presented. Finally, the challenges of the ICG signal analysis in order assess hemodynamic descriptors are discussed.

Contents

2.1.	Circulatory system overview	6
2.2.	Electrical properties of biological tissues.....	8
2.3.	Electrocardiogram.....	9
2.4.	Impedance Cardiography	10
2.5.	Measurement methods.....	12
2.6.	Origin of the ICG signal.....	16
2.7.	Impedance Cardiography signal analysis	19

2.1. Circulatory system overview

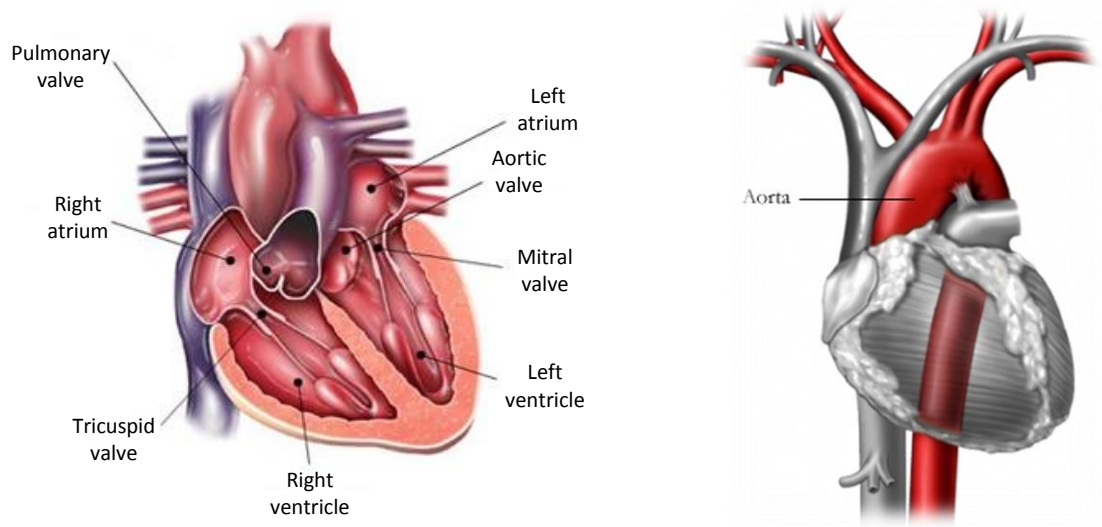


Figure 1) Human heart chambers and valves [6] and aorta detail [7].

The heart is a vital organ, launching the blood into the arteries and veins that delivers the oxygen to the cells and removes the carbon dioxide. It consists on a strong muscular wall, the myocardium, which alternated contraction – systole – and relaxation – diastole – causes blood pumping. The contraction is originated in the cardiac muscle cells that depolarize during the action state and repolarize during the resting state. The heart is divided in four chambers, two atria and two ventricles (figure 1), where the venous blood and arterial oxygenated blood flow separately from the atria to the right and left ventricles and from those into the pulmonary artery and aorta, to be driven across the pulmonary and systemic circulation, respectively. This unidirectional circulation of blood in the heart is assisted by the heart valves.

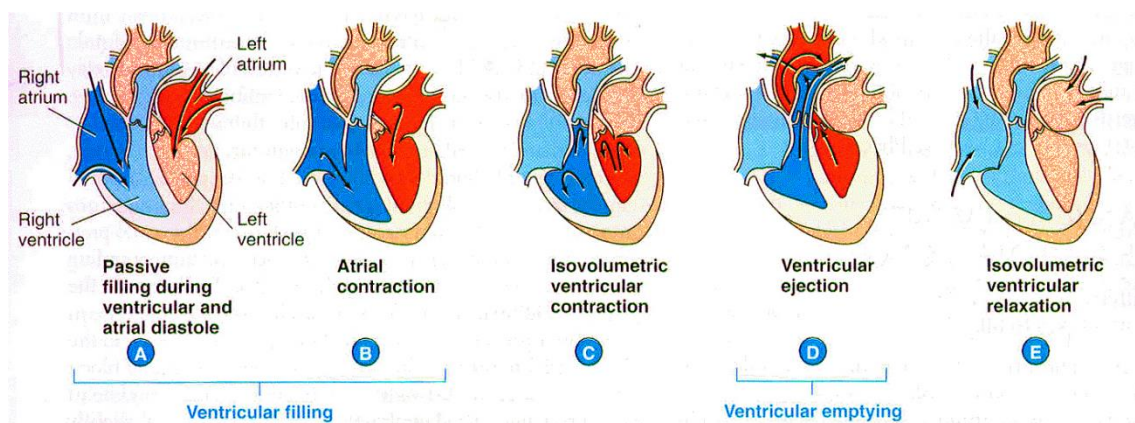


Figure 2) Heart cycle [8].

The left ventricle presents two functions: systolic ejection and diastolic filling (figure 2). The systolic ejection follows an isovolumetric contraction period and occurs at elevated pressures. The high pressure is a requirement for efficient blood supply and fulfillment of the metabolic needs of the organism. Diastolic filling is preceded by an isovolumetric relaxation and occurs at low pressures, a pre-requisite for the correct blood oxygenation in the alveoli. The volumetric pressure causing the stretch of the ventricle wall at the end of diastole, before contraction begins, is the preload and the pressure developed on the left ventricle wall during ejection is the afterload. They describe the interaction between the heart, the venous system and the arterial system, respectively [9].

2.1.1. Systolic times

Since the myocardial relaxation and contraction are orchestrated by intracellular ionic processes the timing of these events is related to the health of myocardial cells. The pre-ejection period (PEP) includes the excitation-contraction coupling and the isovolumetric contraction time of the ventricle. The ejection time (LVET) occurs from the moment the ejection of the left ventricle begins, with the aortic valve opening, until the time the aortic valve closes. A healthy ventricle presents short PEP and large LVET [10].

2.1.2. Cardiac output

Cardiac output (CO) is the volume of blood being pumped by the heart per minute, a product of the heart rate (HR) and stroke volume (SV). The SV of the ventricle is determined by its contractility, the preload and the afterload. The CO is an important parameter for the cardiac function evaluation, especially related to the ventricular performance, providing information about the body oxygen perfusion and giving insights about the hypertension origins.

The most widespread method to measure CO is the invasive thermodilution method, considered the golden standard, which involves inserting a catheter into the circulatory system. The safety of such method is questionable, since catheterization is associated with increase of morbidity and mortality rate in critically ill patients [11]. The Impedance Cardiography (ICG) appears as a fitted alternative, offering a simple, safe and inexpensive method for non-invasive cardiac output monitoring and also providing assess to reliable systolic time intervals [3].

Several studies tried to correlate invasive standard methods for assessment of SV and CO with ICG results presenting different degrees of success. The ICG technic shows high

correlations in subjects with stable circulatory system, but presents poor results in patients with failing circulatory system, valvular or other cardiovascular problem [12] and under conditions of hypoxia, drugs and ventilator maneuvers [13, 14]. However, the determination of CO using the later ICG technology – commercial devices – seems to be less variable and shows better reproducibility on the same subject than the thermodilution, presenting equivalent results to the invasive method in patients after coronary artery bypass graft and showing improvements when compared to previous generation methods [2]. There is a general agreement that ICG requires more methodological investigation [5, 15], but is satisfactory for the determination of relative changes in cardiac output on normal subjects [13]. The contradictory appreciations of the technic over the years led to a reserved consideration of ICG data interpretations and the acceptance of the technique is still not generalized [2, 5].

2.2. Electrical properties of biological tissues

Bioelectricity encompasses all the electrical phenomena in the living systems. In this context is relevant to distinguish between the phenomena that occur in response to externally applied (exogenic) electricity, such as the bioimpedance measurements, and the ones induced by internally generated (endogenic) electrical activity, as the heart beating, the nervous system activity and the muscle contraction. The ICG and ECG are examples of each one, respectively, with application in the study of human hemodynamics.

The impedance of a biological tissue (Z) is a passive electrical property that quantifies its opposition to a current flow externally applied. This value is a complex number that can be calculated through the Ohm's law (equation 1). The impedance value can be represented in one of two forms (equation 2): a complex exponential with amplitude $|Z|$ and argument θ , correspondent to the phase difference between voltage and current, or alternatively, as a combination of a resistance (R , real component of Z) and reactance (X , imaginary component of Z).

$$Impedance = \frac{Voltage}{Current} \quad (1)$$

$$Z = |Z|e^{j\theta} = |Z|\cos\theta + j|Z|\sin\theta = R + jX \quad (2)$$

The biological tissues in the human body are complex anisotropic conductors, where the electrical current flows due to the migration of ions. Their content in water and electrolytes determine the conductive characteristics: the resistive or reactive behavior. The lipidic cellular membrane presents a capacitive reactive behavior while the intracellular and

extracellular contents mainly present a resistive behavior. Accordingly, the current conduction will be different depending on the frequency: at low frequencies the current will pass around the cells, while at high frequencies the current will cross them (figure 3). This behavior is described by the Cole-Cole model that represents the tissue by an equivalent electrical circuit [16].

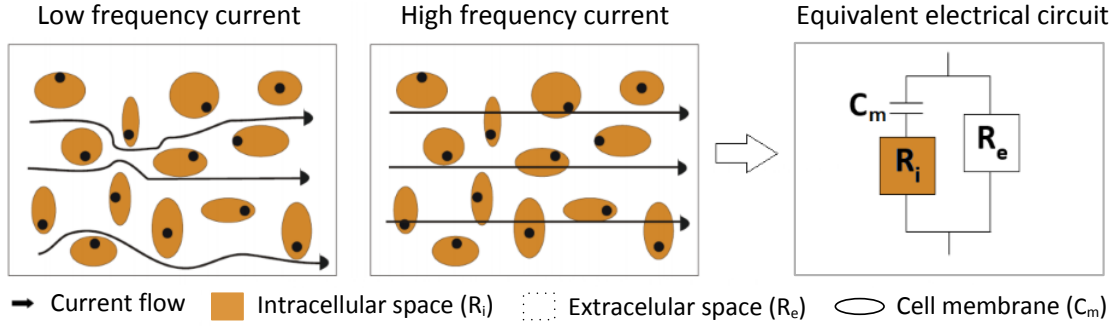


Figure 3) Equivalent electrical circuit for biological tissues. Adapted from [17].

The electrical equivalent circuit represents the intracellular fluid as resistance (R_i) and the cellular membrane (C_m) as capacitance in parallel to the extracellular fluid resistance (R_e). The R_e , R_i and C_m values can be drawn from measuring the tissue's impedance at various frequencies (f). The relation of this values to the overall impedance $Z(f)$ is represented in a simplified way by the equation for the RRC circuit (equation 3).

$$Z(f) = \frac{R_e \times \left(R_i - \frac{j}{2\pi f \times C_m} \right)}{R_e + \left(R_i - \frac{j}{2\pi f \times C_m} \right)} \quad (3)$$

At low frequencies ($f \rightarrow 0$) the cell membrane behaves as an insulator, therefore the capacitor acts as an open circuit and the current flows solely through the extracellular fluid. At high frequencies ($f \rightarrow \infty$) the capacitor acts as a short circuit and the impedance results from the combination of the intra and extracellular fluid resistances [17].

The ICG measurement process uses a single excitation frequency, to obtain the impedance value over a period of time. This way the Cole models are not of direct application in this context.

2.3. Electrocardiogram

The electrocardiogram (ECG) records the time-varying electric phenomena originated by the heart, through the measurement of the differential electrical potential between two

electrodes in contact with the body. The frequency spectrum of the ECG signal is between 0.05 and 100 Hz, and its dynamic range is 1-10 mV [12, 18].

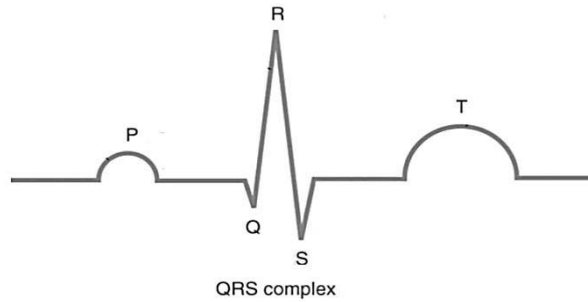


Figure 4) ECG signal showing the characteristic points and waves in one cardiac cycle [19].

The characteristic shape of the ECG signal is related to the electro-mechanical events that occur during the cardiac cycle. The P wave represents the atrial depolarization. The ventricle depolarization forms the QRS complex, with the first downward deflection corresponding to the Q wave, the upward deflection the R wave and the final downward deflection the S wave. After the isoelectric segment, follows the ventricle repolarization corresponding to the T wave [19]. The RR interval, between two consecutive R waves, defines the heart rate (HR).

The short-duration QRS complex is the most predominant feature on the normal ECG signal and presents special relevance for the ICG analysis.

2.4. Impedance Cardiography

Impedance Cardiography (ICG) studies the volumetric variations of fluids in the human chest related to the cardiac activity, by measuring the changes in thoracic impedance during the heart cycle.

The technic consists on applying a controlled alternating current, with constant amplitude and frequency, to the surface of the unknown chest impedance and measuring the established electrical potential, to estimate the impedance value using Ohm's law [4].

The thoracic impedance ($Z(t)$) consists of a relevant resistive component (15–45 Ω) and a negligible imaginary component, correspondent to an approximate 10° phase shift, which is not used for the purpose of cardiac evaluation [4] [20]. Each heart beat causes a pulsatile decrease (ΔZ) in the mean thoracic impedance (Z_0) during systole, which implies a region in the chest where the blood volume is increasing [21]. The impedance values, from several measurements over time, are presented as an impedance waveform and the ICG signal is obtained as the first derivative of ΔZ . The typical ICG traces are accompanied by an

electrocardiographic (ECG) signal, recorded simultaneously to the impedance measurements, that serves as time reference.

Hemodynamic parameters (systolic times and cardiac volumes, mostly) can be assessed based on the relative location of ICG and ECG characteristic points, in combination with the thoracic base impedance (Z_0), thoracic dimensional descriptors and blood resistivity estimates, based on theoretical models.

2.4.1. Current limits

There is overall consensus in the use of sinusoidal currents with amplitude between 1 and 5 mA and frequencies in the range 20–100 kHz for ICG applications. The lower current amplitude limit is the necessary to obtain sufficient SNR. Such current amplitude can lead to muscle excitation at frequencies lower than 20 kHz. At the frequency of 100 kHz the electrode-skin impedance (section 2.5.2) is reduced when compared to low frequencies, which helps decreasing its disturbing impact in the cardiac signal. However, frequencies above 100 kHz introduce problems of stray capacitances [4].

In the working frequency range the current amplitude must be defined in order to ensure that the potential induced on the heart muscle is substantially below the levels that might cause fibrillation (figure 5).

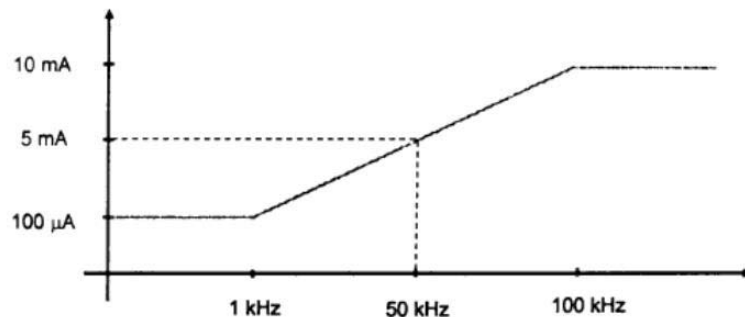


Figure 5) Permissible AC-current (peak-to-peak values) through the human body in accordance to the Standard EN60601 for medical devices. Extracted from [17].

The application of DC currents to biological mediums is limited (table 1), since it causes the medium polarization due to electrochemical processes that take place in the aqueous conducting media, altering the ionic distribution.

Table 1) Effects of the DC current in the human body. Extracted from [22].

Effect	DC current (mA)	
	Men	Women
Slight sensations in the hands	0.6	1
Threshold of perception	3.5	5.2
Painless shock without loss of muscular control	6	9
Painful shock without loss of muscular control	41	62
Painful shock and fixation current threshold (let-go)	51	76
Shock with intense pain, muscular contraction and breathing difficulties	60	90
Possible cardiac fibrillation	500	500

2.5. Measurement methods

The impedance measurement is commonly performed using one of two primary electrode configurations: the tetrapolar configuration (i.e. using four electrodes) or the bipolar configuration (i.e. using two electrodes). Most of the ICG procedures use at least four electrodes in order to overcome the influence of the skin electrode interface, which greatly affects the measurements in a bipolar configuration.

In the bipolar configuration (figure 6) the current is injected through the same electrodes that sense the voltage. The voltage is measured not only across the unknown impedance but also across the cables, electrode contacts and skin impedances. This additional impedance component is difficult to separate and introduces errors in the measurement.

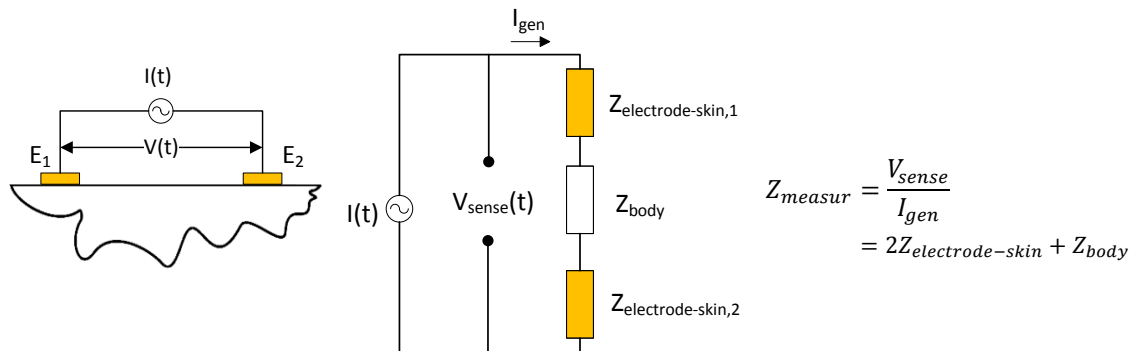


Figure 6) Bipolar configuration, equivalent circuit and impedance mathematical description. The blocks represent complex impedances.

In the tetrapolar-electrode configuration (figure 7), the four electrodes have different roles: the current is injected via two application electrodes (E1, E4) and the voltage is detected via the sensing electrodes (E2, E3). The influence of the electrode-skin interface impedance is minimized since the voltage sensing is made through high input impedance probes. Therefore, insignificant currents flow into the sensing leads and only the voltage differential across the load impedance is measured, providing a more reliable solution. The impedance can be approximated by the simple application of the Ohm's law [4].

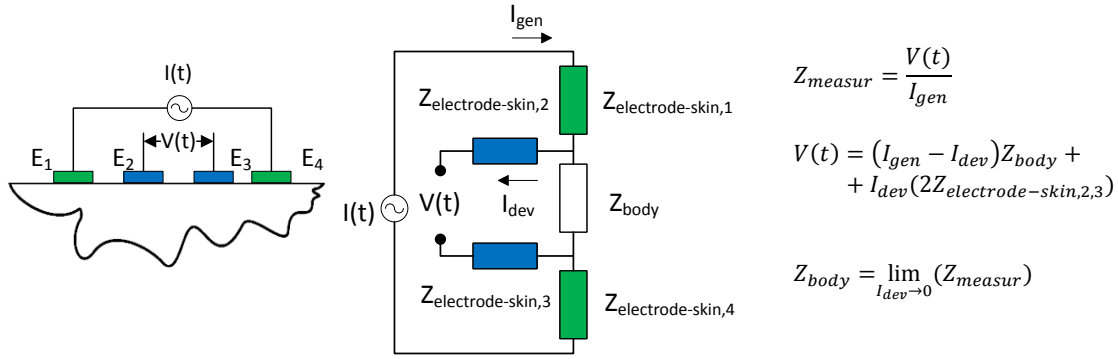


Figure 7) Tetrapolar configuration, equivalent circuit and impedance mathematical description.

2.5.1. Electrodes: type and topography

The electrode that establishes the interface between the measurement device and the body, allows the electrical conversion from ionic conduction into electronic conduction, as the current passes from an electrolyte into a metallic conductor.

One of the most popular methods for quantitative evaluations based on ICG, first reported by Patterson and Kubicek [23, 24, 25], was performed with a tetrapolar electrode system using band electrodes around the thorax extremities: two placed around the neck and two around the chest at the level of the xiphisternal joint and in the base of the ribcage. The outside bands inject current while the inner bands measure voltage. [26].

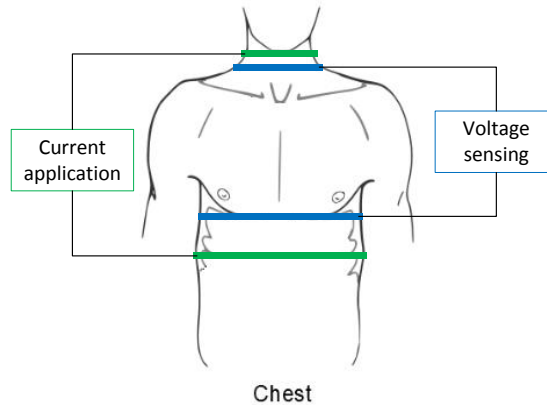


Figure 8) Kubicek band electrode system.

Although band electrodes offered lower impedance and presented bigger effective area, they were also difficult to handle and inappropriate for many clinical applications, for those reasons they have been substituted by spot electrodes. The common disposable spot electrodes provide precise transmission of surface bio-potentials developed across the human skin. They are constituted by aluminum or silver-silver chloride coated with hydrogel, which serves as adhesive and electrolytic medium, being physiological inert over short periods. They are commonly used in ECG and also ICG applications.

Some general rules concerning the electrode positioning on ICG can be pointed: to obtain reproducible measurements, the voltage electrodes must be placed with a distance of at least 3 cm from the application electrodes, avoiding the influence of high current densities around the last ones; the distance between the voltage electrodes must be kept constant between measurements since it affects substantially the value of Z_0 but also ΔZ and $(dZ/dt)_{\max}$ [26].

Due to a lack of standardization, several tetra polar configurations using spot electrodes are described in the literature [27, 28, 26, 29, 30, 31]. Other configurations used in more complex systems apply a higher number of electrodes in order to optimize the measurement procedure [32, 33, 34]. Different configurations show different sensibilities to different signal sources, but in practice they produce similar SV estimations [34] and systolic times [35]. Two common tetrapolar configurations are further described since they have particular interest for this project. These configurations present easy reproduction based on body markers.

2.5.1.1. Anteroposterior configuration

The configuration proposed by Qu et al [28] places the electrodes in the sagittal plane: the current application electrodes are located posteriorly, one above the C4 vertebra and a second one between the thoracic vertebrae T8-T9; the voltage sensing electrodes are located frontally one at the base of the neck, above the jugular notch, and a second one over the sternum leveling with fourth rib.

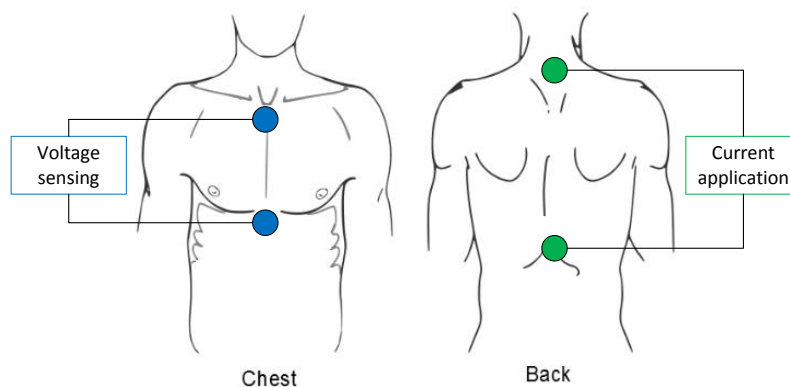


Figure 9) Tetrapolar electrode configuration from Qu et al.

2.5.1.2. Posterolateral configuration

The tetrapolar configuration suggested by Penney et al. [27] places two electrodes in the posterior surface of the neck separated by 6 cm and centered on the C7 prominence. The

remaining electrodes are placed on the left side of the thorax: one on the mid-clavicular line, at the end of the ninth intercostal space and the second in the mid-axillary line at the end of the tenth intercostal space. The current passes through the electrodes on the right side of the neck and on the left mid-clavicular line, while the remaining electrodes sense the voltage.

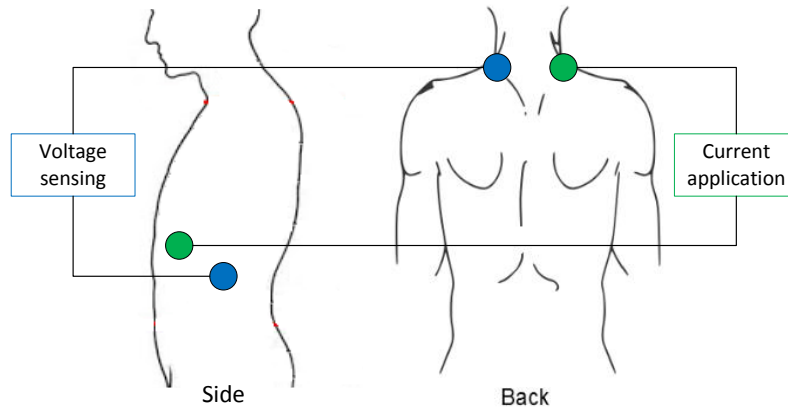


Figure 10) Tetrapolar electrode configuration from Penney et. al.

2.5.1.3. Electrode polarity

The electrode polarity is usually not specified, which might reflect its irrelevance. Although some commercial devices specify the electrode polarity, their suggestions do not agree: the Biopac system's web page suggests the position of the two positive (high current and voltage) electrodes above the two negative ones (low current and voltage) [31] and the user's manual [36] from the Vrije Universiteit Ambulatory Monitoring System [37] specifies the location of the two negative electrodes above the heart level and the positive ones below.

2.5.2. Electrode-Skin interface

Not only the contact electrode-skin presents a resistance to the current flow, as also the electrode electrical behavior can affect the measurements by introducing a DC bias, in result of changes in the electrode potential [38].

The standard electrode can be described by a simplified equivalent circuit (figure 11) with passive components, not accounting the DC drift. The model includes three serial impedances: the skin (Z_{skin}), the contact (Z_{contact}) and the electrode ($Z_{\text{electrode}}$). The value of the skin impedance amplitude approaches $220 \, \Omega$ at $100 \, \text{kHz}$, the contact impedance, corresponding to the resistance of the hydrogel, is near $88 \, \Omega$ and the electrode impedance amplitude is around $3 \, \Omega$ [39].

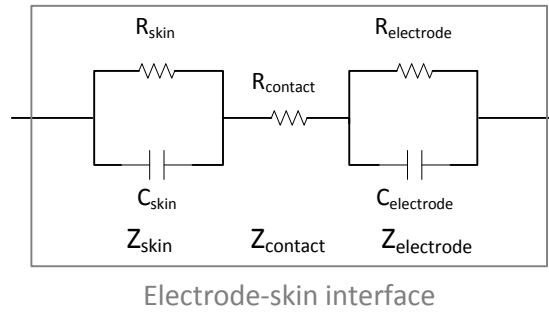


Figure 11) Electrode-skin interface circuit for the typical spot electrode. Adapted from [17].

2.6. Source of the ICG signal

The blood is characterized by its high conductivity, presenting a resistivity two times lower than the muscle and many times higher than the less resistive tissues. Relative to static conditions, the flowing blood presents a decrease in resistivity of at most 10% [40]. This data supports the idea that in ICG the change of the impedance signal is mostly caused by blood volume translocations, while other tissues either maintain the volume or present distinctively higher resistivity. In the particular case of the myocardium the resistivity is five times higher, leading to the electrical isolation of the blood inside it [4].

Furthermore, after several analysis, the cardiac hemodynamics, i.e. changes in blood volume and velocity, were considered the main cause of impedance variations [41]. The varying speed of ejection specially affects the systolic part of ΔZ , while the diastolic part of the impedance signal exhibits the effect of volume alterations [13]. Other conclusions were drawn in respect to the ICG signal [42]: it is a complex signal resulting of multiple sources contribution; its components are not synchronized and their proportions not well defined; it is dependent on changes in the aorta diameter, neck arteries and pulmonary vessels and also on the change of blood resistivity related to cell reorientation in large vessels; it seems to be independent of the heart volume and its blood content, thanks to the isolating properties of the myocardium; for typical electrode positions it is not affected by the extension of the pulmonary artery. These illations, while interesting, do not clarify the origin of the ICG signal, which is still an object of study, pointing out the weakest feature of the technic [13]. At this point, there is still controversy between most authors [43] and more investigation is still needed in this area.

Currently, the changes in thoracic impedance related to the cardiac activity are accepted as caused primarily by ejection of blood from the left ventricle into the aorta, having a close relation to the SV [4]. As the current flows through the path of least resistance, mostly

the aorta that carries the largest volume of blood in the thorax, the cyclic expansion causes a pulsatile change in the base impedance [15].

2.6.1. Simplified model of the human thorax

In a very simplified model, the chest region impedance is represented as a cylinder divided in two parts: the tissue and the blood (figure 12). The impedances of the partial cylindrical volumes are electrically connected in parallel. If the subject does not breathe the only fluid variation is related to the amount and distribution of blood during the heart cycle. The blood volume changes would be represented as variations in the crosssectional area, i.e. the ejection of blood from the heart would be represented as an increase in diameter.

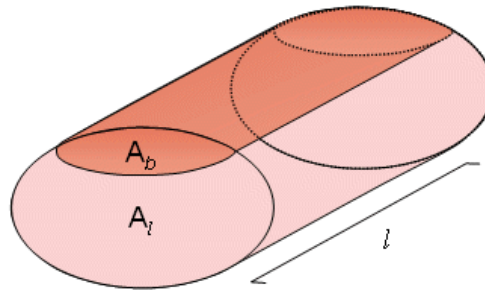


Figure 12) Parallel conductor model for the human thorax impedance, with uniform blood and tissue compartments with crosssectional areas A_b and A_t , respectively and constant length L . Extracted from [13].

Based on the parallel model assumptions, the general expression to describe the increment of blood (ΔV) as a function of the correspondent decrement of the electrical impedance (ΔZ) in a cylindrical region of the body was derived by Nyboer (equation 4) [13]. Where ρ is the blood resistivity, L is the length of the cylindrical model and Z_0 is the mean impedance of the model.

$$\Delta V = -\frac{\rho L^2}{Z_0^2} \Delta Z \quad (4)$$

The ΔV and ΔZ vary almost periodically with the heart pulsation, $\Delta V = \Delta V(t)$ and $\Delta Z = \Delta Z(t)$, while the mean value Z_0 changes slowly, typically in accordance to the pulmonary function, $Z_0 = Z_0(t)$. Thus Nyboer proposed the partition of the measured impedance into two additive components with distinct magnitude and spectra (equation 5) [44].

$$Z(t) = Z_0(t) + \Delta Z(t) \quad (5)$$

The validity of the parallel cylinder model was questioned after inaccurate results, and subsequently more complex models were developed (multi-cylinders or models representing the main blood vessels). Although, when compared with practical studies the

results from such models would still not agree in relation to the origin of the impedance signal [13].

2.6.2. Method for stroke volume calculation

Kubicek proposed the modification of Nyober's formula (equation 4) in order to obtain the SV. Provided that the maximum peak of the impedance derivative $((dZ/dt)_{max})$ is a mean blood acceleration analog during systole, it permits its integration during the ejection time, in order to obtain the impedance variation (ΔZ) analog (equation 6) [45, 13]. It should be noticed that the peak value of the ΔZ derivative is a negative value, sometimes referred as $(dZ/dt)_{min}$, that is conventionally taken in the upward direction (in module) and referred as $(dZ/dt)_{max}$, since the signals on the Nyober's expression cancel out.

$$\Delta Z = LVET \times \left(\frac{dZ}{dt} \right)_{max} \quad (6)$$

This way the volume variation of blood during systole can be identified with the SV as given by equation 7, where SV is the stroke volume (ml), ρ is the blood resistivity ($\Omega \cdot \text{cm}$), L is the distance between the inner sensing electrodes (cm), Z_0 is the base impedance (Ω), $(dZ/dt)_{max}$ is the largest peak occurring during systole on the impedance signal first derivative (Ω/s) and LVET is the left ventricular ejection time (s) [12].

$$SV = \rho \frac{L^2}{Z_0^2} LVET \times \left(\frac{dZ}{dt} \right)_{max} \quad (7)$$

This method is widely used to estimate SV from impedance recordings, but being based in the two-compartment cylindrical model it presents a big abstraction and the change in blood resistivity with velocity is completely neglected [13].

Other methods for stroke volume calculation based on more accurate geometric models and considering other particular descriptors of the subject are available [45]. Thus such models, as well as the presented one, are able to provide a reliable SV estimation [4].

2.6.2.1. Blood resistivity value

The blood resistivity (ρ) is one of the parameters in Kubicek's formula which makes it accurate assessment necessary. Two approaches to its determination are referred: ρ as a constant with a value between 130 and 150 $\Omega \cdot \text{cm}$ or ρ as a function of the hematocrit – percentage of red blood cells on the total blood volume. Even though significant variations of the hematocrit are reported in diseased individuals [46], the use of constant values to obtain

the SV using Kubicek's formula proved to have strong correlation with direct methods of measurement [4]. In this basis seems to be good practice to rely on a constant value when performing ICG in healthy subjects, in an outpatient setting.

2.7. Impedance Cardiography signal analysis

The term 'impedance' is usually applied indiscriminately when referring to the ICG evaluations. Although, there are suggestions that both the magnitude [47, 48, 45] and the resistive part [42, 20, 49] are applied in different studies. This question is irrelevant when neglecting the effect of the thoracic reactance, which is probably in the base of the lack of distinction.

The base thoracic impedance (Z_0) value varies between subjects, frequency of the AC current and with the electrode configuration. For SV calculations the most important component of the thoracic impedance is related to the changes (ΔZ) in the main impedance [45]. The ΔZ due to blood circulation is influenced by respiration and motion artifacts, that present relatively large amplitude and can cause relevant baseline wander [50]. Such artifact is fundamentally caused by changes in the chest dimensions during the breathing cycle (figure 13).

The impedance cardiography (dZ/dt) spectrum extends from DC to 50 Hz [51]. The respiratory related component is in the range of 0.04-2 Hz, while the motion artifact band is between 0.1-10 Hz [50]. Thus, the ICG and the artifact spectra overlap. This way, the baseline for further calculations has to be determined separately for each heart cycle or otherwise the low frequency modulation has to be removed from the signal. The elimination of such effect can be performed by one of the following methods [4].

- Temporary elimination of breathing: despite breathing modulation removal, it affects the cardiac volumes and is not appropriate to perform some physiological tests such as exercise or extended monitoring;
- Application of ensemble averaging methods: several sets of data are obtained and averaged together to reduce random fluctuations of the signal and provide the mean curve during a certain period of time. The information concerning beat-to-beat variations is lost and some features are commonly blurred. The time frames for averaging are determined in respect to an intrinsic reference point or to another reference signal. The R wave from the simultaneously acquired ECG is typically used to synchronize the ICG ensemble average on a beat-by-beat basis.

- Digital filtering: this probably presents the most flexible solution. Although, the use of a narrow filters centered on the heart rate seems to introduce nonlinear phase distortion and attenuates the high frequency components. Plus, adaptive filtering presents the disadvantages of not correctly cancel the respiratory and motion artifact, since they overlap the spectrum of cardiac signal [50]. Other straightforward filtering techniques are still in investigation.

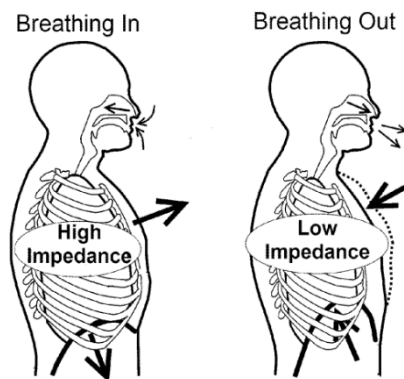


Figure 13) Influence of breathing on the thoracic impedance [52].

Despite being considered an interference in the ICG signal analysis, several authors have studied the respiratory impedance signals derived from ICG in order to extract information related to the respiratory function [53, 54, 20].

2.7.1. Characteristic points and periods

The derivative of the impedance variation, the so called ICG signal, is used to assess the hemodynamic parameters (figure 14). Despite the attempts to draw conclusions based on qualitative differences in the morphology of the ICG signal - mostly related to diagnosis of valve malfunction – their immature state confines the ICG analysis mainly to quantitative estimation of cardiac parameters [4].

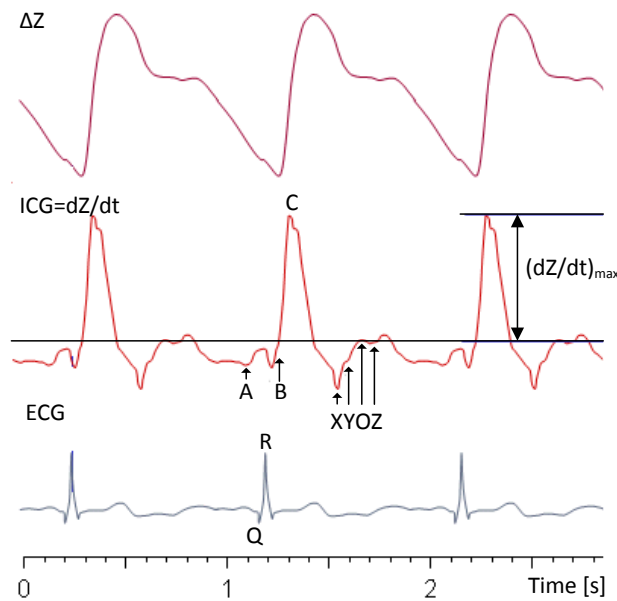


Figure 14) ICG typical waves (ΔZ , dZ/dt presented in the upward direction) and ECG reference signal. Adapted from [13].

Several notches of the ICG curve were associated with different mechanical events that occur during the cardiac cycle [55]. Those points are identified by the letters A, B, C, X, Y, O, Z, similarly to the ECG, and their description is presented on table 2.

Table 2) Characteristic points on the ICG signal [4].

Characteristic point	Description
A (atrial wave)	Associated with the atrial contraction; its amplitude is related to the ejection fraction of the left atrium.
B	Associated with the aortic valve opening, it denotes the beginning of the (left ventricle) ejection time. It appears on the ascending section of the ICG signal before $(dz/dt)_{max}$, at the baseline level. Its identification can be problematic since the characteristic upstroke used as its marker may be indistinct. The correct localization of this point in the ICG curve is crucial for accurate calculation of systolic time intervals, SV and CO.
C (also called E)	Reflects the maximum speed of change in the impedance and is associated with the maximum ejection velocity. The $(dz/dt)_{max}$ is the maximum amplitude of the signal, measured from the baseline to the C point location.
X	Corresponds to the aortic valve closure (the second heart sound) and appears as the lowest value in the negative portion of the ICG signal after C.
Y	Corresponds to the pulmonary valve closure.
O	Wave associated with changes in volume during the diastole and with the opening sound of the mitral valve.
Z	Associated with a third heart sound, it corresponds to a downward deflection after the O wave.

The ICG notches are best noticeable in signals collected from healthy subjects while lying down either in the supine or prone position [49].

The temporal relations between some characteristic points in the ICG signal present physiological and clinical relevance. From the characteristic periods indicated on table 3, the most frequently studied are PEP and LVET which present direct relation with the heart systole.

Table 3) Characteristic periods in ICG [4].

Characteristic period	Description
Q-B	Time between the onset of the heart chambers contraction (Q point in ECG) and the aortic valve opening. It is denominated the pre-ejection period – PEP - and is commonly used as an index of myocardial contractility and sympathetic control of the heart.
Q-C	Time between Q point (ECG) and the ICG curve maximum. It is applied to calculate the Heather index for cardiac contractility.
B-X	Time between the opening and closure of the aortic valve, corresponding to the left ventricular ejection time – LVET .

2.7.2. Hemodynamic parameters

The most relevant hemodynamic parameters that can be extracted from the ICG signal analysis (table 4), apart from the systolic intervals, are the SV and the CO.

Table 4) Hemodynamic parameters [4].

Hemodynamic parameter	Description
Stroke Volume (SV)	Volume of blood pumped by the left ventricle during one contraction cycle, is expressed in milliliters per beat [ml/beat].
Cardiac Output (CO)	Volume of blood ejected by the heart into the systemic circulation during 1 min, is expressed in [L/min]. It is defined as the product of SV and the heart rate (HR), or by the sum of all SV values occurring during the period of 1 min.
Systolic Time Ratio (STR)	Ratio PEP/LVET, is considered as an index of cardiac contractility.
Total Fluid Content (TFC)	The inverse value of the base impedance (Z_0), is expressed in [1/k Ω]. It is an indicator of the fluid content in the thoracic cavity.
Heather index	Cardiac contractility index defined as the ratio of $(dz/dt)_{max}$ to the Q-C period, expressed in [Ω/s^2]. It represents the rate of impedance change from the beginning of the cardiac contraction to the peak of the mechanical action.

From the referred hemodynamic parameters, several hemodynamic indices [4] can be derived using the characteristic points and periods taken from the ICG and ECG curves, blood pressure and/or other body characterization parameters.

Chapter 3

Phantom Setup

This chapter presents the methodology involved in the development of a simple bench system in order to replicate the decrease in thoracic impedance with an increased blood volume in the vessels near the heart.

The results from the impedance measurements performed on a static phantom composed of several agar-agar volumes embedded on a relatively low conductive aqueous solution are presented and discussed.

Contents

3.1.	Materials and methods	24
3.2.	Results and discussion.....	32

As follows from the ICG concept, the blood ejection during the cardiac systole causes the surrounding structures to swell due to blood inflow [56] and accordingly, a decrease of thoracic impedance is registered (section 2.6). To verify that an increase of a conductive volume within less conductive surroundings causes a depletion of the impedance measured across the whole system, a static phantom was developed.

The resistivity of the thoracic tissues, without considering heart and lungs, is approximately three times higher than the resistivity of blood [57]. This physiological ratio was the primary point considered when choosing the phantom materials and adjusting their conductive properties to electrically mimic the blood and thoracic tissue.

3.1. Materials and methods

To perform impedance measurements a portable Electrical Impedance Spectroscopy (EIS) system described by Borges et al. [58], was employed. The system works in a bipolar configuration with needle electrodes. The present formulation of such system allows the measurement of impedances down to 100 Ω without incurring in error, that limitation had to be accounted in the phantom development. All the impedance measurements were the result of applying an excitatory AC voltage to the sample in study. In this procedure three excitatory frequencies in the range of the ICG specifications were studied - 50 kHz, 70 kHz and 100 kHz.

During the described procedures the materials were weighted using a balance with scale 0.4-500 g and precision 0.1 g. For liquid volumes greater than 150 mL a graduated recipient with scale 100 to 1000 mL and precision 100 mL was used. For more precise measurements or smaller liquid volumes was used either a graduated syringe with scale from 2-100 mL and precision 2 mL or one with scale 1-60 mL and precision 1 mL.

3.1.1. Electing the materials

The agar-agar alga is commonly used to develop nutritive media for microorganism cultures. Thanks to its consistency - similar to gelatin - it has also been employed on the conception of phantoms simulating solid bodily tissues [59, 60, 61]. A preliminary test on 20 mL solidified agar-agar samples prepared with distilled water (1.15% (m/m)) resulted on a resistance close to 4.5 k Ω (and reactance near -133 Ω) at an excitation frequency of 100 kHz. Even though the average value of thoracic impedance could not be reached attending to the limitations of the EIS system, the agar-agar sample resistance was worked on to present a better approach to such value. The reactance value was only taken for control.

Chapter 3: Phantom Setup

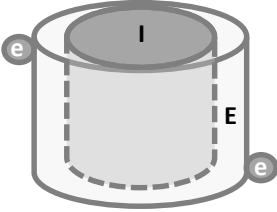
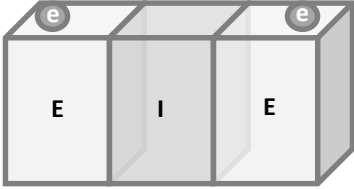
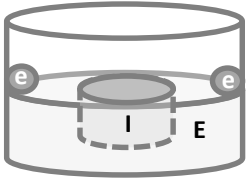
The electrical conductivity of water is directly dependent on the concentration of salts dissolved on it. Distilled water has low ionic concentration, hence presenting high resistivity. The smaller the ions dissolved, the faster they travel across the solution, increasing the conductivity. Strong acids and bases, with high degree of ionization in water, cause a more drastic increase in the conductivity than weak acids or bases, which partially ionize, or salts, that provide larger ions.

In order to decrease the agar-agar resistivity, in a controlled way, two easily affordable resources were explored: sodium chloride (NaCl) and citric acid ($C_6H_8O_7$). The NaCl, known as the ordinary table salt, dissociates into sodium and chloride ions when dissolved in water. Citric acid is a weak organic acid found in lemon or lime juice in more significant quantities than in other citrines. These two substances in low concentrations allow an easy manipulation of the conductive properties of a solution.

After a trial and error process, the results that better approached the required impedance for the low resistive medium were obtained by adding natural lemon juice to the agar-agar preparation and then correcting the results with NaCl. Alongside, acceptable results were obtained with an aqueous solution of lemon juice in distilled water, as the less conductive medium.

3.1.2. Phantom models and Practical limitations

Table 5) Idealized phantom models

Geometry 1: cylindrical solid container.	Geometry 2: rectangular shape.	Geometry 3: cylindrical central mass embedded on liquid solution.
		
e – electrodes; I – internal content (blood-like); E – external content (resistive tissue-like).		
Advantages		
<ul style="list-style-type: none"> • The geometry agrees with the simplified models for the human thorax; • Enables the use of ICG electrodes. 	<ul style="list-style-type: none"> • The several rectangular pieces can be easily shaped; • Enables the use of ICG electrodes. 	<ul style="list-style-type: none"> • Since the electrodes are fixed to the container sides, the distance between electrodes can be easily maintained between measurements.
Disadvantages		
<ul style="list-style-type: none"> • The variation of the internal content is not possible using the same phantom: several cylinders with different central diameters are needed; • To avoid leakage the central pool cannot trespass the cylinder and the pool depth might vary between different phantoms; • The internal content consistence and shape have to be optimal to permit correct juxtaposition; • Removing the agar from the cylindrical mold was proven to be difficult without damaging it. 	<ul style="list-style-type: none"> • The central mass has to present a consistence that permits the correct juxtaposition of surfaces; • Several phantoms with different central volumes are needed; • The difficult maintenance of the distance between electrodes. 	<ul style="list-style-type: none"> • Needs several central masses with different volumes; • The ICG spot electrodes cannot be used; • The external content has to be liquid while the central mass is solid which does not agree with the physiologic reality; • The electrode disposition is not in accordance to the ICG reality that disposes the electrodes along the vertical conductive axis, perpendicularly to the tissue swelling.

The three configurations described in table 6 were tested in miniature set-ups. The first and second geometries shown similar practical problems: the distance between electrodes was difficult to maintain since there was no direct point of reference between phantoms; and the interface between solid samples presented a highly resistive barrier to the current even when the surfaces were pressed together. The third geometry shown to be the simplest and most reliable, even though it did not reproduced the theoretical models and could not be used to perform tests with the real ICG spot electrodes that need to be attached on a solid surface.

3.1.3. Final formulation

In its final formulation, following the third geometry in table 5, the phantom was composed by four agar-agar masses with different volumes surrounded by an aqueous solution composed of 9.1% (v/v) natural lemon juice on distilled water (resistivity $>200 \text{ k}\Omega\cdot\text{cm}$). The agar-agar was prepared from an aqueous solution of 0.2% (m/m) NaCl and 1.4% (m/m) of agar-agar for food applications on distilled water. This solution was heated with a microwave oven (Power=800 W) inside a Pyrex container for a total of 6.5 minutes. To prevent the solution from boiling - which would render its density uneven - the heating time was divided into successive intervals of 120, 60, 60, 45, 45, 30 and 30 seconds and at the end of each heating period the solution was stirred. Natural lemon juice was then added to the agar while it was still liquid (temperature $>50 \text{ }^{\circ}\text{C}$), to make up for 4.8% (v/v) of the initial volume of solution.

A control sample of 20 mL was collected and the remaining agar-agar was then disposed on a plane PP (polypropylene) container ($\varnothing 15\text{cm}$) to cool down at ambient temperature for 2 hours. Then the container was covered and transferred to the fridge, where it stood for around 6 hours. The measurements were performed with agar-agar at ambience temperature, after it was out of the fridge for a few minutes. To avoid problems with the adherence to the walls of the container, the agar-agar was chopped of the container with circular cutting molds after its solidification (figure 15).

The aqueous solution was prepared in slots of 330 mL right before the measurements took place by stirring together the distilled water and the lemon juice. After that a 20 mL sample was collected for evaluation.

To prove the repeatability of the experience two phantoms were separately realized following the procedure described above. The final results presented are averaged values of the evaluations performed in each phantom. For every sample tested the impedance was measured two times at each frequency (f) of interest – 50 kHz, 70 kHz and 100 kHz – and then averaged with respect to each frequency.

Chapter 3: Phantom Setup

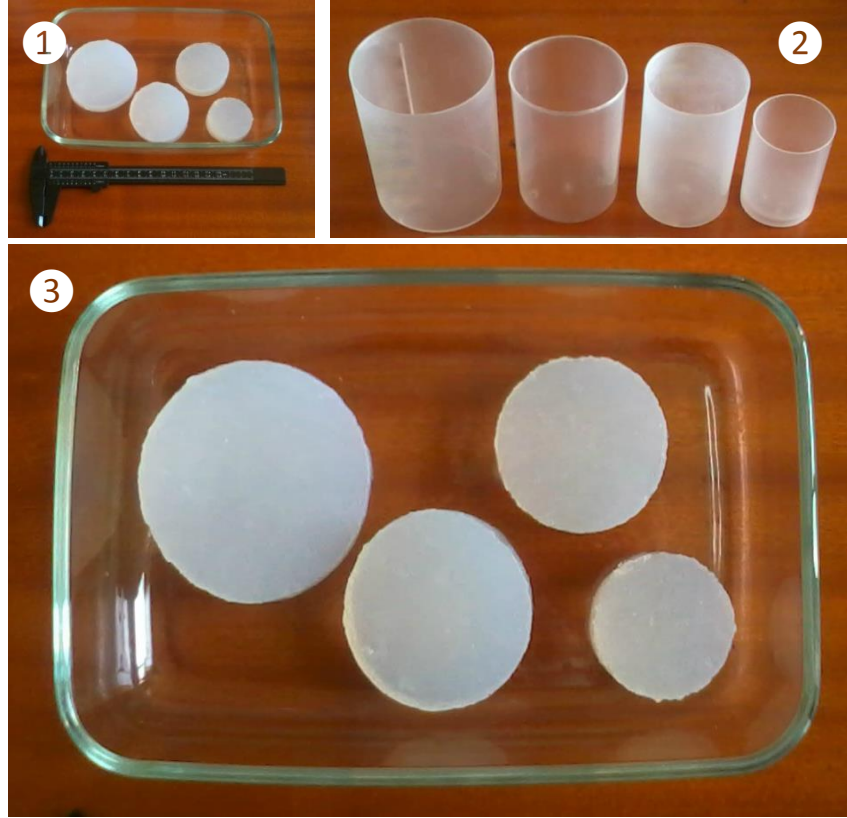


Figure 15) Agar-agar cylindrical masses (1)/(3) and molds (2) used to cut them ($\varnothing=6.63$ cm, 5.59 cm, 5 cm and 4.02 cm, from left to right).

The 20 mL samples of aqueous solution and agar-agar, collected inside PP containers ($\varnothing = 4.6$ cm), were used to the indirect evaluation of their relative resistivity, by measuring their impedance using similar electrode configurations (figure 16). The resistivity approximated evaluation is made according to equation 8, considering that the real part of the impedance is proportional to the resistivity.

$$R = \frac{\rho L}{A} \quad (8)$$

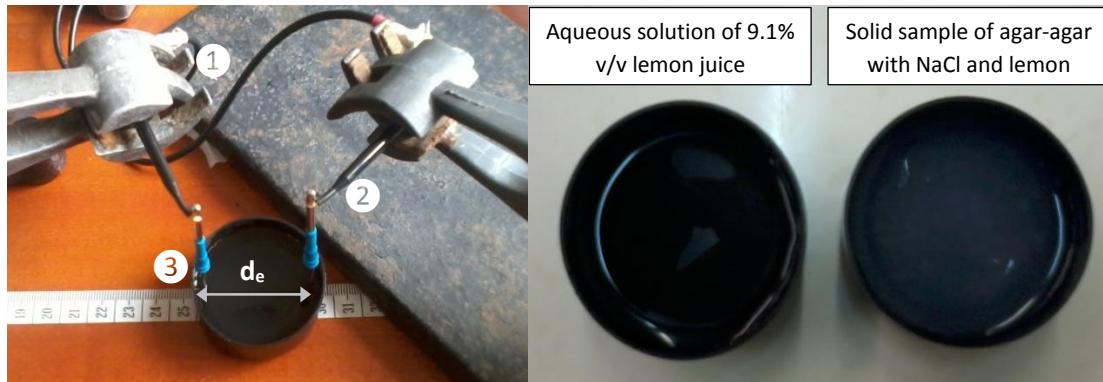


Figure 16) Set up for measuring the impedance (left) of 20 ml samples of solution and agar-agar inside PP containers (right): (1) holder claw, (2) EIS system grip and (3) needle electrodes. (Mean $d_e=3.71$ cm and ~ 0.5 cm from the point of contact with the grip to the electrode top.)

The agar-agar sample impedance was also measured outside the container, on a glass surface (Pyrex), to test the container's effect.

The electrode configuration was kept as constant as possible by using holder claws to help maintaining the distance between the electrodes and their vertical insertion into the samples. It was verified that little variations in the distance between the electrodes introduced notorious variations in the impedance reading. The length of the needle inside the sample also affected the results, although in a less pronounced way. The vertical variation of the point where the needle would contact the grip did not show appreciable effects on the result. The absolute error associated with the variation of the electrode disposition from measurement to measurement was estimated in 0.1 cm, accounting only 2.7% of the distances between them, in the range 3.69-3.75 cm.

The results (figure 17) from comparing the measurements on the agar-agar 20 mL samples inside and outside the PP containers, showed that the container induced a maximum increase of 13% in the resistance, relatively to the value measured on the glass surface. Obviously, such effect was not evaluated on the liquid samples. Since the purpose of using 20 mL samples was to obtain normalized values of impedance, assuring that the resistivity of the solid sample was lower than the liquid one (figure 18), the error introduced by the container was ignored, since all values would be inflated in the same direction, which would not affect the ratio between the impedance of internal and external phantom components.

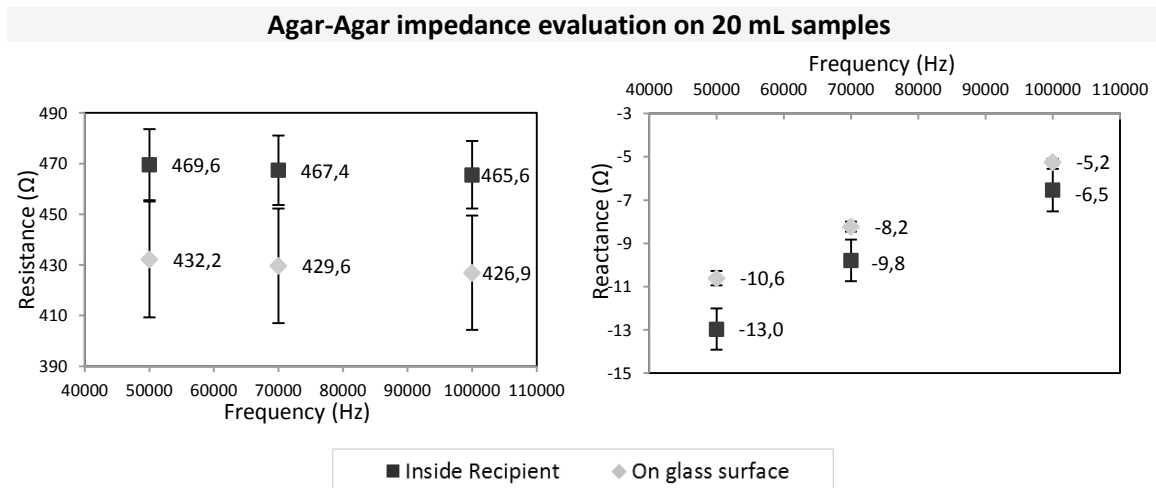


Figure 17) Agar-Agar impedance evaluation on 20 mL samples: Average values from two phantoms with similar formulations. The error bars reflect the standard error of the mean.

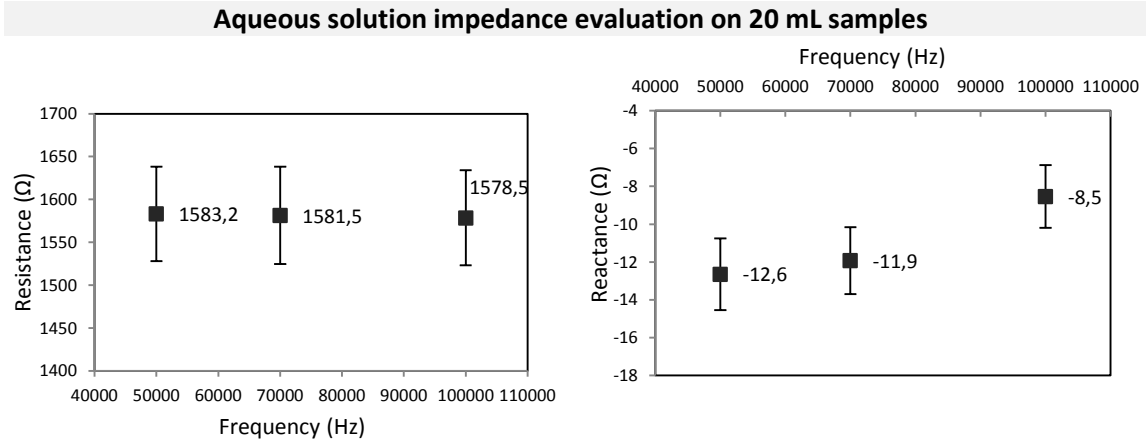


Figure 18) Aqueous solution impedance evaluation on 20 mL samples: Average values based on samples taken from two phantoms with similar formulations. The error bars reflect the standard error of the mean.

After the initial evaluation confirmed the expected relative resistance values, and before being included into the aqueous solution, the agar-agar volume (V) was estimated based on the mold diameter (D) and the measurement of their average height (h) using a caliper (table 6), according to equation 9. The errors in the direct measurements were estimated based on the visual evaluation of the maximum uncertainty for each situation, since the error associated to the caliper measurement did not reflect the real procedure limitations.

$$Volume (V) = \frac{\pi D^2}{4} h \quad (9)$$

The uncertainty on the volumetric values (δV , equation 10) of the agar- agar on table 6 was obtained by error propagation, according to the next expression, where δD , and δh are the uncertainties of the diameter and height of each sample, respectively.

$$Volume\ uncertainty\ (\delta V) = \frac{\pi D}{2} \sqrt{h^2 \delta D^2 + \frac{D^2 \delta h^2}{4}} \quad (10)$$

The aqueous solution volume was measured using a graduated syringe, and the uncertainty of the measurement was considered as the smaller scale division of the syringe to account for adherence processes.

Table 6) Phantoms volumetric description: the volumes of aqueous solution and agar-agar are indicated.

Sample	Mold diameter, D (cm)	Phantom 1		Phantom 2	
		Height, h (cm)	Volume, V (ml)	Height, h (cm)	Volume, V (ml)
Aqueous solution	-	-	250 ± 2	-	250 ± 2
Agar v1	4.02 ± 0.10		15.61 ± 6.39		15.23 ± 6.39
Agar v2	5.00 ± 0.10	1.23 ±	24.15 ± 9.86	1.20 ±	23.56 ± 9.86
Agar v3	5.59 ± 0.10	0.50	30.19 ± 12.32	0.50	29.45 ± 12.32
Agar v4	6.63 ± 0.10		42.46 ± 17.31		41.43 ± 17.31

Chapter 3: Phantom Setup

After securing the EIS system electrodes on two supports with claws above a round PP container ($\varnothing = 17.5$ cm) (figure 19), the aqueous solution was added to the container and its impedance was measured. The aqueous solution volume was enough to vertically bath the agar-agar masses, without going over them.



Figure 19) EIS system and experimental set-up: (1) laptop running a Matlab® based user interface for data processing; (2) PicoScope® acquisition interface and signal conditioning unit of the EIS system with electrode grips to grab the needle electrodes in contact with the samples; (3) Phantom.

To make sure the electrodes would not move in a significant way from measurement to measurement, two squared marks were placed at the bottom of the container, on the outside. The central points of the squared marks were 14.5 cm apart and the maximum deviation of the distance between electrodes from that value was confined to 0.7 cm – the width of each mark – between measurements. A third mark was placed in the center of the container to assure the central placement of the agar-agar masses.

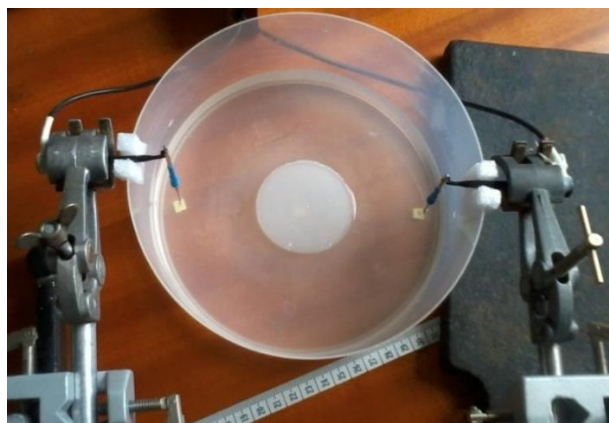


Figure 20) Detail of the phantom setup: central mass of agar surrounded by the aqueous solution. The needle electrodes are held beneath the marks location on the bottom of the container.

Due to practical constraint - to prevent the movement of the whole system -, the aqueous solution volume was not completely substituted between measurements within the same phantom, with different agar-agar masses, but only adjusted.

One agar-agar mass at a time was included in the solution with the assistance of a spatula and for each of them an equivalent volume of solution was removed. The solution volume was reposed to 250 mL at the end of each measure after one agar mass was removed and before another was included. There were performed auxiliary measurements in the phantom with each of the agar-agar masses within the complete 250 mL (before the volume adjustment) to make sure the same impedance evolution would take place.

To assure that the variation of resistivity or volume along the procedure would not affect the results, the solution impedance was measured again after taking the last agar sample off and reposing the 250 mL of solution.

To avoid damaging the agar-agar masses their impedance was only evaluated after being bathed in the solution. Such evaluation was performed by disposing the agar samples above a glass surface and inserting the needle electrodes vertically into the sample, at approximately 0.25 cm from their periphery – in a configuration similar to that shown in figure 16.

3.2. Results and discussion

The resistance ratio between the external and internal medium had an average value of 3.38, considering data from the impedance evaluation on the 20 mL (figure 17 and figure 18), which is a close approximation to the physiological ratio.

The final evaluation of the aqueous solution showed a decrease of the resistance values in both phantoms (table 7). For the first phantom, the resistance variation was not significant since it was inferior to the variation induced by the smaller agar-agar volume. For the second phantom, the variation of resistance was more relevant, presenting a variation almost as high as the one measured with the larger agar-agar mass. The resistance decrease can be justified based on an erroneous adjustment of the final volume or in the resistivity alteration due to contamination of the sample. This does not invalidate the results since the overall resistance variation due to the agar-agar masses was higher.

Chapter 3: Phantom Setup

Table 7) Impedance properties of the aqueous solution alone on the phantom container, at the beginning and at the end of the measurements. The uncertainties reflect the standard error of the mean.

Aqueous solution	f (kHz)	Phantom 1		Phantom 2	
		R (Ω)	X (Ω)	R (Ω)	X (Ω)
Initial phantom content	100	2063.3 \pm 0.1	-20.9 \pm 0.5	2044.3 \pm 0.2	2.2 \pm 0.3
	70	2075.5 \pm 0.5	-29.7 \pm 0.2	2049.3 \pm 0.4	-7.1 \pm 0.2
	50	2085.9 \pm 1.3	-34.1 \pm 0.3	2052.8 \pm 0.4	-11.4 \pm 0.1
Final phantom content	100	2012.5 \pm 1.6	-18.2 \pm 0.5	1855.5 \pm 0.4	0.9 \pm 0.3
	70	2022.0 \pm 0.3	-25.8 \pm 0.1	1858.3 \pm 0.1	-5.9 \pm 0.2
	50	2028.8 \pm 0.8	-28.9 \pm 0.8	1860.4 \pm 0.4	-11.0 \pm 0.3
Average Δ	-	53.8 \pm 1.5	3.9 \pm 0.6	190.7 \pm 0.8	0.94 \pm 0.2

Since all agar-agar solid components included in the phantoms were made from the same material it was expected that the greater their volume (and consequent diameter) the higher the resistance.

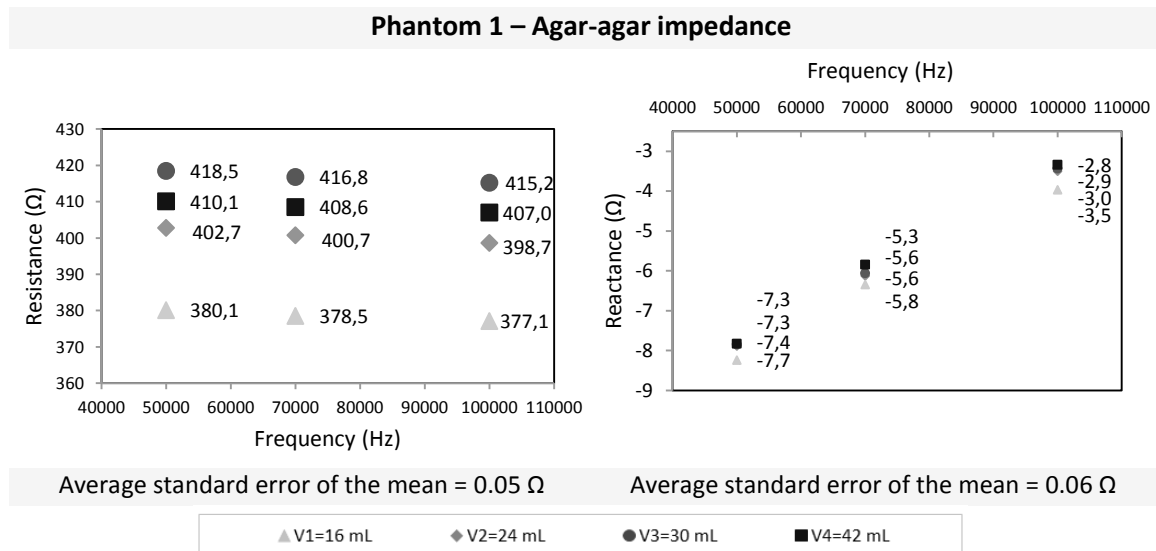


Figure 21) Impedance evaluation on individual agar-agar volumes from phantom 1: Resistance (left) and reactance (right) as a function of the excitatory frequency. The distances between the electrodes during the measurements were: 3.54 cm, 4.4 cm, 4.95 cm, 6.21 cm for v1, v2, v3 and v4, respectively.

The impedance evaluation of the agar-agar volumes showed an abnormal high resistance value on the sample V3 from phantom 1, with a value that surpassed the resistance of V4 (figure 21). This was probably due to contamination of the sample in the process of inclusion onto the phantom. All the other values behave as expected.

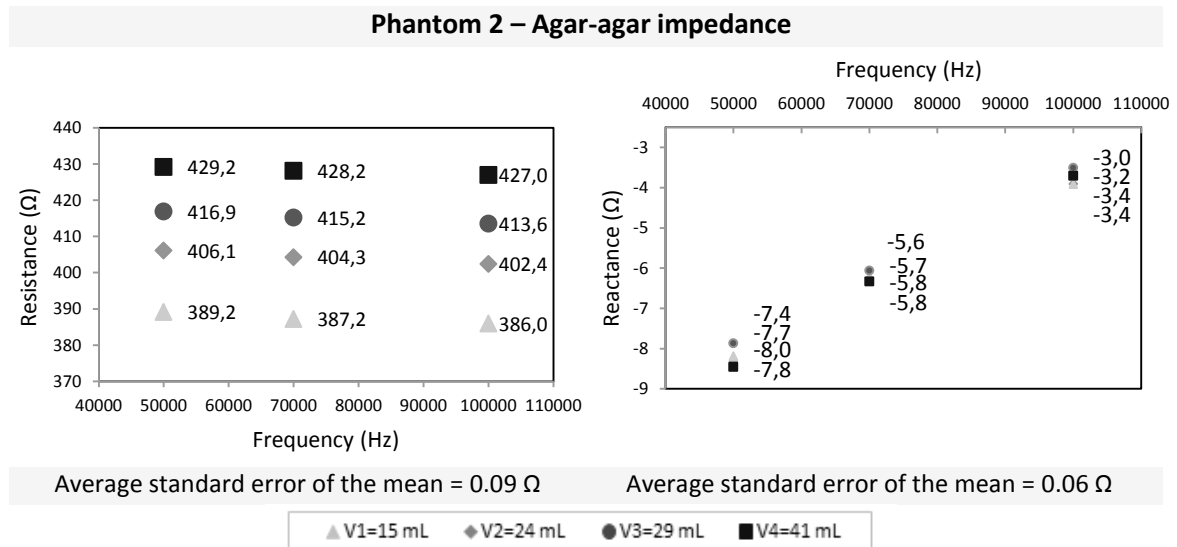


Figure 22) Impedance evaluation on individual agar-agar volumes from phantom 2: Resistance (left) and reactance (right) as a function of the excitatory frequency. The distances between the electrodes during the measurements where: 3.5 cm, 4.41 cm, 5.01 cm, 6.15 cm for v1, v2, v3 and v4, respectively.

In the second phantom, the resistance values from the agar-agar samples increased with the samples volume (figure 22), as expected. In both phantoms, the reactance values do not show a clear relation with the sample volume, presenting similar values at the same excitatory frequency.

The following data corresponds to the average of the two phantoms (at the same frequency, volume and measurement setup conditions) for ease of visualization. The agar-agar volumes were also averaged. The error values presented are a good reflection of the concordance between phantoms. In figures 23 and 24, the value at V=0 mL corresponds to the initial measurements on the aqueous solution, without any agar-agar mass.

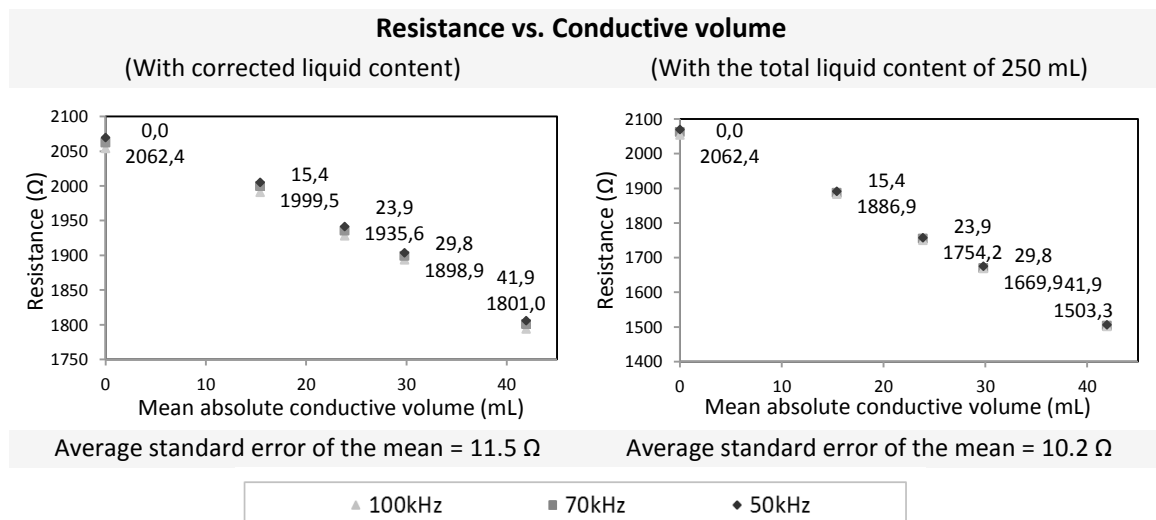


Figure 23) Phantom resistance as a function of the conductive volume for measurements after adjustment of the liquid volume (left) and with the total liquid content of approximate 250 mL (right). Each label indicates the resistance value at 70 kHz.

The measurements performed on the samples surrounded by 250 ml of aqueous solution, shown an evolution similar to that verified for the measurements performed after removing a volume of solution similar to the agar-agar mass (figure 23). The resistance values with full volume were lower than the ones with the adjusted value, which is related to the larger contact surface presented by the agar-agar mass to the solution when the liquid level is higher.

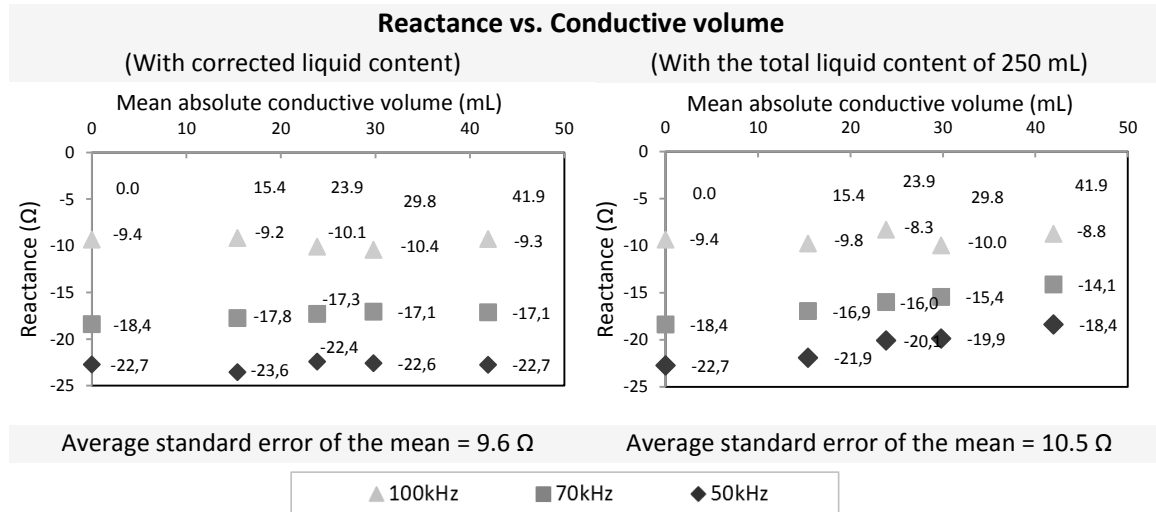


Figure 24) Phantom reactance as a function of the conductive volume for measurements after adjustment of the liquid volume (left) and with the total liquid content of approximate 250 mL (right).

Although reactance has shown a slight tendency to become more positive with the volume (figure 24), the results were not conclusive when studying each phantom individually. An odd observation was made when examining the reactance values from phantom 2, since at 100 kHz the aqueous solution shown an inductive behavior ($X > 0 \Omega$) (table 7), which would propagate to the measurements with the agar-agar volumes. This was verified only on this phantom, on the initial measurement inside the phantom container and on the final measurement as well, but not on the measurements on the 20 mL samples. The cause of such behavior is not clear, but it seems to have introduced an offset on the reactance values relative to the phantom 1, dislocating them closer to zero. The uncertainty values presented on figure 24 are close to the absolute value of the average reactance, capturing the incongruence between the two phantoms at this point.

In general, the evolution of resistance and reactance of this biological material with the excitation frequency was in accordance to the expected (section 2.2). The resistance varies inversely with the excitatory frequency, since the energy of the signal increases at high frequencies making it easier to cross the material interfaces. The system components seem to

present an overall capacitive behavior with negative reactance, as verified by the preliminary tests on the 20 mL samples. In this case the reactance absolute value varies inversely to the frequency, i.e. the negative value becomes closer to zero with the increase of frequency. The reactance evolution is related to the material behavior at higher frequencies being similar to a capacitor, which approaches a short circuit – small opposition to the current flow - with increasing frequency (section 2.2).

The impedance values for different phantoms did not overlap precisely and some odd events were spotted, but the overall direction of the impedance variations was coherent. Some anomalies might be related to the method intrinsic limitations imposed by the weighting scale and volumetric material. Furthermore, the agar-agar for food applications is not driven to this type of applications and can easily create structures with altered densities which effect cannot be easily described.

The registered variations of impedance, from one measurement to another, could not be successfully related to the variation of volume for consecutive measurements – a limitation of using a static phantom that presents very discontinuous values. Based on the linear variation of resistance with the variation of the agar-agar volumes in both phantoms, can be concluded although that the overall impedance (real component) of the phantom decreases with the volumetric increase of its most conductive component, as expected.

Chapter 4

Impedance Cardiography Acquisition System

Throughout this chapter the system developed to perform ICG monitoring will be presented.

The Arduino® microcontroller board is introduced as a part of the hardware. The basic operation of the AD5933 – integrated impedance meter – is explained in order to understand the need to adapt it to the ICG demands, namely: current injection and voltage sensing through high impedance inputs using a tetrapolar electrode configuration, DC bias elimination and small impedance measurement. The circuit developed to answer such needs is presented then, as well as the calibration process with its intrinsic limitations. The commercial ECG front-end operation is also explained.

The firmware intercom with the hardware and the Matlab® GUI, which allows the control of the acquisition procedure, is explained.

The Matlab® GUI and its capabilities are then presented.

Contents

4.1.	Hardware.....	38
4.3.	Firmware	54
4.4.	Software	57

The developed ICG system includes the hardware to acquire impedance and ECG signals, the firmware to control the data collection and the software interface to initially define the operation parameters and display the relevant data returned after basic pre-processing (figure 25).

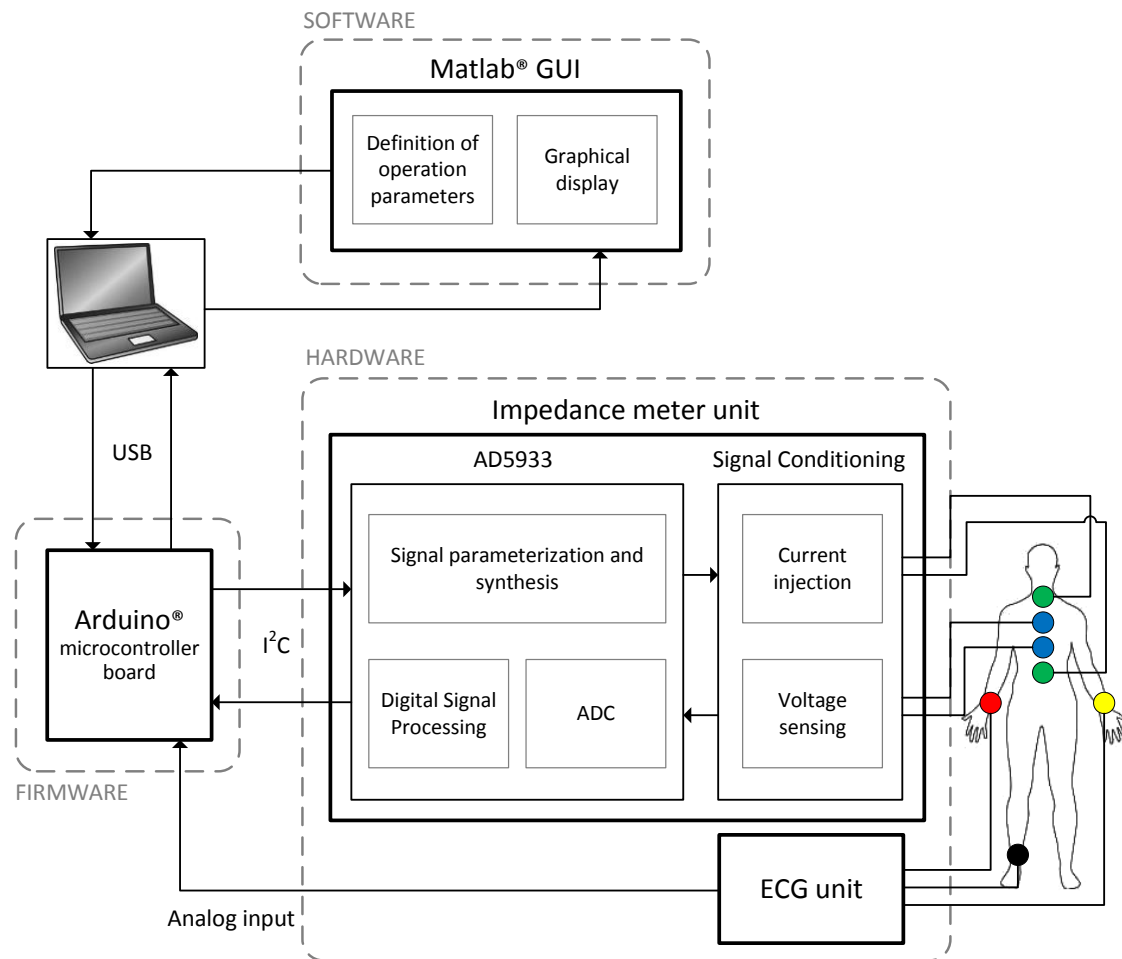


Figure 25) ICG system: simplified functional diagram describing the information flow between software, firmware and hardware.

4.1. Hardware

The ICG system's hardware can be subdivided into three main units: the impedance meter module, the ECG module and the microcontroller board that interacts with the other modules and runs the firmware for handling the data collection. The main focus of this work was to develop the impedance meter module, while the ECG acquisition was encompassed with a simple commercial front-end.

4.1.1. Arduino® Mega 2560 – microcontroller board

The Arduino® Mega 2560 board (figure 26) includes several resources that were employed in this system. The board is clocked internally at 16 MHz. The I²C interface allows the communication with the integrated impedance analyzer (AD5933) at 400 kHz. The on-board 10 bit, 9.6 kSPS ADC samples the ECG signal between 0-5 V delivered at one of its analog inputs. The microcontroller handles the data acquisition from the ECG and impedance units and its serial communication to the PC at 115.2 kbps, via USB. The board is supplied with 9 V through a power pin and converts it internally to 5 V, the working voltage. It also supplies the AD5933 with 3.3 V. The digital pins were only used for test purposes.

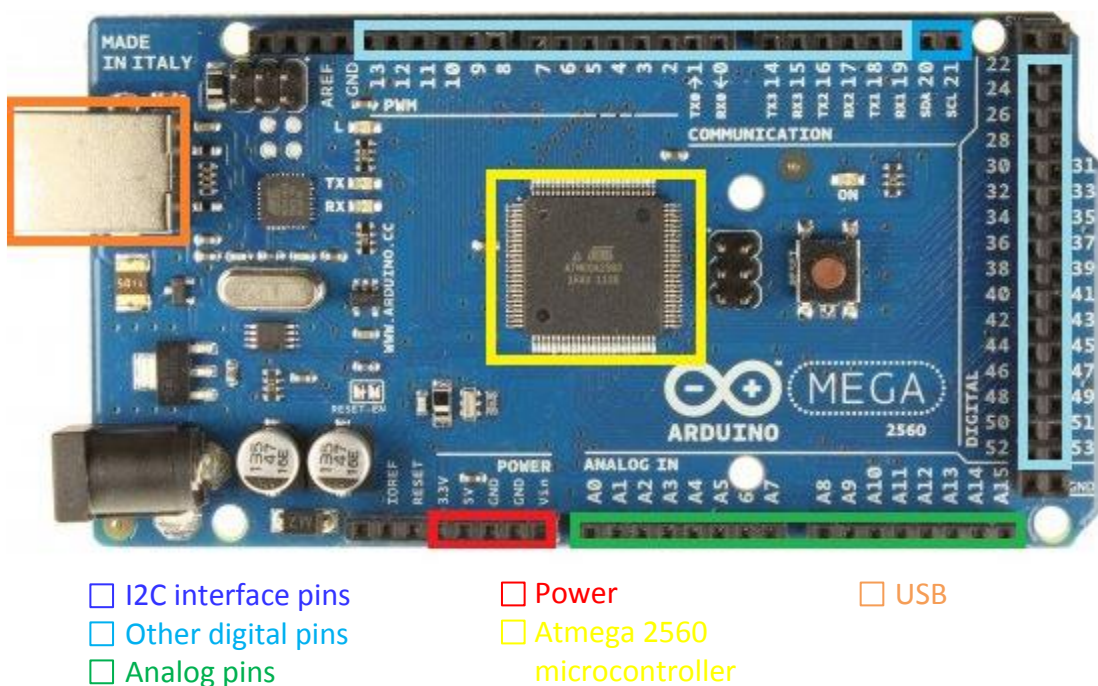


Figure 26) Arduino® Mega 2560 board relevant components.

4.1.2. Impedance meter unit

The impedance meter unit was built around an integrated impedance spectrometer, the AD5933 from Analog Devices. This chip was associated with an extension circuit in order to perform the medium excitation using an AC-current and the voltage sensing through high impedance inputs, in a tetrapolar electrode configuration, while adjusting the system to operate inside the limits for human safety.

4.1.2.1. AD5933 - Integrated impedance analyzer

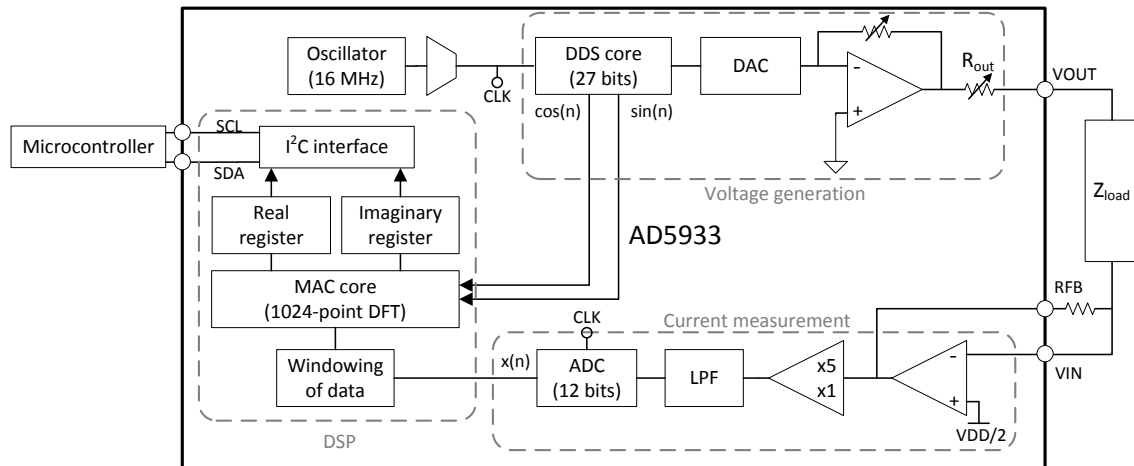


Figure 27) AD5933 simplified functional block diagram depicting its basic operation configuration.

The AD5933 [62, 63] is a fully integrated impedance measurement system (figure 27) configurable through a low level I²C serial interface [64]. In its basic configuration, the AD5933 can measure impedance values from 100 Ω to 10 M Ω , with an accuracy of 0.5 %, for excitation frequencies from 1 kHz to 100 kHz, with a frequency resolution down to 0.1 Hz [62]. The operation procedure consists on exciting an unknown complex impedance (Z_{load}) with a known controlled voltage and frequency, then measuring the current flowing through it to compute its complex (real and imaginary) Discrete Fourier Transform (DFT) coefficients in order to obtain the Z_{load} components. The measurement can be repeated for the desired excitation frequencies by commanding the I²C interface. The system is typically applied to perform spectroscopic analysis using a frequency sweep, but a single frequency operation can be achieved programmatically.

The voltage generation stage of the AD5933 includes a programmable direct digital synthesis (DDS) core that numerically synthesizes a sinusoidal signal at a defined frequency [65], converted by a digital-to-analog converter (DAC) into an analog waveform. The analog output undergoes a programmable gain stage that defines the peak-to-peak value of the output excitation signal made available at the VOUT pin, centered on a typical positive DC bias. The output impedance of the AD5933 at the maximum peak-to-peak voltage (1.98 V_{p-p}) is 200 Ω .

The current signal generated across Z_{load} is forwarded to a current-to-voltage amplifier, in the current measurement stage, presenting at the VIN pin a virtual ground with a DC value set to half the supply voltage (VDD/2). The current flows into VIN developing a voltage signal at the amplifier output, with a gain externally defined by the feedback resistance (R_{FB}), connected between RFB and VIN. The programmable gain amplifier (PGA) that follows,

allows the multiplication of the output by a factor of 1 or 5. The signal is low pass-filtered by an antialiasing filter and then presented to the input of a 12 bit, 1.04 MSPS analog-to-digital converter (ADC), that passes the digitalized results to the digital signal processing (DSP) engine. The R_{FB} value and the PGA gain must be selected in order to maintain the signal within the linear range of the ADC (0V to VDD). The delay ($\Delta t_{settling}$) between the moment the DDS core is commanded to generate a waveform at specified frequency (f) and the time the ADC starts sampling a new impedance point (equation 11) is defined by the number of settling time cycles (N_s) programmed into the device.

$$\Delta t_{settling} = \frac{1}{f} \times N_s \quad (11)$$

The system clock, for the DDS and ADC, is generated by the internal oscillator with a typical frequency of 16.776 MHz or, otherwise, provided externally.

The multiply accumulate (MAC) core performs the DFT over 1024 samples, at each frequency, to determine the spectral power of the measured current. The calculation is based on the algorithm described by equation 12, where $X(f)$ is the power of the signal at the frequency f, $x(n)$ is the ADC output and $\cos(n)$ and $\sin(n)$ are sample vectors provided by the DDS core at the frequency f, that carry information related to the output excitation signal.

$$X(f) = \sum_{n=0}^{1023} \left(x(n) \times (\cos(n) - j\sin(n)) \right) \quad (12)$$

The real (R) and imaginary (I) components of the result, at each frequency, are stored in memory, encoded in the two's complement format and the data registers can be accessed through the I²C interface. These are not the resistive and reactive components of the impedance under test: the DFT coefficient is an image of the complex input current and for that reason is inversely proportional to the (amplitude) value of the unknown impedance. The non-calibrated values of amplitude and phase (in radians) are computed using equations 13 and 14.

$$Amplitude = \sqrt{R^2 + I^2} \quad (13)$$

$$Phase = \tan^{-1} \left(\frac{I}{R} \right) \quad (14)$$

When using the arctangent formula to calculate the phase at each point the correct phase angle is returned only when the sign of the R and I components are both positive. To obtain the standard phase angles taken counterclockwise from the positive real x-axis the corrections in table 8 must be applied.

Table 8) Corrected phase angles [62].

Real component	Imaginary component	Quadrant	Correct phase angle
Positive	Positive	First	$\tan^{-1}\left(\frac{I}{R}\right)$
Negative	Positive	Second	$\tan^{-1}\left(\frac{I}{R}\right) + \pi$
Negative	Negative	Third	$\tan^{-1}\left(\frac{I}{R}\right) + \pi$
Positive	Negative	Fourth	$\tan^{-1}\left(\frac{I}{R}\right) + 2\pi$

4.1.2.1.1. Calibration procedure and impedance calculation

The AD5933 requires an initial calibration process, in which a known resistor (R_{cal}) is placed between VOUT and VIN and two corrective factors for the amplitude – gain factor - and phase – system phase - are calculated for subsequent measurements. The R_{cal} value should be a midpoint of the impedance range of interest to account for the gain introduced by the ratio of R_{FB}/Z_{load} (ideally unitary gain). The gain factor is obtained from the R_{cal} value and the raw amplitude returned by equation 13, through the following expression. The gain factor is affected by the R_{FB} value, the output excitation voltage, the PGA gain and the frequency.

$$Gain\ factor = \frac{1}{R_{cal} \times Amplitude} \quad (15)$$

The phase measured by the AD5933 accounts the phase introduced across the whole signal path, along with the phase through the analyzed impedance. When a purely resistive load is placed at the AD5933 terminals the phase measured is completely due to the internal influence of the system components (equation 16).

$$System\ phase = Phase, \quad when\ Z_{load}\ is\ purely\ resistive. \quad (16)$$

After calculating these parameters, the true amplitude ($|Z_{load}|$) and phase (θ_{load}) of any unknown impedance are obtained using the following expressions, where amplitude and phase refer to the raw values obtained at each measurement from equations 12 and 13, respectively.

$$|Z_{load}| = \frac{1}{Gain\ factor \times Amplitude} \quad (17)$$

$$\theta_{load} = Phase - System\ Phase \quad (18)$$

4.1.2.1.2. Operation parameters

The typical values adopted for the operation of the AD5933 in the present system are specified in table 9, the details about their definition process are given in the firmware section, 4.2.

Table 9) AD5933 operation parameters – typical values.

Power Supply	3.3 V
Output signal frequency	50 kHz, 70 kHz or 100 kHz
Output peak-to-peak voltage	1.98 V _{p-p}
PGA gain	1
Number of settling time cycles	5
System Clock	16.677 MHz internal clock

4.1.2.2. Signal conditioning circuit

The AD5933 has been used in biological applications to perform electrical bioimpedance spectroscopy [66, 67, 68, 69, 70] and also ICG single frequency measurements [49].

Several circuit extensions to the AD5933 are proposed in the literature to adapt the chip to different purposes: allow the measurement of impedances connected to the ground [71]; allow the operation in a tetrapolar configuration [66, 68, 70, 49]; extend the impedance measurement range [67, 72, 73]; perform the load excitation using a current signal [72]; remove the signal DC bias to prevent electrolysis on biological tissues [74].

In the present case, the changes to the normal operation of the AD5933 were made in order to complete the following requirements:

- Convert the voltage excitation signal at the AD5933 output into a current encoded signal obeying to the ICG guidelines (section 2.4.1);
- Minimize the output DC bias current to avoid the medium polarization (section 2.4.1);
- Allow the use of a tetrapolar electrode configuration to reduce the influence of parasitic impedances from the interface electrode-skin (section 2.5);
- Enable the measurement of impedances in the ICG range of interest (Appendix A);

The extension circuit removes the DC voltage bias from the AD5933 output and feeds the signal to a voltage controlled current source (VCCS) that pursues the voltage-to-current conversion. The DC residual currents at the VCCS output are minimized by an AC-coupling circuit before the signal is delivered to the biological medium. The instrumentation amplifier senses the voltage differential generated across such impedance through high impedance

inputs and restores the DC component required for the AD5933 operation. The voltage output is converted to current by a series resistor.

For the complete presentation of the impedance meter circuit please refer to Appendix C.

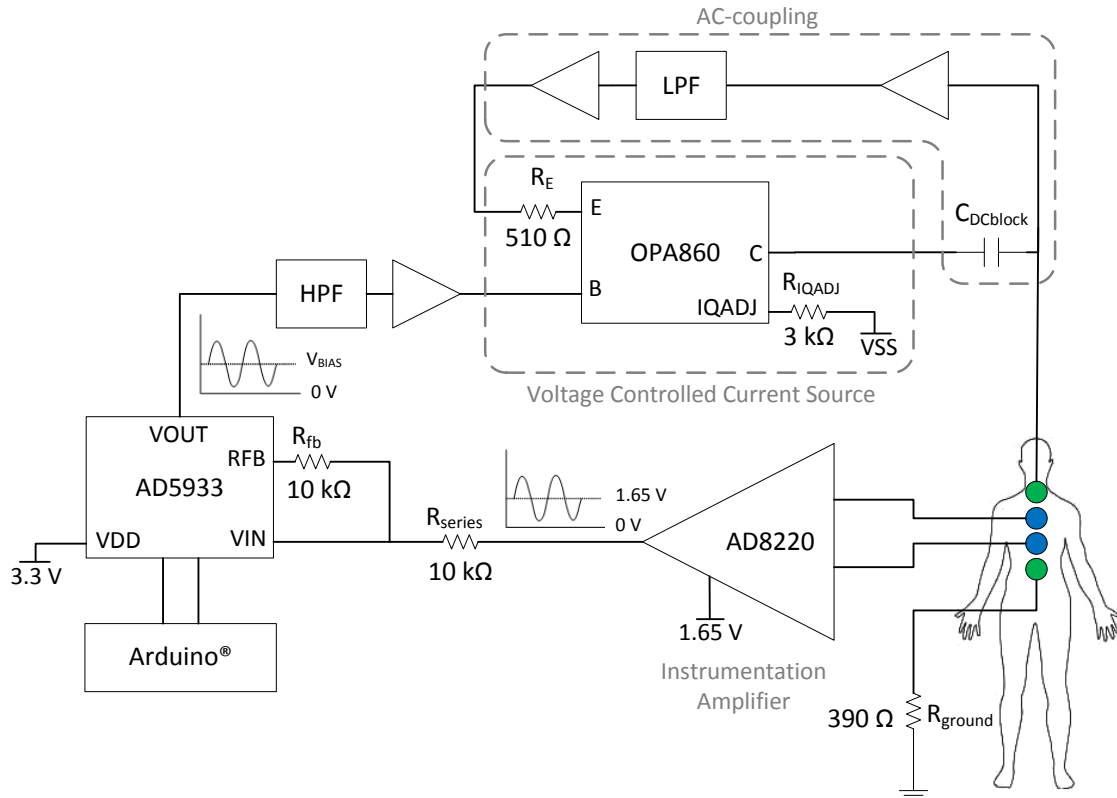


Figure 28) Signal conditioning circuit. Current injection and voltage sensing electrodes are presented in green and blue, respectively.

The first stage of the conditioning circuit (figure 28) encompasses a passive high pass filter, with a cutoff frequency of 3.4 Hz, which removes the typical DC bias from the AD5933 voltage output signal. To buffer the filter output – as well as for the other buffers on board - the TLC074 [75] operational amplifier with low input noise and high input impedance was employed, preventing currents from flowing from the ground.

The voltage-to-current conversion stage is based on the OPA860 VCCS [76]. It presents three terminals: a high impedance input (base, B), a low impedance input/output (emitter, E) and a current output (collector, C). In the presented configuration, the VCCS operates as a second generation positive current conveyor [77]: the input voltage applied on the input B is conveyed to E and the current generated through the emitter resistance (R_E) is conveyed to the C output. If B presents a positive voltage relative to E, the current flows out of the C output, otherwise if B presents a negative voltage relative to E, the current flows into the

C output, more explicitly a current flowing out of E will generate a current flowing out of C. The VCCS is non-inverting because of the sense of the output current.

In accordance to Ohm's law, the theoretical amplitude of the output current (i_C) can be obtained by multiplying the amplitude of the input voltage (v_B), ideally half the peak-to-peak voltage output defined for the AD5933, for the R_E value. Following this, the R_E value was chosen in order to generate an excitation current with typical amplitude of 1.94 mA, in accordance to the ICG typical current limits.

The adjustment of the external resistor (R_{IQADJ}) allows optimization of bandwidth, quiescent current and voltage-to-current gain trade-offs of the VCCS. The reduction of the quiescent current, by means of a large R_{IQADJ} value, increases the output impedance at C, which minimizes the current variation for a range of impedance loads. This is an important point since the system correct operation relies on the precise current maintenance. The effect of a low quiescent current on the bandwidth is not relevant for the frequency range of interest.

The inclusion of a DC-blocking capacitor ($C_{DCBlocking}$) at the VCCS output is mandatory, in order to prevent applying DC currents into the subject. This capacitor along with the impedance of the next stage forms a high pass filter, performing a passive AC-coupling process. An intrinsic problem to bioimpedance measurements is the charging of the DC-blocking capacitor due to residual DC currents related to electrode polarization, causing the saturation of the source output. To overcome this problem a DC feedback loop was implemented around the VCCS, following a principle widely described for similar systems [58, 78, 79]. The voltage at the DC blocking capacitor output is sensed and low pass filtered at 30 Hz with a passive filter to extract the DC component that is fed back into the VCCS emitter. This originates at the collector a current contrary to the one causing the DC-bias sensed voltage in the first place. The circuit performs an active correction of the DC component maintaining the output close to 0 mA.

The current applied to the load, through the high current electrode, is then recovered at the low current electrode that conduces it across a grounded resistor (R_{ground}). The R_{ground} was included to maintain a stable VCCS output current, which occurs for load impedances higher than 390 Ω (section 5.1). The voltage generated across the load, in response to the applied current, is sensed through the receiving electrodes at the high impedance input pins of the AD8220 instrumentation amplifier [80]. Since near no current passes through these electrodes the parasitic effect of the electrode-skin interface in the voltage measurement is minimized. The high CMRR - near 60 dB for the frequency range of interest – minimizes common mode interferences, discounting the effect of any DC residual component that may arise. The AD8220 was used with unitary gain. The differential AD8220

output is referenced to 1.65 V, to repose the DC bias obeying to the AD5933 requirements. The reference is generated by an auxiliary circuit that provides ± 3 V to the terminals of a variable resistor allowing the trimming of the required voltage.

The voltage output from the AD8220 passes through the series resistance (R_{series}) generating the current fed to the AD5933. In order to pass the voltage signal with unitary gain through the AD5933 current –to-voltage amplifier, the values of feedback resistance (R_{FB}) and R_{series} are equal. The value of R_{series} was choose to maintain the current generated across this resistor by the voltage output of the AD8220 (with amplitudes in the range of 0-1.65 V), inside the interval of currents expected to be generated by the defined AD5933 voltage output across the range of impedances it can measure in its original configuration (section 4.1.2.1). For $Z_{load}=10 \Omega$, the relation between the voltage output and current input of the AD5933 - considering the ideal current output from the VCCS and the ideal voltage output from the AD5933 - results on a resistance of 0.5 M Ω , for $Z_{load}=815 \Omega$, the resistance seen by the AD5933 is 6.3 k Ω .

The particularities of this system made necessary the development of an adjusted calibration process.

4.1.2.2.1. Calibration procedure revised and impedance calculation

By injecting a current and sensing a voltage the extension circuit introduces an admittance in the signal path, i.e. considering a constant excitation current, if $|Z_{load}|$ increases the AD8220 output voltage will also increase, producing a higher current across R_{series} , and the reciprocal. This is not taken into account in the original calibration process, since the normal operation of the system expects a current drop in response to an increase in $|Z_{load}|$.

The AD5933 sees the extension circuit as a complex impedance and the current generated across R_{series} , in response to the voltage output of the AD8220, is acquainted as the response of the complex impedance to the excitation voltage at VOUT. This way the variation of the AD8220 voltage output is seen by the AD5933 as a variation in the R_{series} value.

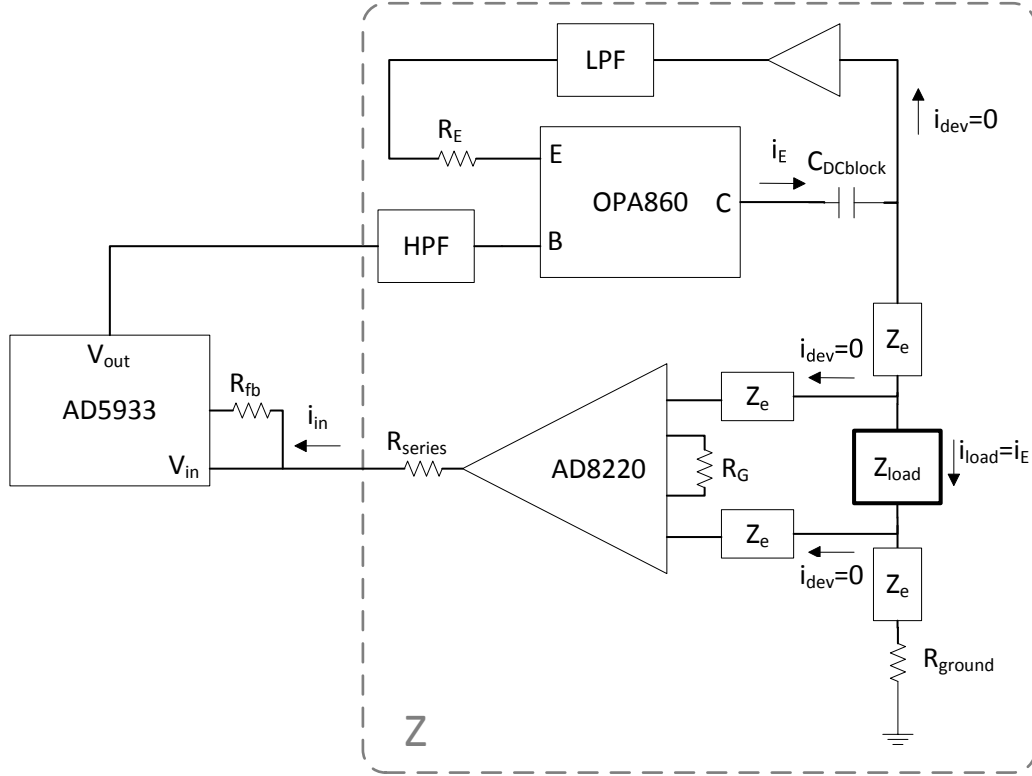


Figure 29) Simplified impedance unit with relevant quantities and simplified presentation of stray components equivalent (Z_e).

The impedance value (Z), as seen by the AD5933, is the relation between the voltage output (V_{out}) and the current input (i_{in}) given by the Ohm's law. Based on the analysis of this relation some conclusions can be drawn with respect to the load impedance value (Z_{load}).

The deduction presented below (equation 19) assumes that the current output is constant and equal to the theoretical value defined by the emitter resistor (R_E) and considering that no current is deviated from its path across the load (figure 29). The AD8220 voltage output (V_{AD8220}) is considered to be the linear result of the ideal current output of the VCCS passing across the load, in accordance to the defined gain (G_{AD8220}).

$$\begin{aligned}
 Z &= \frac{V_{out}}{i_{in}} = \frac{V_{out}}{\frac{V_{AD8220}}{R_{series}}} = \frac{V_{out}}{\frac{i_E \times Z_{load} \times G_{AD8220}}{R_{series}}} = \frac{V_{out}}{\frac{V_{out} \times Z_{load} \times G_{AD8220}}{R_E \times R_{series}}} \\
 &= \frac{R_E \times R_{series}}{Z_{load} \times G_{AD8220}}
 \end{aligned} \quad (19)$$

The estimative of the load impedance (Z_{load}) is given by rearranging the last expression.

$$Z_{load} = \frac{R_E \times R_{series}}{Z \times G_{AD8220}} \quad (20)$$

Unrolling the expression into its complex exponential representation gives a better understanding of the relation between amplitude and phase of the measured impedance, Z and Z_{load} .

$$|Z_{load}|e^{j\theta_{load}} = \frac{R_E \times R_{series}}{G_{AD8220}} \times \frac{1}{|Z|e^{j\theta}} \quad (21)$$

The comparison of both sides of the expression leads to the following relations.

$$|Z_{load}| = \frac{R_E \times R_{series}}{G_{AD8220}} \times \frac{1}{|Z|} \quad (22)$$

$$e^{j\theta_{load}} = e^{-j\theta} \Leftrightarrow \theta_{load} = -\theta \quad (23)$$

This principle can be applied to correct the calibration process and the outputs during general acquisition, as follows.

Based on the equation 22, the relation between the calibration resistance (R_{cal}) and the amplitude of the impedance perceived by the system (Z_{cal}) can be obtained as follows.

$$|Z_{cal}| = \frac{R_E \times R_{series}}{G_{AD8220}} \times \frac{1}{R_{cal}} \quad (24)$$

The gain factor for the amplitude can then be derived similarly to the original procedure (equation 15).

$$Gain\ factor = \frac{R_{cal} \times G_{AD8220}}{R_E \times R_{series} \times Amplitude} \quad (25)$$

The system phase can still be considered to be the phase perceived by the system with a purely resistive component at its terminals (equation 16), with all the stray contributions across the system resulting in a constant value at a given frequency.

$$System\ phase = \theta_{cal} \quad (26)$$

The system phase is determined from the raw real and imaginary values, simply by applying the arc tangent expression (equation 14).

During acquisition the corrected amplitude and phase values are accessed based on the following expressions. The calibrated amplitude of the impedance is obtained by substituting the perceived impedance amplitude value $|Z|$ given by equation 17 on equation 22. The common factors from $|Z_{load}|$ and the gain factor expression (equation 25) could be simplified, resulting on expressions not dependent on the R_E , R_{series} and G_{AD8220} , although, they

are presented in the form they were implemented in practice. The calibrated impedance phase is the combination of equation 18, the original phase, and equation 23.

$$|Z_{load}| = \frac{R_E \times R_{series}}{G_{AD8220}} \times Gain\ factor \times Amplitude \quad (27)$$

$$\theta_{load} = -\theta \Leftrightarrow \theta_{load} = System\ phase - Phase \quad (28)$$

From the impedance amplitude and phase the resistance (R_{load}) and reactance (X_{load}) values can be calculated using the general expressions, as follows.

$$R_{load} = |Z_{load}| \times \cos(\theta_{load}) \quad (29)$$

$$X_{load} = |Z_{load}| \times \sin(\theta_{load}) \quad (30)$$

4.1.2.2.2. Calibration procedure assumptions and limitations

The calibration process formulized above relies on assumptions that must be justified. Also, the practical implementation of the calibration process will suffer from approximations that have to be analyzed.

The high pass filter, the VCCS, the DC blocking capacitor, the cables and the instrumentation amplifier, as well as the stray impedances along the current path were considered to introduce systematic errors on the impedance measurement at a specified frequency. Therefore they are accounted for in the values of the calibration parameters. The calibration model also considers a constant current supplied by the VCCS , flowing across the path to the ground, without any deviation that can cause the current that flows on the load (Z_{load}) to be different from the ideal VCCS output.

The parasitic impedances that affect the impedance measurement in the specific case of the ICG are presented on figure 30. The blocks represent complex impedances: the electrode-skin interface is described by the circuit presented on section 2.5.2, while the remaining can be identified with the RRC parallel circuit (section 2.2).

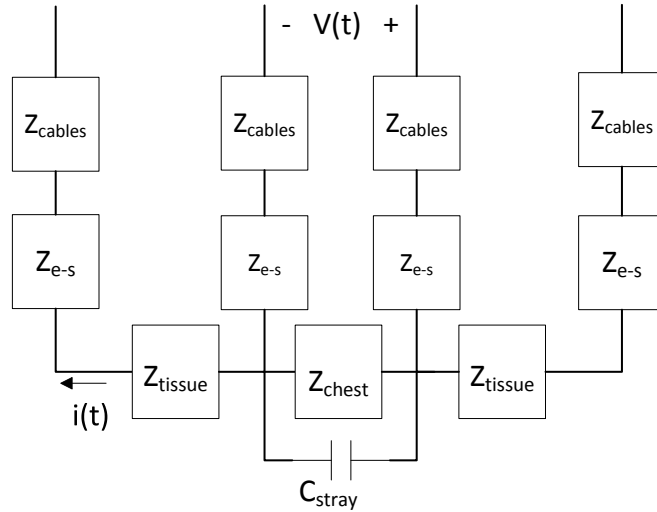


Figure 30) Equivalent electric circuit of all parasitic impedance components affecting the thoracic impedance measurement (Z_{chest}) [58, 66]: Z_{cables} corresponds to the effect of the electrode cables; Z_{e-s} is the electrode-skin interface impedance; Z_{tissue} represents the tissue in between the application and sensing electrodes.

The sensing electrodes high input impedance prevent the current from flowing through them, as explained before (section 2.5). In this particular case, the influence of the interface electrode-skin, as well as the cables parasitic capacitances have very low impact on the impedance measurement.

There are evidences that the electrode-tissue interface acts as a resistor at frequencies higher than 10 kHz [81]. The high impedance amplitude on the application electrodes can have significant impact on the precision of the system because it can affect the VCCS output, while increasing the common mode voltage at the instrumentation amplifier input [66].

The stray capacitances introduced by the cables are especially important in the application electrodes where the current flows. Their influence would probably be reduced by using a driven shield technique - not employed in the present system. Nevertheless, the effect of this protection is only evident at high frequencies ($> 10^5$ Hz) [58], revealing a little impact in the frequency range of this system.

The capacitive leakage is a deviation of the reactance value mainly observed at high frequencies, although, it affects the impedance value at every frequency. This effect is caused by parasitic capacitances (C_{stray}) primarily introduced by amplifiers and can be described by a capacitor in parallel to the load (figure 30). Parasitic capacitances in general introduce systematic errors in the impedance measurements - they can also be accounted by the calibration factors - and their influence does not drastically affect the impedance analysis at a single frequency.

During the practical implementation of the calibration procedure the spot electrode pads (section 4.1.4) cannot be used, that way the calibration resistor - with a value similar to the thoracic impedance - is directly connected between the metallic plugs at the electrode cable endings. This process accounts for the cable influences, but not for the electro-skin interface, neither for the effect of the inter-electrode tissue. The reliability of such calibration procedure is dependent on the VCCS compliance, which will define the variation of the current output with the extra impedance component. Also this procedure assumes that the calibration parameters are mainly affected by the amplitude of the load between the instrumentation amplifier terminals, which defines the leakage through the stray capacitance and produces the most important contributions on the system gain variation through the voltage drop produced.

The acquaintance of the equivalent model for the stray impedances was important to understand their effect on the impedance measurement. Although, the incomplete knowledge of the model components and the lack of a reference tetrapolar method to establish comparisons with, made the development of a test circuit based on this model unreliable.

4.1.3. ECG unit

The ECG unit is based on a commercial analog front-end that senses, amplifies and filters the ECG waveform, including an on board 50 Hz notch filter to remove the line noise in accordance to the European constraints. The output placed between 0 and 5V is directly forwarded to an ADC. The ECG electrodes are connected to 3 inputs: R, right; L, left and G, ground. The ground electrode is directly connected to the circuit ground.

The three electrodes are placed one at each arm and one on the right leg, forming the edges of the Einthoven's triangle (figure 31). The ECG records the differential voltage between any two points of the triangle. In this procedure three different leads are obtained: Lead I is measured between the left arm (+) and the right arm (-); Lead II is measured between the right leg (+) and right arm (-); Lead III is measured between the right leg (+) and the left arm (-). [18].

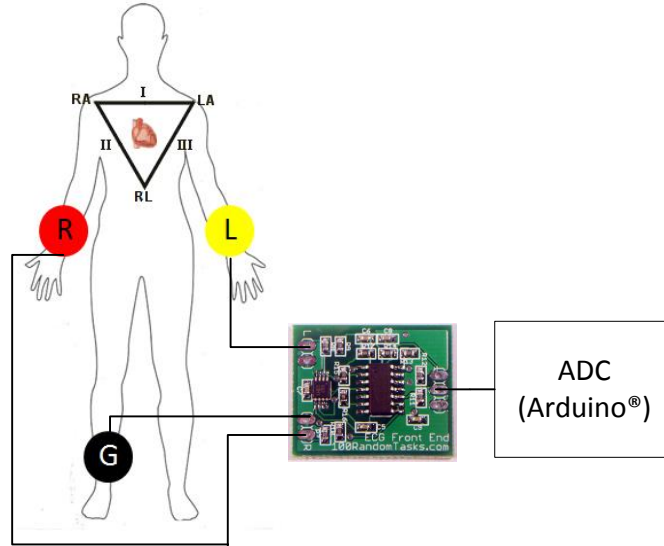


Figure 31) ECG front-end [82] and the 3-lead ECG configuration.

This ECG front-end presented some problems, when performing measurements by itself - without ICG – it would saturate when all the three electrodes were connected to the subject, but performed well while only lead I was measured.

4.1.3.1. ECG calibration method

The Arduino® ADC has a resolution of 10 bits, returning values from 0 to 1023 at each reading. The simplest way to obtain the physical quantity from these values is by using the following expression, assuming a constant supply voltage (V_{cc}).

$$V(EGG) = \frac{ADC_{value} \times V_{cc}}{1023} \quad (31)$$

The value returned directly from the ADC is referenced to the 5V supply pin on board. The referred voltage was measured during acquisitions resulting in an average value of 5.05 ± 0.01 V. Fluctuations in the supply voltage imply that at each sampled point measured the reference value can be different, for such, the overall correction considering a constant value of V_{cc} is an erroneous process. Since the ECG amplitude is not evaluated during ICG measurements it was considered the average supply voltage to perform the correction.

4.1.4. Electrode construction

The system needs 4 ICG electrodes – high current (I+), low current (I-), high voltage (V+), low voltage (V-) - and 3 ECG electrodes – right arm (R), left arm (L) and ground (G) - for its operation.

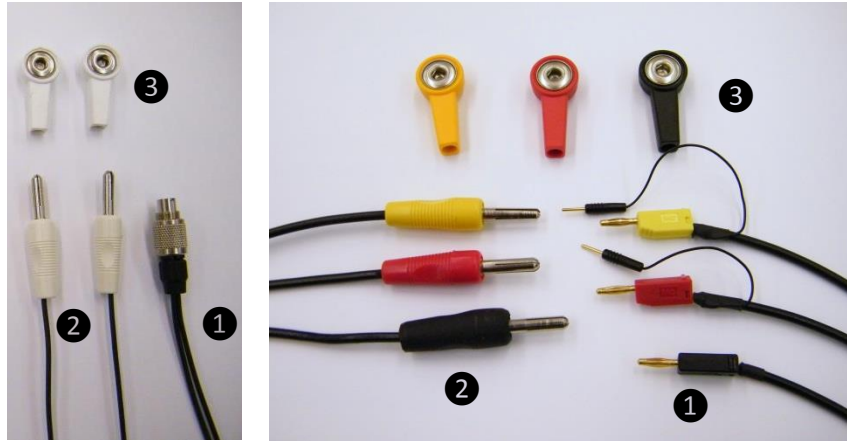


Figure 32) ICG (left) and ECG (right) electrode components: (1) plug for connection with the device, (2) plug for connection with the subject and (3) plug adapter for clip electrodes.

To optimized signal-to-noise ratio coaxial cables were employed in both cases. The ICG electrodes were constructed using 1 m long RG178 RF coaxial cables ($\varnothing=1.8$ mm, maximum resistance= $8.02 \Omega/\text{m}$ and capacitance= 98 pF m^{-1}). The ECG electrodes employed RG174 RF coaxial cables ($\varnothing=2.794$ mm and capacitance= 101 pF.m^{-1}) also with 1 m. To eliminate interferences the input of the shield conductor was grounded - except for the ECG ground. Simply grounding the shield might have been a poor solution, since for long cables the capacitance between the shield and the core remains, living the input signal vulnerable to interference. Such stray capacitance can attenuate the high frequency component of the input signal - more relevant to the ICG electrodes. The driven shield input partially cancels the capacitive effect, by putting both conductors at the same potential [83]. The plugs employed for each type of electrode are depicted in figure 32.

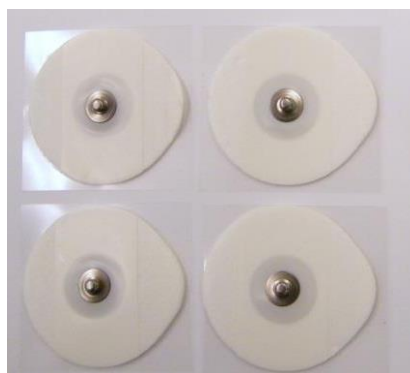


Figure 33) Pre-gelled disposable electrodes for ECG.

The electrode contact with skin was made through 48×50 mm pre-gelled disposable foam electrodes for ECG (F9060 from FIAB).

4.1.5. Printed Circuit Board Specifications

The circuit was included on a 16×10 cm printed circuit board (PCB) (figure 34), designed to satisfy the specifications of an already existing platform.

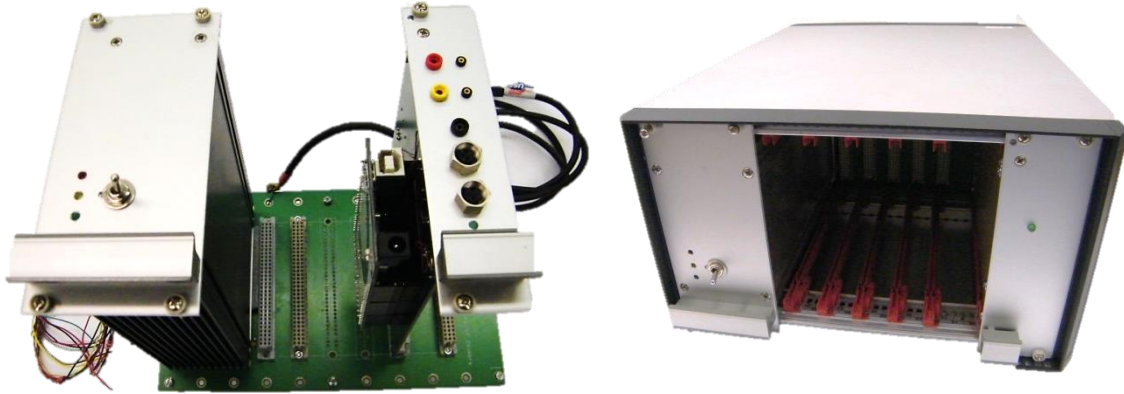


Figure 34) PCB board (middle) mounted on a test platform with voltage converting module (left), showing the frontal panel with sockets to connect the electrodes and the Arduino® board on the PCB back, and multichannel platform (right).

The multichannel platform (figure 34) has the purpose of operate several hemodynamic probes at once. This platform presents various slots where each custom made circuit board can be accommodated and plugged into a bus communication system that provides the power supply to the board and encompasses analog pins, digital pins and USB channels to establish the communication with external devices. During all the ICG system trials a test platform, analog to the multichannel platform, was used. The test platform is supplied at 12 V by an external voltage source and an intermediate circuit performs the voltage conversion to supply ± 5 V and ± 15 V to the board. The developed ICG system only uses the bus for power supply.

4.2. Firmware

The firmware that runs on the Arduino® microcontroller is triggered by a serial input from the user interface (GUI) sent via USB (figure 35). The inputs from the GUI are sent in a fixed order, along with an 8 bit identifier value. The Arduino® code waits until he receives a known 8 bit sequence, reads the parameter value associated with such identifier and in return sends the correspondent confirmation character to the GUI. The communication proceeds if the identifier and the confirmation character correspond to the values expected on either side.

The input parameters result from user definitions that need to be programmed into the firmware to set the operation mode – acquisition or calibration –, the impedance meter

excitation frequency – 50, 70 or 100 kHz - and the sampling frequency – 400 Hz maximum. In calibration mode only the impedance meter output is acquired, whereas in acquisition mode the ECG input is also sampled.

The initialization of the AD5933 is conducted following the steps on figure 35. Every time an impedance measurement is needed another request to the AD5933 has to be issued by programming a measurement repetition at the defined frequency.

The sampling frequency is established by setting a timer to operate the data acquisition at fixed periods. The minimum acquisition period (2.5 ms) was drawn based on the time elapsed between two valid measurements, which was evaluated in 1.879 ms (maximum). This evaluation was made by setting a digital pin high during the time a measurement took place – which includes the time for sending a measurement request to the AD5933, waiting till the measurement is available, read it and send the result to the serial interface, reading the analog input from the ECG front-end and send the result to the serial interface – and verifying, with the oscilloscope (Picoscope®), the time interval the digital pin was high. The code inside the timer was optimized so that the actual impedance point would be processed inside the AD5933 core in parallel to the ECG sampling/reading and read in the next cycle. This procedure also introduces a minimum delay between the time the AD5933 ADC starts sampling the impedance point and the moment the ECG point is sampled by the Arduino® ADC. Although no problems were verified when using the maximum sampling rate, a backup was included. In case the measurement is not ready and the timer needs to ignore an acquisition, the data sent to the interface (zeros) will lead to a NAN value on the impedance data and a 0 in the ECG data, informing that the acquisition was not correct.

The code inside the timer takes only 1.13 ms to run, in the remaining time the Arduino® verifies if there was a known finalization input from the GUI, if any the timer is turned down, so no more data is sampled and sent. Arduino® waits for another input from the GUI, meaning that all the data in the serial line was cleaned, and powers down the AD5933, extinguishing the excitation signal to the load. In a similar fashion as for initialization a confirmation character is sent to assure the effectiveness of the finalization.

Chapter 4: Impedance Cardiography Acquisition System

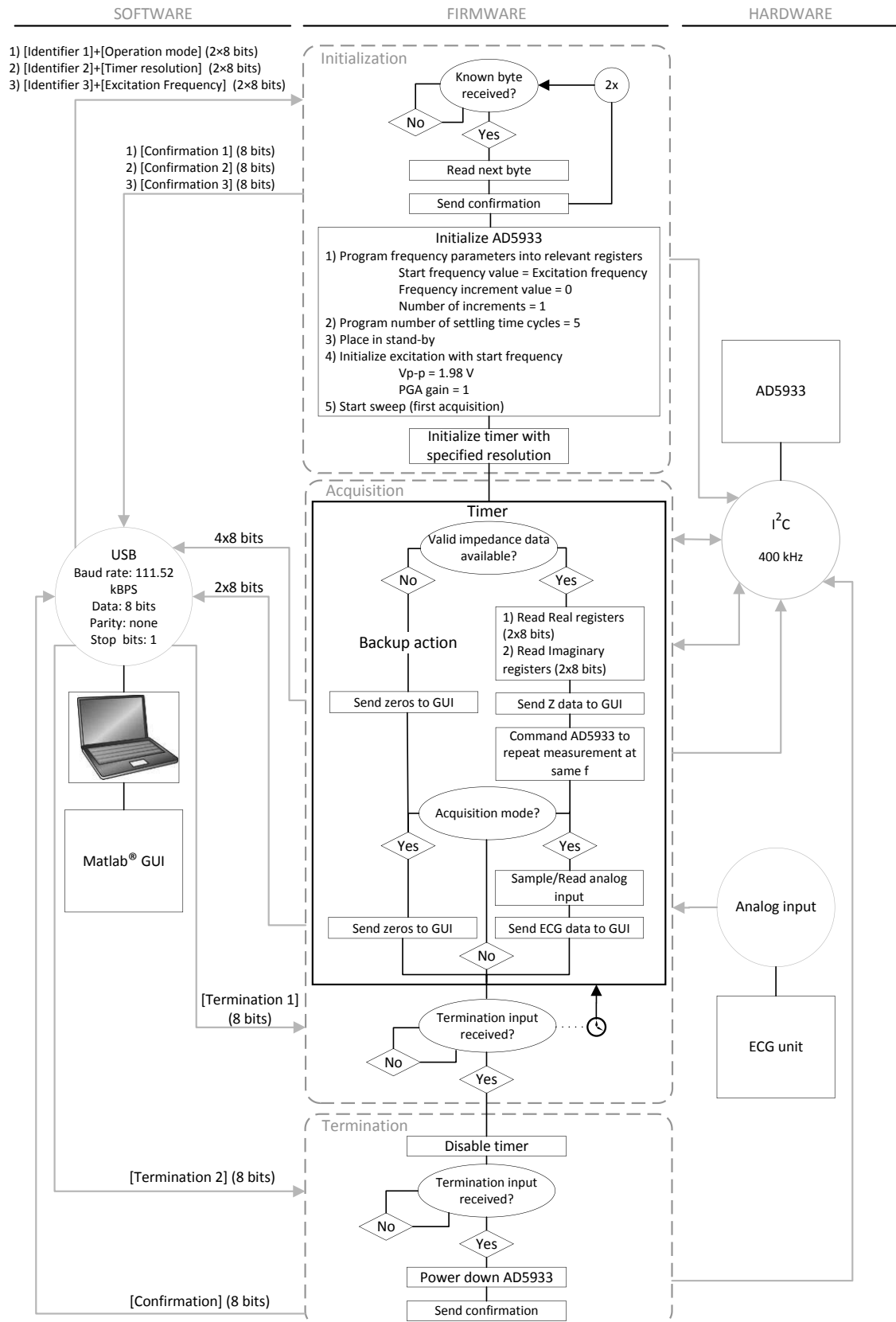


Figure 35) Process diagram for the firmware operation.

4.3. Software

The user guide interface (GUI) was developed using Matlab®. It allows the acquisition initialization, while giving control over some operation parameters, displays the raw results in real time and shows the pre-processed data at the end of each acquisition. In a similar way to the firmware, it can operate in one of two modes - ICG acquisition or calibration –, presenting some graphical differences in either cases. The operation mode is defined in a dedicated panel that also presents typical parameters for the chosen mode.

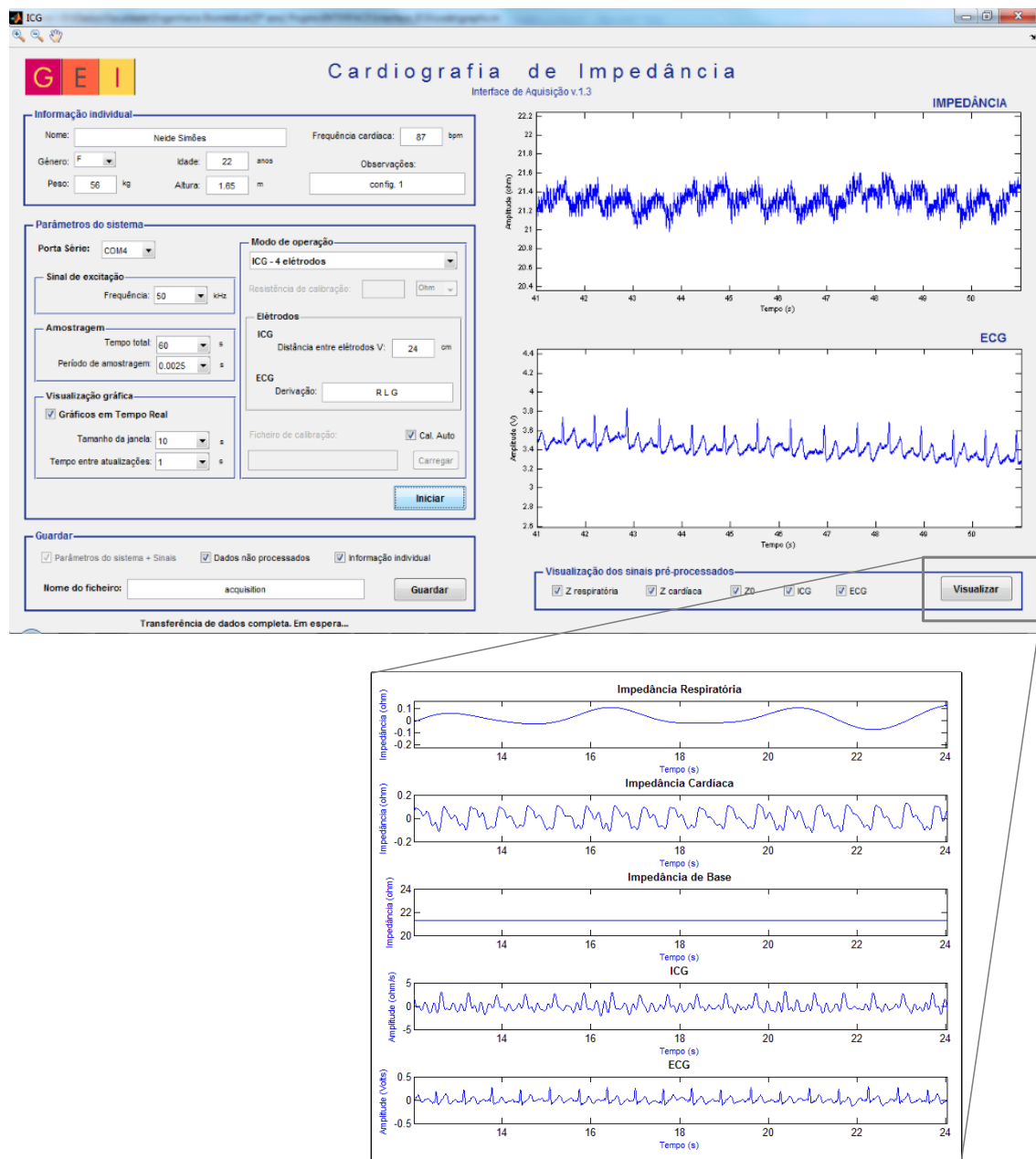


Figure 36) Graphic User Interface after a measurement presenting the raw impedance and the ECG signals and the pre-visualization of pre-processed data: respiratory impedance, cardiac impedance, base impedance, ICG signal and ECG.

During ICG acquisition the GUI exhibits a control panel (figure 36 , left side) divided into 3 sections. The subject information section enables gathering basic information about the examined subject: in hospital setting other parameters would be relevant, but for the depth of the studies conducted this was enough. The system parameters section lets the user choose the serial port (COM) where the Arduino® board communication is established, the excitation frequency, the sampling specifications and the graphical presentation parameters. The time between updates defines how often Matlab® revisits the information in the serial interface, the limit is 1 s to prevent data from accumulate rendering the Matlab® operation slow. A cancel button is available during acquisition, giving the option to stop the acquisition, while the acquired data can still be saved if the user wishes to do so.

When the acquisition process is initiated, after the initialization parameters are transferred, the data received at the serial port is converted to decimal values, then the raw amplitude and phase are calculated and calibrated. The calibration of the impedance data is implemented using a single pair of calibration parameters through the whole process. The calibration parameters can be obtained from a file generated on calibration mode that must be chosen by the user or by using an automatic procedure, in which case the first 10 s of data received are evaluated to verify the average raw amplitude value, used to calculate the calibration parameters based on established calibration models (section 5.3). This process and the initialization together account for an unreasonable waiting time that could not be reduced effectively.

The calibrated impedance amplitude with no further processing and the calibrated ECG are presented in the graphic panel (figure 36 , right side) and updated periodically. The remaining impedance curves (phase, resistance and reactance) are also calculated in background. At the end of the acquisition the data can be saved in a .mat file.

The pre-processed data can only be evaluated at the end of each measurement since the filtering is not applied in real time (section 6.1.3).

In calibration mode the interface presents a simplified control panel (figure 37). After the data acquisition is initiated the data received is converted to decimal and the raw amplitude (equation 13) and phase (equation 14) are presented in the graphic panel. At the end of each acquisition the calibration parameters are calculated based on the average values of amplitude and phase. Such data can be stored in a calibration file prepared to be used during acquisition.

Chapter 4: Impedance Cardiography Acquisition System

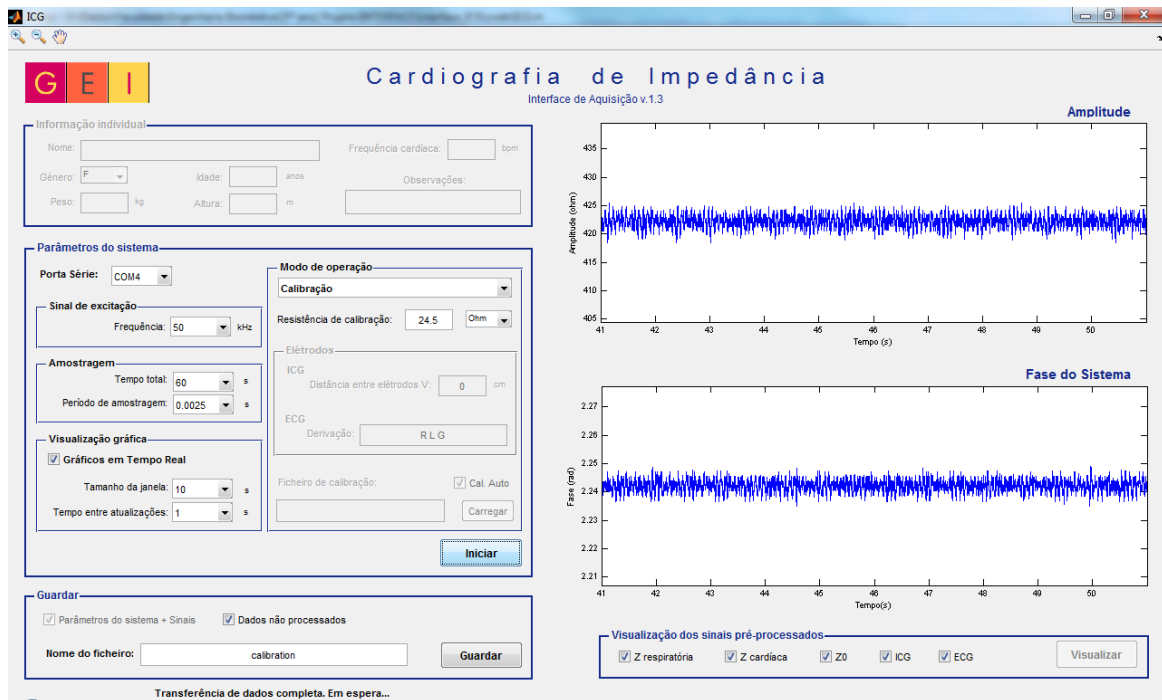


Figure 37) Graphic interface after acquisition of calibration data.

Chapter 5

System Evaluation

In this chapter the results from the system (described before) performance evaluation are presented.

The current source was tested in its native state to verify its compliance and internal resistance in order to corroborate the assumptions made in the last chapter related to its operation.

The AC and DC currents on board are examined to verify their accordance to the secure limits and the instrumentation amplifier measurement behavior is analyzed.

The practical implementation of the calibration procedure and the errors it introduces were studied. The calibration models established from this study as well as the resulting automated calibration procedure are also evaluated.

The process of estimation of the time delay introduced on the ECG signal by the filtering processes is also presented.

Contents

5.1.	Current source evaluation.....	62
5.2.	AC and DC performance and security limits.....	66
5.3.	Calibration procedure evaluation	69
5.4.	ECG time delay	75

5.1. Current source evaluation

In an ideal situation the system should be able to cope with body impedances till 1.5 k Ω [77], taking into account the sum of stray impedances in the current path. Also, the current source compliance has a fundamental role in the system correct operation, since the impedance load may present variations during the measurement procedure and between subjects. This way the maintenance of the current value across a comfortable range of impedance loads is necessary.

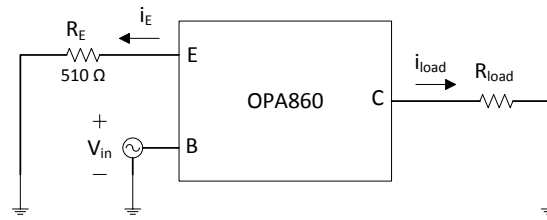


Figure 38) Voltage controlled current source (OPA860) basic configuration. B represents the base where an AC voltage is injected, E is the emitter where the current output is defined by the resistor R_E and C is the collector where the current output is delivered to the load resistor (R_{load}).

The VCCS compliance and internal resistance were evaluated at each working frequency of the ICG system for a set of load resistors (table 10) placed on the collector. The configuration employed is described on figure 38 and the tests were performed on bread board. The AC voltage on B was supplied by a signal generator and the average characteristics of the signal are described on table 11.

Table 10) Test resistor (R_{load}) values for evaluation of the current source. The values cover all the working range of the current source.

$R_{load} (\Omega)$	10.2	50.8	99.4	149.4	196	388	466	508	685	815	1190	2390
---------------------	------	------	------	-------	-----	-----	-----	-----	-----	-----	------	------

For every test resistor and for each excitation frequency the characteristics - frequency, peak-to-peak voltage (V_{p-p}), DC offset (V_{DC}) - of the input voltage signal at B and output voltage signal at C were registered. The measurements were performed using the Picoscope® - PC oscilloscope - acquisition interface.

Table 11) Signal generator output characteristics: frequency (F), peak-to-peak voltage (V_{p-p}) and DC offset (V_{DC}). Average values on the input B from each the measurement performed on the test resistors. The error is evaluated in terms of the standard error of the mean.

F (kHz)	V_{p-p} (V)	V_{DC} (mV)
50.20 ± 0.03	1.906 ± 0.002	79.41 ± 1.36
71.68 ± 1.03	1.913 ± 0.002	77.96 ± 4.60
103.38 ± 0.51	1.896 ± 0.004	79.74 ± 2.65

To evaluate the source compliance, the amplitude (i_{load}) and the DC bias (i_{loadDC}) of the current across R_{load} were calculated from the measured AC (V_{p-p}) and DC (V_{DC}) voltages at C as follows (equation 32 and equation 33). The results of such evaluation are presented below.

$$i_{load} = \frac{V_{p-p}}{2 \times R_{load}} \quad (32)$$

$$i_{loadDC} = \frac{V_{DC}}{R_{load}} \quad (33)$$

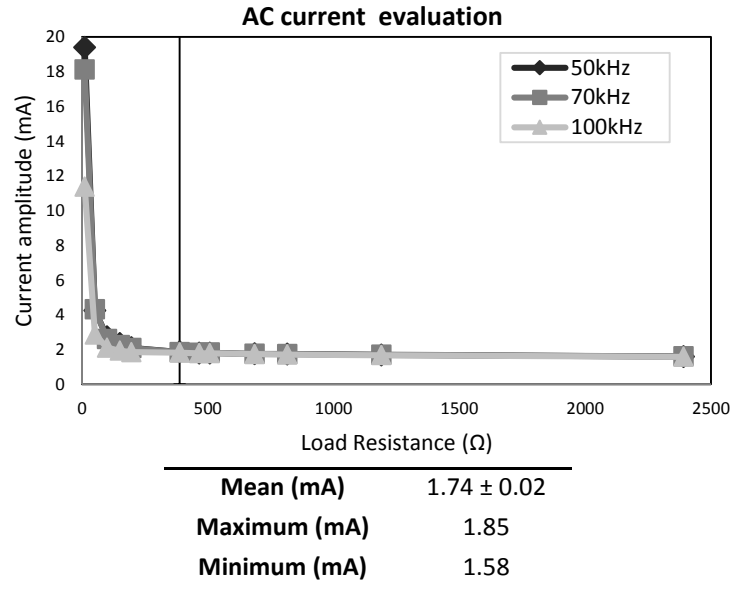


Figure 39) VCCS: current amplitude variation with the load resistance value. The vertical line represents $R_{load}=388 \Omega$. The statistic values consider only the stable region to the right of 388Ω .

The VCCS presents an acceptable AC compliance for load resistances higher than 388Ω (figure 39), with a near linear current response. Despite being different from the theoretical value, the current amplitude inside this stable region is in accordance to the ICG demands ($<2.5 \text{ mA}$, section 2.4.1).

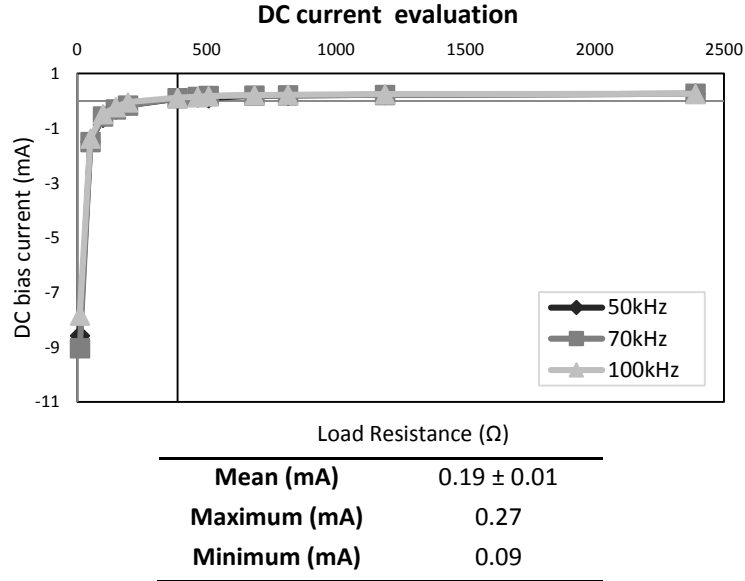


Figure 40) VCCS: DC bias variation with the load resistance value. The vertical line represents $R_{load}=388 \Omega$. The statistic values consider only the stable region to the right of 388Ω .

The DC response of the VCCS (figure 40) presents the same initial instable behavior as for the AC evaluation. For resistances higher than 388Ω , the DC current shows a linear behavior with the expected polarity for a positive DC input. The mean DC value is a conjoint result from the source input being dislocated from 0 V and the effect of the input bias current of the VCCS. These preliminary results are satisfactory though, because the DC output is inside the limits for human sensibility ($<0.6 \text{ mA}$, section 2.4.1).

The evaluation of the source internal resistance (R_{in}) was based on the expression for the current divider expression (equation 34), where i_{ideal} is the theoretical value of the current, obtained from R_E and V_{in} by applying the Ohm's law. Since the generator output value presented some variations the i_{ideal} value was calculated for each measurement, assuming R_E constant.

$$R_{in} = \frac{i_{load} \times R_{load}}{i_{ideal} - i_{load}} \quad (34)$$

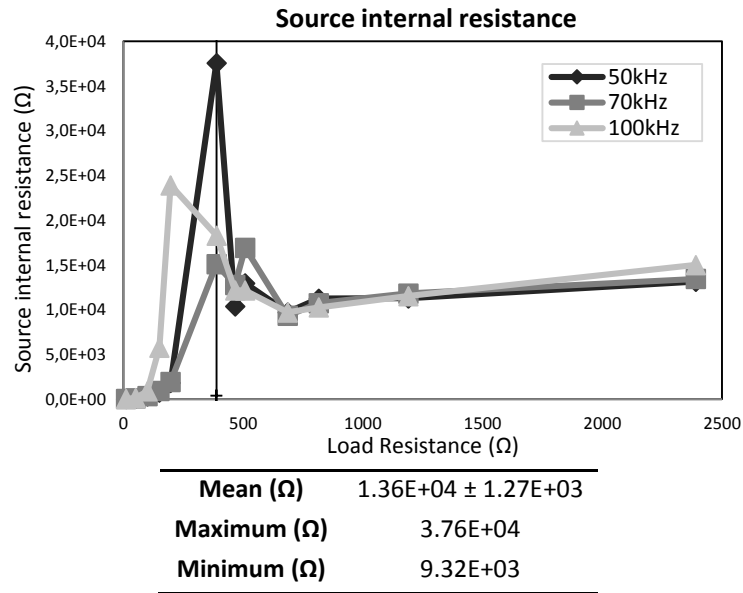


Figure 41) VCCS: internal resistance variation with the load resistance value. The vertical line represents $R_{load}=388 \Omega$. For $R_{load}<388 \Omega$ the internal resistance is presented in module (absolute value). The statistic values consider only the stable region to the right of 388Ω .

The mean source internal resistance (figure 41) inside the stability region is approximately one order of magnitude higher than the larger load resistance tested, which is an acceptable result.

For load resistances lower than 388Ω , the output current is higher than the ideal, rendering the denominator of equation 34 negative. The lowest the load resistor the better it approaches a short circuit and the less current is diverted through the source internal resistor, a behavior compatible with a high internal resistance. The current amplitude results (figure 39) are compatible with such line of thought presenting higher values of current through the load than for larger resistances. The accentuated decline of R_{in} for low R_{load} is an effect of the large absolute difference between the ideal and verified current on equation 34. Also should be notice that low R_{load} measurements suffered from higher noise levels which could have altered the results for those resistances.

From this evaluation follows that the VCCS load impedance can reach $2.39 \text{ k}\Omega$ without occur the output saturation due to the voltage generated across the load. Also, the output current deviation from the ideal is acceptable and the source can maintain the same approximate current values for a significant range of resistors, permitting an accurate function of the ICG system and a correct implementation of the calibration procedure.

To eliminate the devious behavior of the source for low resistors a grounded resistor of 390Ω was placed in the current path. This resistor is especially relevant when measuring impedances directly placed on the system terminals and permits the accurate implementation

of the calibration procedure (as described on section 4.1.2.2.2). When dealing with a real ICG acquisition the impedance of the two electrode-skin interfaces in the current path alone (section 2.5.2) are enough to put the source inside the stable region.

5.2. AC and DC performance and security limits

The system circuit was evaluated on board to verify if the current values across a load at its terminals were appropriated for human safety. The evaluation was performed on 17 resistors inside the operation range of the system (table 12), by placing them between the electrode plugs. The maximum resistor value was chosen by a trial and error process. The AC and DC voltages were measured using the Picoscope® interface and the current components were calculated as before, using equations 32 and 33.

Table 12) Test resistor (R_{load}) values. These resistors cover the full impedance measurement of the system.

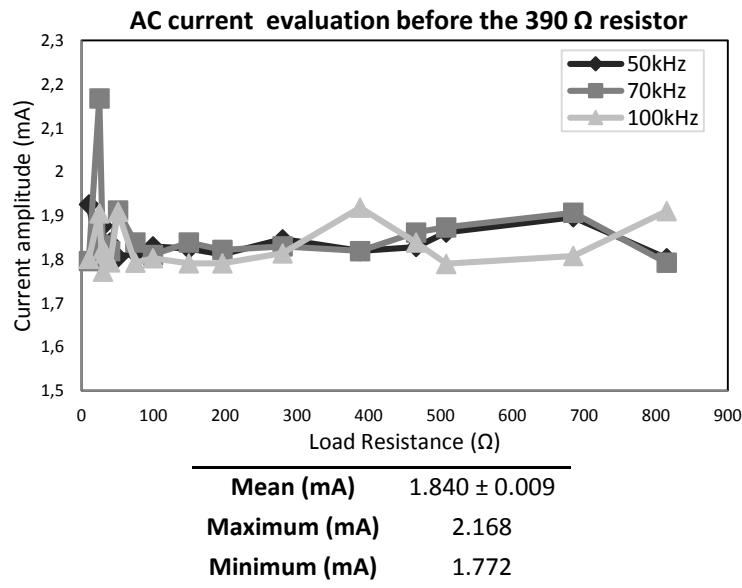
R_{load} (Ω)	10.2	24.8	29.8	30	33	39.7	50.8	74.7	99.4	149.4	196	280	388	466	508	685	815
----------------------------	------	------	------	----	----	------	------	------	------	-------	-----	-----	-----	-----	-----	-----	-----

The VCCS voltage input was also evaluated and the results are presented on table 13, showing acceptable accordance with the expected values and small variations.

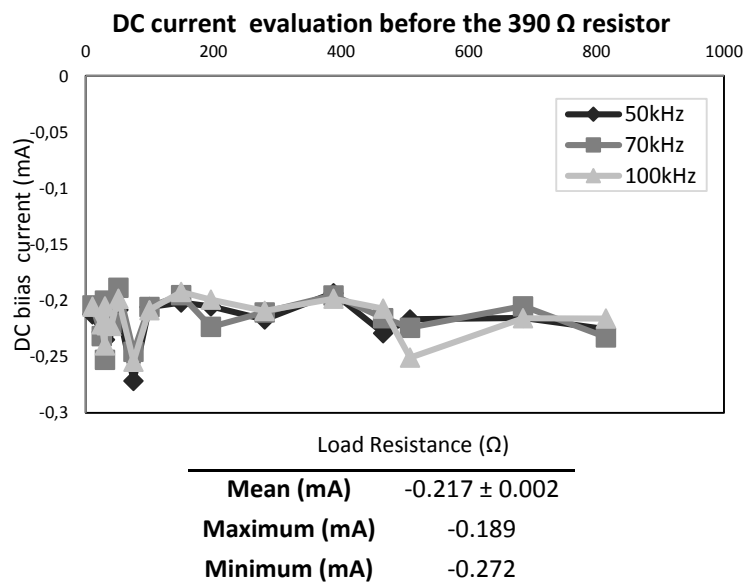
Table 13) VCCS voltage input characteristics on board: Frequency (F), peak-to-peak voltage (V_{p-p}) and DC offset (V_{DC}). Average values from each measurement performed on the test resistors. The error is evaluated in terms of the standard error of the mean.

F (kHz)	V_{p-p} (V)	V_{DC} (mV)
49.662 ± 0.003	1.951 ± 0.005	-95.47 ± 2.31
69.532 ± 0.002	1.942 ± 0.006	-89.41 ± 1.98
99.346 ± 0.007	1.929 ± 0.004	-90.20 ± 1.66

Since the total impedance value across the current path could only be estimated, the measurements were performed right before the grounded resistor of 390 Ω . This approximation considers that the current output after the DC blocking capacitor that will flow through the load, will also pass through the grounded resistor. Nevertheless, a remark as to be done related to the current that might be deviated through the stray capacitance parallel to the load (section 4.1.2.2.2). This effect will decrease the current through the load causing this study to be affected by a systematic error for excess regarding the current calculation. This does not affect the purpose of the actual study, since the excess error only extends the security limits for the current, in case the evaluated values are inside the security range.

Figure 42) PCB: current amplitude through the grounded resistor of 390 Ω .

All the registered current amplitudes (figure 42) are inside the range for ICG applications for this frequencies (<2.5 mA, as the most limitative value at 50 kHz, section 2.4.1). In average the variation is not significant, the overall variation registered may in fact be related to noise. The maximum peak registered was due to a noisy signal that altered the Picoscope® evaluation.

Figure 43) PCB: DC bias through the grounded resistor of 390 Ω .

The DC bias on board (figure 43) is negative since the input DC component is also negative, although the polarity is not very important for this matter. This evaluation shows that the AC-coupling does not completely removes the DC bias, although the results are below

the limits for human sensibility (<0.6 mA in module, section 2.4.1) in all the measurements, with a comfortable gap.

The current output after the blocking capacitor was also studied (Appendix D) based on an estimative of the total impedance load equal to the test resistance plus the grounded resistor value – also resulting in a systematic error for excess. The results were in average similar to the ones estimated based on the grounded resistor with no violation of the safety limits, producing an even larger gap from the safety limits. This data was not further studied since the first evaluation was considered more accurate.

The reference of 1.65 V fed to the AD8220 was adjusted at the beginning of each measurement to the closest value possible and the average of the values throughout the measurement process was 1.638 ± 0.002 V. The instability of this reference has especial influence in the AD5933 evaluation of the current input and after being verified its instability, it was corrected at each measured performed.

The calculation of the current from the instrumentation amplifier output was also attempted, although the results shown to be interesting, were unreliable for the current determination purposes.

Considering the AD8220 unitary gain definition, the current amplitude value passing through the load would be the result of applying the Ohm's law to the voltage output of the AD8220 (min = $0.144 V_{p-p}$ and max = $2.752 V_{p-p}$ in the range of resistors tested) and the load value in a similar way to equation 32. The result presented on figure 44 is not as linear as expected. This effect cannot be related to a current variation through the load as proven by the results of the current evaluation. The reason might be a non-linear behavior of the AD8220 for small loads at its terminals that is probably related to the combination of the noise effects on the small signals and also to the effect of the (small) input bias currents. This point is supported by the lack of information on its datasheet [80] for measurements below 100Ω .

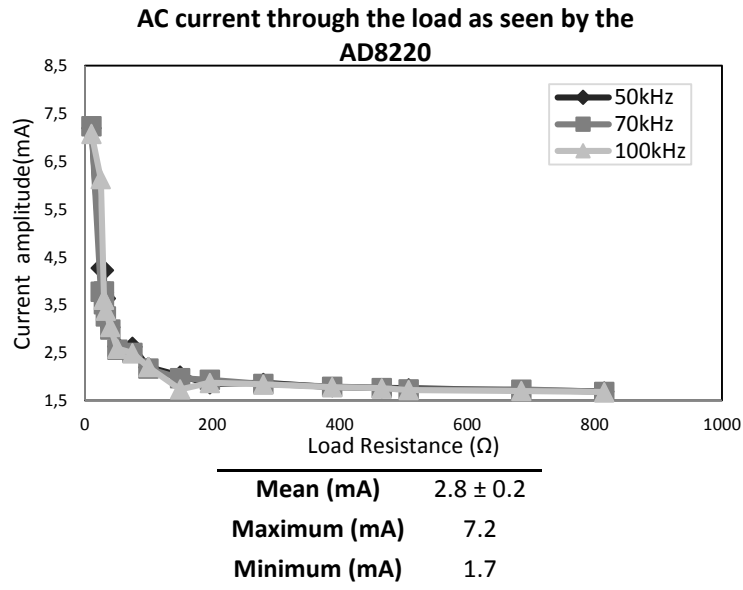


Figure 44) PCB: Current amplitude as a result of applying the Ohm's law to the AD8220 output voltage and the actual load resistor value.

The results from these evaluations were assumed to be kept when measuring the impedance on a real setup on a human. This is a good abstraction since the source shown a good maintenance of the current amplitude value and the circuit holds the capabilities to keep the DC component at low levels. Furthermore, the source output was later monitored during the system operation on a human subject at the minimum and maximum frequencies of interest to verify if the source would saturate or if any anomaly in the DC component would be verified. Since no anomalous result was verified the data was not further explored and the evaluations in this section were assumed as a good approximation.

5.3. Calibration procedure evaluation

In order to study the effectiveness of the proposed calibration procedure and attempt to reduce its limitations an exhaustive study of the effect of the excitation frequency and the R_{cal} value on the calibration parameters was made. The study resulted on the definition of models for the variation of calibration parameters that allowed the implementation of an automatic calibration procedure. The original calibration procedure used a pair of calibration parameters for each frequency based on the measurements on a single resistance. This was neither practical, nor reliable since it implied an approximation procedure for which the error could not be evaluated when dealing with a range of Z_{load} values. The evaluation was performed on the same resistors (table 12) that were used for the current limits analysis. To avoid a biased analysis of the results, two data acquisitions of 60 s, at a 400

Hz sampling frequency, were performed on each resistor: one for calibration and one for evaluation.

To evaluate the calibration process using a complex impedance a RRC circuit was developed, presenting amplitude and phase values fairly close to the thoracic impedance range (Appendix A).

Table 14) RRC circuit for testing purposes and impedance characteristics.

Frequency (kHz)	Amplitude (Ω)	Phase ($^{\circ}$)	Resistance (Ω)	Reactance (Ω)
50	23.451	-17.074	22.417	-6.886
70	21.805	-14.026	21.155	-5.284
100	20.766	-10.686	20.406	-3.851

The non-calibrated amplitude (equation 13) and phase (equation 14) with the quadrant correction – system phase - were calculated point-to-point using the calibration data set, and the results were averaged for each test resistor at each frequency. The gain factor for the amplitude (equation 25) was calculated based on the averaged non-calibrated amplitude.

The figure 45 shows a linear direct variation of the non-calibrated amplitude value - used to derive the gain factor - with the test resistor value. Exhibiting a behavior compatible with an admittance: the raw amplitude is an image of the current input of the AD5933 – initially inversely proportional to Z_{load} (section 4.1.2.1.1) – being directly proportional to the test resistance value (equation 27). The phase variation with the load resistance is not linear for small resistances and there is a clear variation of its value across frequencies.

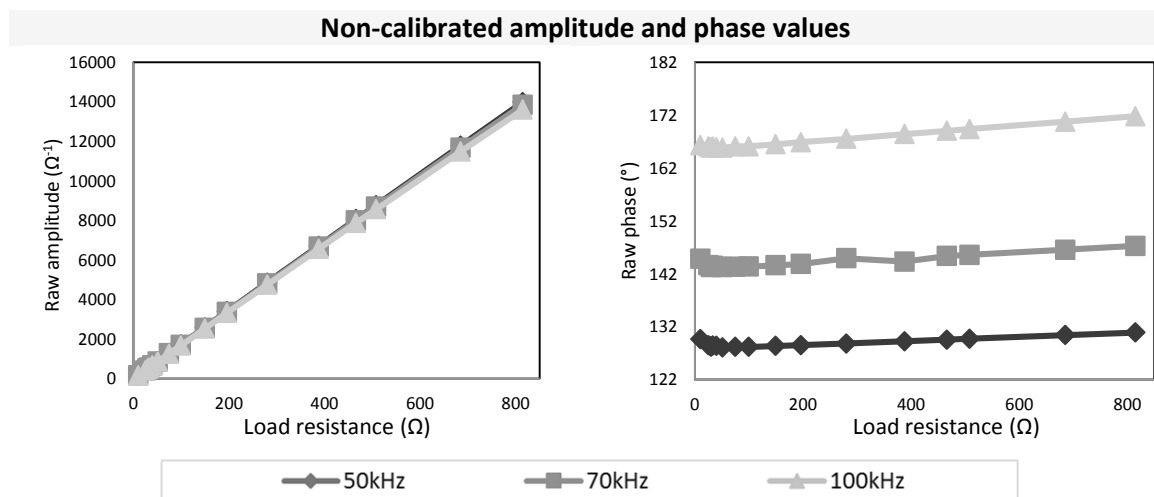


Figure 45) Variation of non-calibrated amplitude (left) and phase - system phase - (right) with the test resistor value.

The calibration parameters were evaluated first on the test data set from the same resistors and then on the RRC circuit, to evaluated univocally the effectiveness of the algorithm on complex impedances. The calibrated impedance amplitude (equation 27) and phase (equation 28) were calculated point-to-point and averaged for each resistance at each frequency. The amplitude error was obtained by comparing the calibrated amplitude to the test resistor (R_{cal}) nominal value. The residual phase was considered to be the phase error, since it was expected to be 0° .

The results on table 15 show that all the errors are lower than the unit. They might not reflect well the errors associated to the calibration process since the calibration parameters were applied to the calibration of the same resistor in which they were acquired. There was not a distinguished variation of the error with the test resistor or with the frequency.

Table 15) Absolute errors from the evaluation of the calibration parameters on test data from the same resistors: Average values from all the resistances at the same frequency.

Mean absolute errors		
Frequency (kHz)	Amplitude (Ω)	Phase ($^\circ$)
50	0.032	0.008
70	0.017	0.077
100	0.013	0.003
Maximum	0.032	0.077

The test with the RRC circuit (table 16) gives a better evaluation of the calibration performance for values near the range of interest for the ICG, especially important because its amplitude impedance is located in the non-linear region. The calibration parameters were obtained from a resistance of 24.8Ω . The errors indicated are relative to the expected values (table 14). The nominal values are also presented as reference. These results are proof that the algorithm can deal with complex impedances for which it was not programmed. The errors are higher than those evaluated for the test resistors but are still lower than the unit. No conclusions can be derived in what comes to the variation of the error with the frequency.

Table 16) Average impedance values measured on the RRC test circuit obtained with a calibration resistance of 24.8Ω and relative absolute errors (Δ).

Frequency (kHz)	Amplitude (Ω)		Phase ($^\circ$)		Resistance (Ω)		Reactance (Ω)	
	Mean	Δ	Mean	Δ	Mean	Δ	Mean	Δ
50	24.019	0.568	-16.689	0.385	23.007	0.590	-6.898	0.011
70	21.904	0.099	-13.904	0.122	21.262	0.107	-5.263	0.021
100	21.138	0.372	-10.856	0.171	20.760	0.355	-3.981	0.130
Maximum	-	0.568	-	0.385	-	0.590	-	0.130

The impracticability of the original calibration procedure is noticeable even in the evaluation of the errors introduced, since the calibration resistance has to be chosen in accordance to the expected impedance value which will introduce different errors in the measurement of the same impedance in accordance to the operator judgment. Testing all the combinations of R_{cal}/R_{RC} or R_{cal}/R was not made since it has little practical significance.

The original calibration procedure of the AD5933 relies on the R_{cal} nominal value (taken as amplitude rather than a real impedance component) to determine the calibration parameters and the non-calibrated amplitude returned by the system presents a direct relation to such value. This way the variation of the calibration parameters with the non-calibrated amplitude was studied, as the most relatable value to the load amplitude in general.

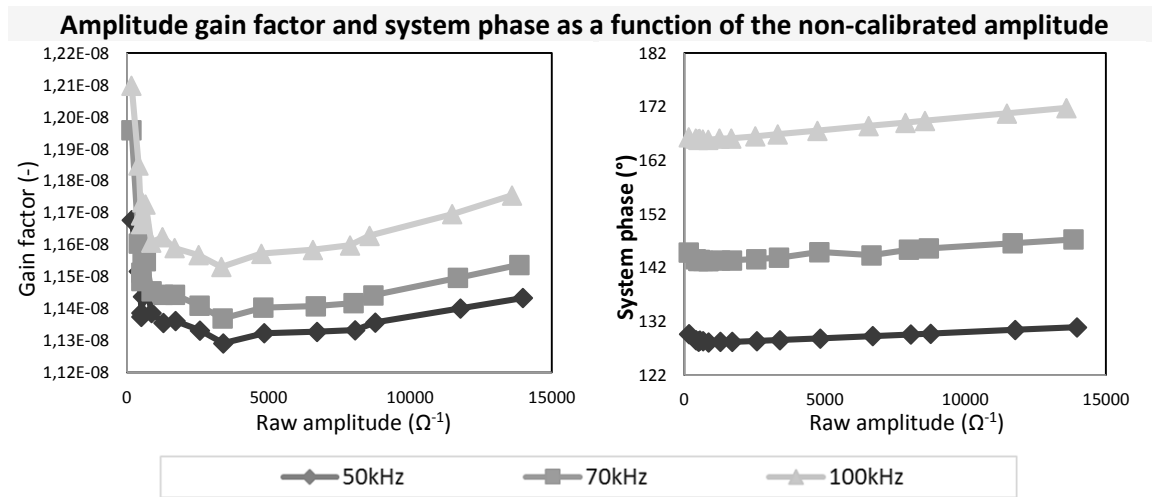


Figure 46) Variation of amplitude gain factor (left) and system phase (right) with the non-calibrated amplitude value.

The amplitude gain factor presents a non-linear variation with the raw amplitude value (figure 46). The non-linearity is particularly evident for low resistance values, showing a curvature similar to the one verified for the current across the load calculated from the AD8220 voltage output (figure 44), which is probably an important contribution to this observation. Nevertheless, the overall percent variation of the gain factor with the amplitude is small, presenting values of 3.41%, 5.18% and 4.92% at 50, 70 and 100 kHz, respectively. The system phase presents a relation to the raw amplitude value similar to that presented for the test resistance nominal value. The percentage variation of this value is 2.2%, 2.81%, and 3.58% at 50, 70 and 100 kHz. In both cases the correction parameters have a significant variation with frequency.

After these preliminary studies the calibration data was used to establish a mathematical model to estimate the calibration parameters based on the raw amplitude of the load, a descriptor of the load that can be directly accessed during the acquisitions providing information about its value. The mathematical tool Eureka [84] was employed to perform the data fitting and determine six mathematical expressions to describe each of the calibration parameters as a function of the raw amplitude (figure 46), at the three working frequencies (to confer the fitting plots refer to Appendix E).

The model was tested using data from the test resistors and the RRC. For each component tested the calibration parameters were deduced based on the average raw-amplitude of each acquisition on that component by applying the correspondent expressions.

Table 17) Absolute errors from the evaluation of the calibration model on the test resistors: average values from all the resistances at the same frequency.

Frequency (kHz)	Mean absolute errors	
	Amplitude (Ω)	Phase ($^{\circ}$)
50	0.225	0.041
70	0.176	0.054
100	0.166	0.070
Maximum	0.225	0.070

The mean absolute error (table 17) on the amplitude for the calibration procedure using the mathematical models is higher than before (table 15), but the phase error is lower. This data is very optimistic, but in relative terms can show a good performance of the calibration model, since both errors are still lower than the unit, not showing a significant variation over the first evaluation.

Table 18) Average impedance values from the RRC test circuit obtained from calibration parameters based on the calibration algorithm models and relative absolute errors (Δ).

Frequency (kHz)	Amplitude (Ω)		Phase ($^{\circ}$)		Resistance (Ω)		Reactance (Ω)	
	Mean	Δ	Mean	Δ	Mean	Δ	Mean	Δ
50	23.911	0.460	-16.654	0.420	22.908	0.491	-6.853	0.034
70	21.942	0.137	-13.827	0.199	21.306	0.151	-5.244	0.040
100	21.066	0.300	-11.028	0.342	20.677	0.271	-4.030	0.179
Maximum	-	0.460	-	0.420	-	0.491	-	0.179

For the RRC evaluation (table 18), the amplitude errors decreased and the phase error increased in comparison to the first evaluation (table 16), but all error values are below the unit, showing accordance between expected and calculated impedance values.

The evaluated errors although presenting small absolute values are still higher than the expected amplitude for the cardiac impedance signal (Appendix A). This is although a limitation of the technic that relies on a small amplitude signal to obtain its conclusions.

5.3.1. Automated calibration procedure

Based on these models was established an automated calibration procedure for the GUI (section 4.3), executed automatically at the beginning of each acquisition. Taking into account the final application of this system, a 10 s evaluation period was established in the beginning of each measurement to estimate the average raw amplitude used to calculate the calibration parameters for that measurement. The waiting time is not ideal, since it is too long for practical implementation, but is the minimum time necessary to account for the impedance variations due to the respiratory processes, that cause the most significant baseline variation of the thoracic impedance. It was estimated that during an acquisition the average raw amplitude based on the 10 s period represents the average value from the whole acquisition with an error of 2 %.

The effect of using a single pair of calibration values to correct a varying impedance as well as the variation introduced on the calibrated data by the 2% deviation on the raw amplitude were studied using true thoracic impedance data (Appendix F). The maximum discrepancy from the reference value - calibrated with parameters from the models using the raw amplitude value averaged from the whole set of data – introduced by such variables was an order of magnitude inferior to the maximum error value already established based on the RRC evaluation. This way such influences were considered to be of less relevance.

5.3.2. System measurement limits and errors

The upper measurement limit of the system was tested on board using several resistors connected to the electrode plugs to determine when the AD5933 would saturate and based on those values the range of test resistors (table 12) was defined. The measurement limit is defined by the AD5933 rather than the VCCS that did not show any sign of saturation during the evaluation on resistors, as verified from the tests in the section 5.2, neither for the evaluation on a real acquisition setup. Since the limit is defined for the resistors at the instrumentation amplifier terminals, the stray capacitances from the interface with the patient were not considered. In such case the interval would be narrower so that the VCCS output load would still be lower than 2.39 k Ω (section 5.1), although this does not have practical relevance since the thoracic impedance range is much below that limit.

The lower limit of measurement was defined by the lowest value tested and considering that the system was calibrated to deal with it. A remark as to be made towards this value since the SNR is not ideal at the AD8220 output for such small impedance.

Table 19) Summary of system capabilities.

Parameter	Range
Frequency	50 kHz, 70 kHz or 100 kHz
Impedance amplitude	10 to 865 Ω
Impedance phase	0 - 2π rad
Mean absolute amplitude error	0.46 Ω
Mean absolute phase error	0.42 $^\circ$

The summary of the system capabilities is presented on table 19. The errors specified are based on the highest known uncertainty: the one evaluated using the RRC circuit. Statistically this might not be correct, but the error evaluation for the maximum gives a better approximation to the overall error associated with the approximated calculations and the system limitations. The error analysis performed on measurements directly obtained from the system was based on those values ($\delta|Z|$ and $\delta\theta$). For the resistance and reactance an error propagation (equations 35 and 36) is considered, based on their calculation from the amplitude and phase (equations 29 and 30).

$$\delta R_{load} = \sqrt{(\cos\theta \times \delta|Z|)^2 + (|Z|\sin\theta \times \delta\theta)^2} \quad (35)$$

$$\delta X_{load} = \sqrt{(\sin\theta \times \delta|Z|)^2 + (|Z|\cos\theta \times \delta\theta)^2} \quad (36)$$

5.4. ECG time delay

Analog filtering introduces delays on the signal output. Since the ECG and ICG measurements need to be synchronized, the time delay introduced on the ECG signal by the filtering components on the circuit was studied in order to correct it. In this evaluation the system was considered linear phase, i.e. the filter introduces a constant delay for all the signal frequencies and no frequency distortion. This is not true and is easily verified from the ECG signal augmented waves, but is still a good approximation once the objective is only to dislocate the wave in terms of an absolute time delay and not correct any frequency non-linearity otherwise introduced by the commercial system.

The filtering components on figure 47, between the test points, are considered to introduce delay, since they are directly in the signal path (to assess the complete circuit schematic please refer to Appendix C). The amplifier delay was not studied under the

assumption that its contribution would not be relevant in comparison with the other components.

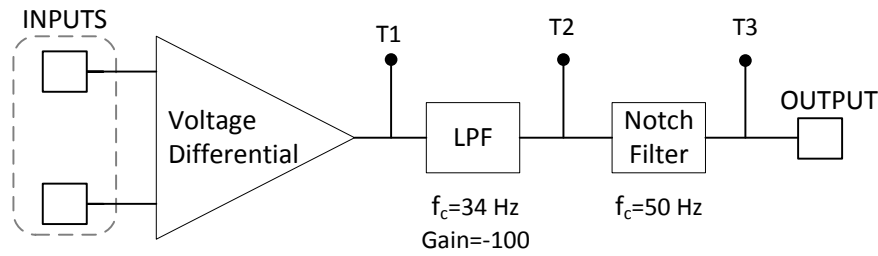


Figure 47) ECG front-end block diagram [82]: only components that are considered to introduce delay are identified. The delay evaluation was made in the identified test points.

The output of the first differential stage (T1) shown to be too noisy and flat to allow its comparison to the front-end output (T3), for that reason the delay was roughly estimated in a two-step process. The active low pass filter (T1-T2) was simulated with the Orcad® circuit simulation tool. The input to the low pass filter was a sinusoid with amplitude of 0.01 V and frequency 1 Hz, very close to the heart rate and, in short, the lowest frequency of interest (figure 48). The result of this evaluation was a delay of 4.53 ms, based on the difference between the zero crossing points of the input and output waves.

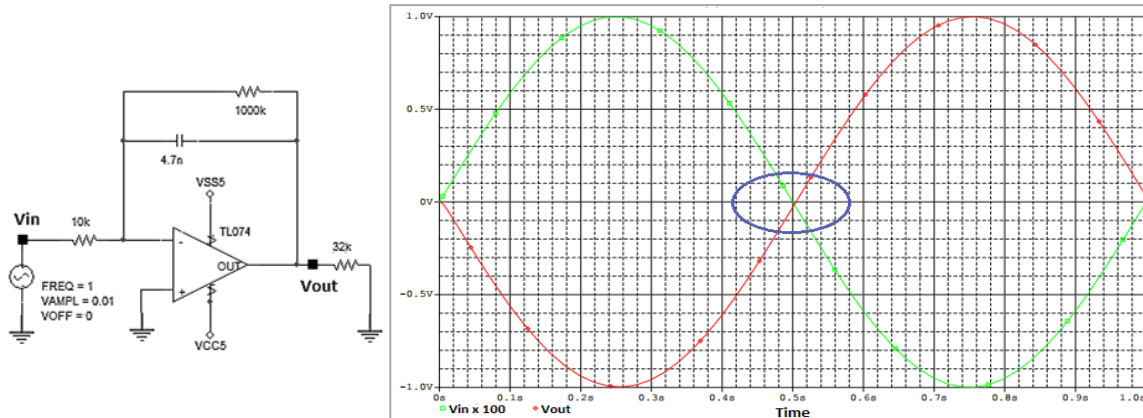


Figure 48) Low pass filter circuit simulated using Orcad® (left) and graphical representation of the input and output voltage over 1 s (right). The blue circle indicates the zero crossings where the delay was evaluated.

The notch filter input was perceptible (T2), allowing its direct comparison with the ECG front-end output (T3) in order to access the delay. The signals were simultaneously acquired at the notch filter input and at the front-end output with the Picoscope® interface (figure 49). The cross correlation of those signals was performed over 5 acquisition samples with 5 seconds each, using Matlab®. The result was an average delay of 5.50 ms with a standard error of the mean of 0.17 ms. The delay variation between data samples, reflects the non-linear frequency response of the filter for a variable signal, still the variation is not

significant when compared to the overall value, being contained in the minimum sampling period (2.5 ms).

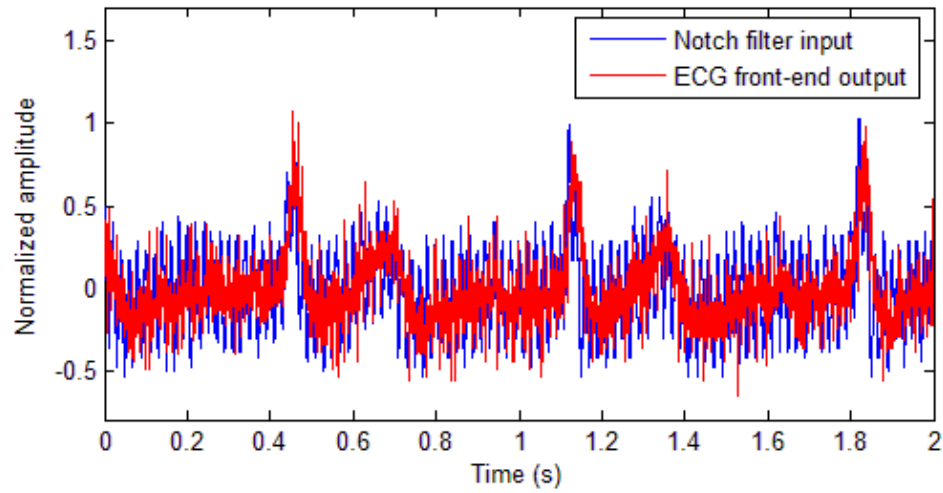


Figure 49) Normalized notch filter input signal and ECG front-end output. The lack of synchronization between the ECG peaks in both signal is visible despite the noise (related to the antenna effect from the direct measurement).

Considering only the circuit parts studied, the overall delay introduced is 10.03 ms. The ICG and ECG were synchronized, at the end of each acquisition, by software taking into account this value.

Chapter 6

Validation Tests

The ultimate goal of the developed ICG system is to acquire the thoracic impedance and ECG signals simultaneously on a human subject in order to assess the possible hemodynamic parameters. To verify the system performance on actual ICG measurements a pilot study was conducted on a small number of volunteers.

The acquisition procedure, the signal analysis – pre-processing, ECG-QRS detection, ensemble averaging and feature extraction - and the results related to relevant physiological parameters are presented and discussed in the following chapter.

Contents

6.1.	Methodology	80
6.2.	Results and discussion.....	87

6.1. Methodology

The ICG acquisition proceeding as well as the signal processing and analysis performed over the thoracic impedance and ECG signals in order to obtain the possible hemodynamic parameters are described over the next sections. At this point, should be clarified that no automated algorithms were developed in order to process the ICG signal.

6.1.1. Data Acquisition protocol

The data collection was performed on three healthy subjects (please report to table 21, page 88) with the objective of testing the effectiveness of the developed system. For every subject two variables were tested: the ICG electrode configuration and the excitation current frequency (50 kHz and 100 kHz). The objective of using two configurations is to find the most appropriated for this system in terms of practicality, SNR and general results.

The measurements were all performed with the subjects sitting upright for simplification of the acquisition set-up. The heart rate was measured with a cuff monitor and registered at the beginning of the acquisition procedure. Before the electrodes application, the skin was prepared with an ECG conductor spray.

The 3 lead ECG was performed simultaneously to the ICG and the electrodes where placed in accordance to the system specifications - right arm, left arm and the ground on the right leg, above the ankle (section 4.1.3).

Two ICG electrode configurations were tested: the first according to Qu et al. [28] – anteroposterior configuration described on section 2.5.1.1 - and the second as proposed by Penney et al. [85] – posterolateral configuration described on section 2.5.1.2. As a matter of uniformity, the positive leads (considering the VCCS output the high current lead) for ICG where placed above the negatives throughout the acquisitions, as suggested on the web page of the impedance cardiography system from Biopac® [31]. For each electrode configuration the distance between the sensing electrodes was measured with a metric tape. An initial test was performed to verify if the electrode placement was correct. During that time the subjects were asked to perform a stressed inspiration-apnea-expiration period to verify the right variation of the baseline impedance – a rise in the impedance magnitude during inspiration (figure 13). Two acquisitions of 60 seconds were then performed at a sampling rate of 400 Hz for an excitation frequency of 50 kHz and repeated for 100 kHz.

With different electrode configurations the distance between sensing electrodes could not be maintained. Since the electrodes are placed in accordance to physical markers

that vary from subject to subject, the distance between sensing electrodes for different subjects could not be maintained either, while using the same configuration.

The ECG electrodes had to be relocated after the first test so that the signal would not saturate. In all situations they were placed between the middle of the forearm and the middle of the arm. Due to this observation, ICG and ECG data was later separately collected using the same technics described above to verify the signals influence on each other.

6.1.2. Signal-to-noise ratio

The signal-to-noise ratio (SNR) of the impedance meter and ECG units was evaluated separately over calibrated non-filtered data from independent acquisitions, to eliminate any influence of the systems on each other. The SNR was calculated in accordance to equation 37.

$$SNR(dB) = 10 \times \log_{10} \left(\frac{Signal\ Power}{Noise\ Power} \right) \quad (37)$$

The ICG signal power was obtained from the squared RMS amplitude of the raw signal with length (N). The baseline was included in this calculation since it presents relevant information. The noise associated with this signal was obtained from the same signal by applying a stop-band filter to the signal frequencies, since it could not be directly obtained from the system because the instrumentation amplifier would saturate the AD5933 entry when no load was at its terminals, by moving the DC reference level to higher values.

$$Signal\ Power_{ICG} = \frac{\left(\sqrt{\sum_{i=1}^N Raw\ Impedance\ Signal^2(i)} \right)^2}{N} \quad (38)$$

Similarly, the ECG signal power was evaluated in accordance to equation 39 using the non-filtered signal and removing the baseline level. The noise component was obtained from a measurement with the electrodes disconnected from the subject.

$$Signal\ Power_{ECG} = \frac{\left(\sqrt{\sum_{i=1}^N (Raw\ ECG\ Signal(i) - DC\ level(i))^2} \right)^2}{N} \quad (39)$$

In both cases the noise power was evaluated in accordance to equation 40 by removing the baseline introduced by the system.

$$Noise\ Power = \frac{\left(\sqrt{\sum_{i=1}^N (Noise(i) - DC\ level(i))^2} \right)^2}{N} \quad (40)$$

6.1.3. Signal pre-processing

Several artifacts of physiological and non-physiological origin affect both thoracic impedance (section 2.7) and ECG signals. Either suffer interferences from patient movement (motion artifact, 0.1-10 Hz), respiration (baseline wander, 0.04-2 Hz), muscle contraction (electromyographic interference, 6-500 Hz [86]), bad coupling of the electrodes to the patient (contact noise), as well as the power-line interference with a characteristic frequency of 50 Hz and other electromagnetic interferences from the equipment [12]. The components of interest for the ICG analysis are between 0.8-20 Hz [50], the respiratory impedance relevant information is between 0.05-0.5Hz [54] and the ECG relevant information is commonly assumed to reside in the 0.5-40 Hz band [87].

The signal filtering applied in this case presents steeper frequency cuts in order to suit the actual system needs. This allowed the baseline stabilization and elimination of the spurious fluctuations at higher frequencies, without degrading the general shape of the signals. The calibrated and synchronized impedance and ECG signals were band-pass filtered in the frequency domain in the pass bands indicated on figure 50.

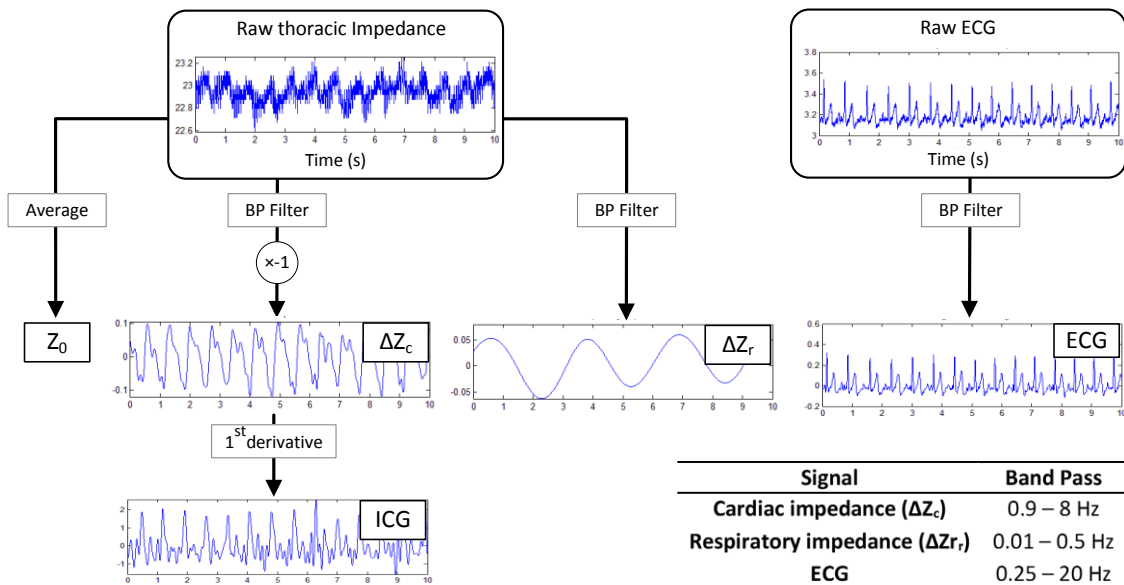


Figure 50) Pre-processing.

Commonly the thoracic impedance signal ($Z(t)$) is subtracted from the mean value (Z_0) and low pass filtered to remove higher frequency interferences, the first derivative (ICG) of such signal (ΔZ) relies on the ensemble averaging of the signal or other filtering technic to eliminate the respiratory component [50]. In the present case, the noisy thoracic impedance signal was directly filtered around the cardiac frequency using a strong band-pass filter,

directly eliminating the most relevant interferences, and only after that the first derivative of the inverted signal was performed to avoid noise amplification.

The ICG was calculated based on both the impedance amplitude and the real components in order to overcome the lack of information about which of the impedance components is studied. The base impedance (Z_0) was obtained from the mean value of each of those impedance components. The other thoracic impedance components - phase and reactance - show no relevance for the ICG analysis related to the cardiac activity, this way they were only evaluated in terms of their average values to verify their accordance to the information in the literature and even though they were filtered alongside with the amplitude and resistance no further analysis was conducted for the lack of reference values to be compared with.

The component related to the respiratory impedance was also separated from the original thoracic impedance signal to verify the variation of its influence with the electrode configuration.

The offline pre-processing procedure implemented in the software interface (section 4.3) includes the basic filtering described for the thoracic impedance components and the ECG, and goes as far as the ICG calculation, implementing all the steps on figure 50.

6.1.4. QRS detection

The automatic detection of the QRS complex on the ECG signal is an important step in the current system. The ICG signal correct processing relies on a good detection performance of the R wave.

The QRS detection algorithm employed was based on the traditional Pan and Tompkins algorithm [88], presenting a simple solution and yet a good performance [89]. The algorithm consists on applying several filters to the ECG signal in the time domain in order to obtain a square wave for each QRS complex, evaluated in respect to a threshold to perform the peak detection. The fundamental modifications to the original algorithm are related to the initial band-pass filter in the frequency domain instead of the finite impulse response filter applied in the time domain; the repeated squaring of the signal (raised to 4) instead of a simple squaring, in order to better differentiate the R wave from the T wave, that would sometimes show an amplitude near the first; and the simplified peak detection based on the relation to a non-adaptive threshold.

The squared wave is compared to the threshold - a fraction of the maximum ECG amplitude – identifying the relevant peaks. The R point is the maximum of the original signal inside each relevant segment identified, the Q point is the minimum before that maximum and the S point is the minimum after the maximum.

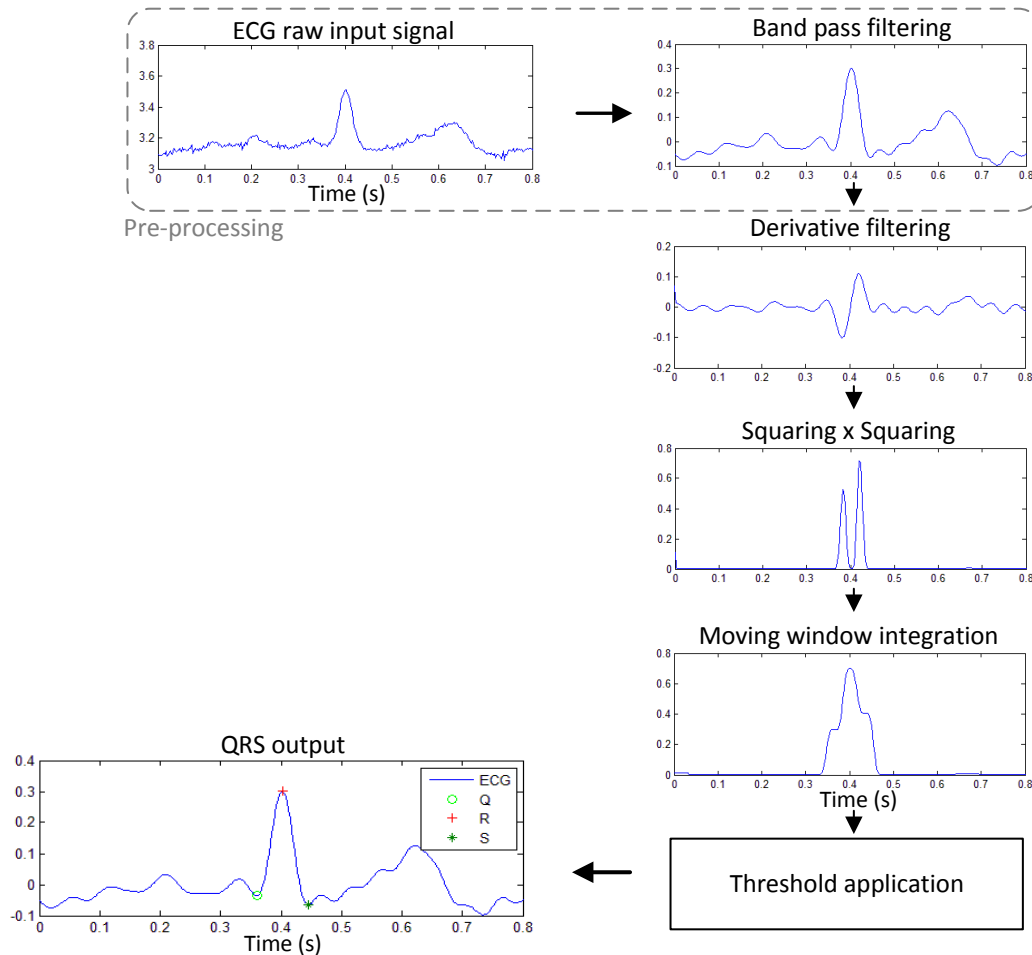


Figure 51) QRS detection algorithm steps (based on the Pan and Tompkins algorithm). Band-pass filtering: removes interferences; Derivative filtering: enhances peaks; SquaringxSquaring: turns the signal positive and reinforces the peaks in a non-linear way; Moving window integration: merges nearby peaks.

The average specificity and sensitivity of the algorithm for each characteristic point was determined by analyzing the results on three signals acquired on different subjects with the current system with simultaneous ICG acquisition – worst case. The evaluation was performed in accordance to equations 41 and 42, considering that: true positive is a correctly detected point; false positive is a falsely detected beat; false negative is an undetected beat and true negative corresponds to the points well detected different from the one being evaluated. This showed an acceptable performance for the R wave (table 20).

Table 20) QRS detection algorithm's performance.

Feature	# beats	Sensitivity (%)	Specificity (%)
Q	242	89	91
R		99	93
S		92	92

$$\text{Specificity} = \frac{\text{True Positives}}{\text{True Positives} + \text{False Negatives}} \quad (41)$$

$$\text{Sensitivity} = \frac{\text{True Negatives}}{\text{True Negatives} + \text{False Positives}} \quad (42)$$

6.1.5. Wave segmentation and Ensemble average

The ICG signal was segmented in order to perform its ensemble average over periodic repetitions, synchronized by the R peak from the ECG signal (figure 52). This process eliminates the beat-to-beat variability but reduces the effect of spurious components on the signal resulting on a final unique wave that can be analyzed to extract the relevant features. The ensemble averaging was performed over the minimum RR period by summing the digitized samples gated by the R wave and dividing the result by the number of beats (N) considered in the analyzed period [42]. The segmented beats were analyzed one-by-one, to exclude those that were badly segmented thanks to erroneous R peak identification, as well as the beats that presented affected ICG waves. The ΔZ and ECG waves were also averaged to be kept as a reference.

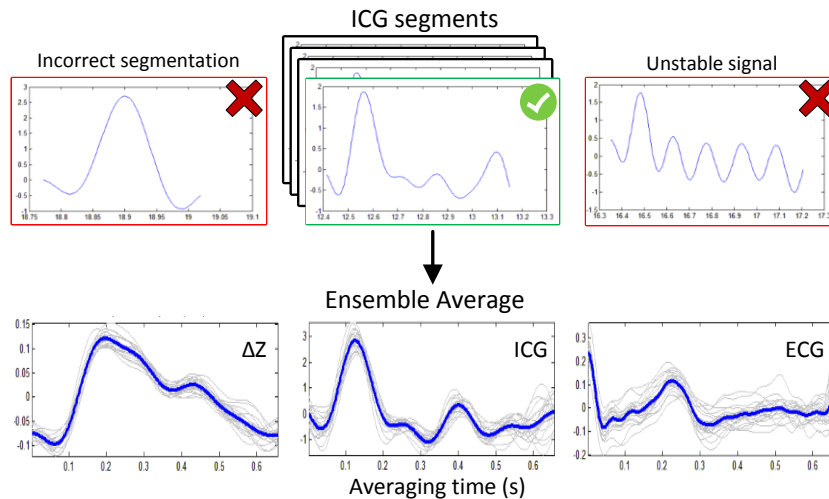


Figure 52) Ensemble average: ICG beats segmented by the R-ECG peak and averaged ΔZ , ICG and ECG signals over N beats.

At this point the base thoracic impedance (Z_0) was re-evaluated (Z_0'), taking into account only the thoracic impedance data correspondent to the accepted ICG segments.

6.1.6. Feature extraction

The signal quality did not allowed the identification of all the characteristic points on the ICG averaged curve, for that reason only the fundamental B, C and X points were studied. Those features were manually marked on a panel similar to the one presented on figure 53, using Matlab® tools.

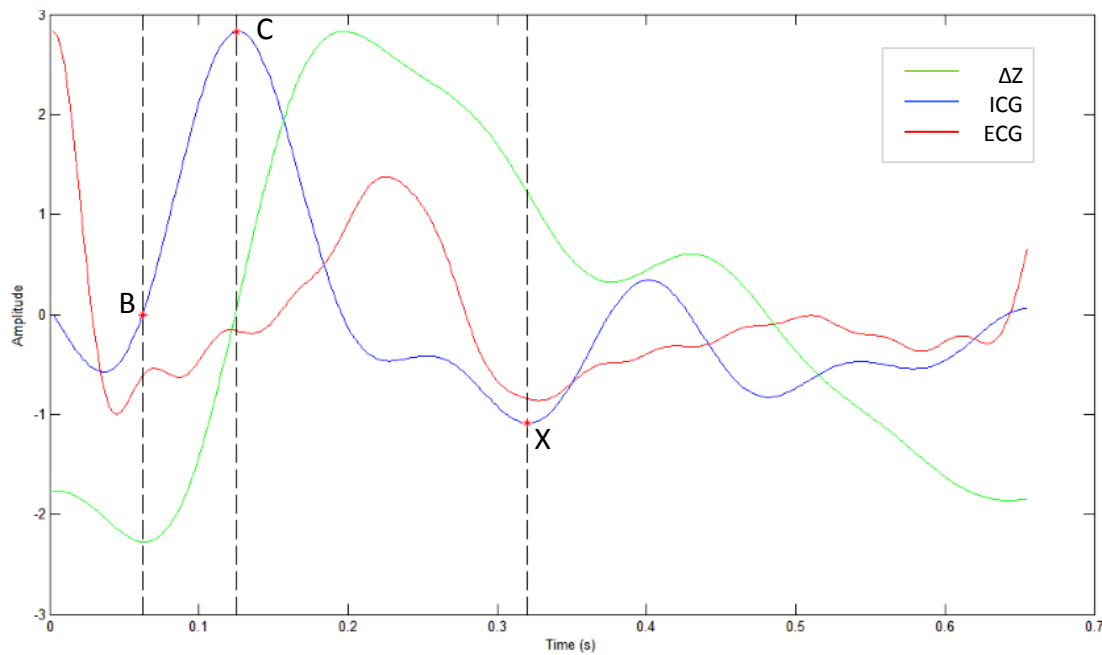


Figure 53) Feature extraction panel with relevant points on the ICG averaged signal. The ΔZ and ECG, normalized to the ICG maximum amplitude, were only used as references to correctly identify the characteristic points.

The highest ICG peak after the R wave from ECG was taken as the C point [90]. The B point was assumed to be at the zero-crossing point of the ICG curve prior to the point C [91]. This presented the most straightforward identification method, although some signals presented the inflection before C above zero and in those cases the minimum before C was considered as the B point [90]. The X point corresponds to the time instant where the lowest ICG value occurs during the negative section to the right of C (section 2.7.1).

6.1.7. Assessment of Hemodynamic Parameters

Based on the information extracted during the signal analysis the heart rate (HR), the systolic times (PEP and LVET) and the cardiac volumes (SV and CO) were obtained.

Relative to the assessment of relevant parameters from the signal analysis some explanations are required:

- The $(dz/dt)_{\max}$ is the maximal amplitude from the baseline to the peak of the ICG curve [4], corresponding to the C abscissa (figure 53).
- For the correct evaluation of PEP some authors consider the use of the Q-wave onset mandatory [92], others are that consider the Q peak a better solution [93]. In the present case the Q onset was used. To overcome the difficult Q onset identification was applied a method that seems to be current practice to estimate such value, by subtracting a fixed value of 48 ms from the time of the R wave peak. This method presents a relevant abstraction resulting on an estimation only [93, 92].
- The LVET being the time interval between B and X, was directly evaluated from the abscissa difference of those points.
- The HR was calculated from the average RR interval evaluated from the QRS detection algorithm output. The results had to be corrected by visual evaluation when the algorithm performed poorly.
- The SV was calculated from the Kubicek's formula, using a constant blood resistivity value. The value of 147 $\Omega \cdot \text{cm}$ was assumed for the purpose of this work, following the reference on the Biopac® cardiac output system's manual [94].

A resume from all the relevant parameters collected during the signal analysis and the uncertainties associated with such values, used in their evaluation process, is presented on Appendix G.

6.2. Results and discussion

The hemodynamic parameters vary with the position of the subject [37]. The standard position for ICG measurements is the supine, but several studies have been conducted while sitting or standing, showing a postural influence on the hemodynamic parameters obtained. The base thoracic impedance increases and the $(dz/dt)_{\max}$ value decreases from supine to sitting, resulting on a reduction of SV [95]. The time intervals are also affected as the heart rate increases with the body straightening [96]. Although, the absolute values reported from evaluations on different systems while sitting [97, 98] show, in comparison to the reference intervals for such values, higher SV, higher PEP and LVET inside the interval (Appendix B). The absolute values that could be assessed help to corroborate the values obtained from this system, since no direct comparison between the reference position and the sitting position was available.

During the acquisition procedure a crosstalk between the impedance and the ECG units was detected, that punctually led the ECG signal to saturation. For that reason, a posterior study was performed to compare the results from independent and simultaneous acquisitions of the two signals in order to establish a suitable error margin to the signal analysis. Following this, the results from thoracic impedance measurements alone will be first presented as a reference. The data obtained from simultaneous acquisitions of impedance and ECG on three subjects (table 21) and the physiological parameters determined by the subsequent signal analysis will then be presented and discussed under the light of the system's crosstalk influence.

Table 21) Subject data summary. The heart rate values presented are only indicative values, since they were not monitored throughout the long acquisition periods.

#	Gender (F/M)	Age (years)	Weight (kg)	Height (m)	Heart rate (bpm)
1	F	23	50	1.6	78
2	M	24	68	1.68	55
3	F	22	54	1.65	87

It should be stressed that the small population under study does not permit a relevant statistical analysis. Many factors can affect the impedance measurements which can lead to erroneous conclusions when analyzing such a limited amount of data, this way the results were only analyzed in average terms to verify the general accordance to the reference values in the literature.

The error analysis is made in accordance to the established on Appendix G, unless otherwise noticed. The comparison to reference values implies the values on Appendices A and B.

6.2.1. Signal-to-Noise Ratio

In accordance to the procedure described on section 6.1.2, the average SNR was evaluated using two sets of impedance and ECG data acquired independently from subject #3.

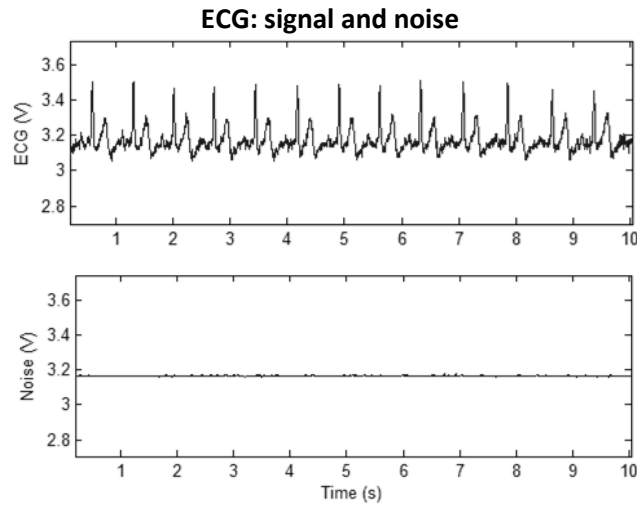


Figure 54) ECG signal without pre-processing and noise level obtained with the electrodes unplugged. The DC-level is not relevant in either case. The signal was acquired on subject #3 at a sampling frequency of 400 Hz.

The visual comparison of the ECG's signal and noise (figure 54) shows a relevant amplitude difference.

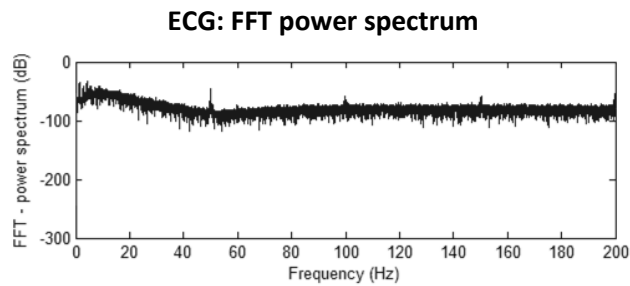


Figure 55) ECG signal's power spectrum in dB, after removing the irrelevant baseline.

The FFT (figure 55) shows a particularly noticeable peak at 50 Hz, relative to the power line noise. This indicates that the front-end notch filter is not very effective. The signal power at low frequencies, where the relevant ECG components are, is higher.

Table 22) ECG system's SNR. The presented value results from averaging the results of two acquisitions.

SNR (dB)
27.9

The ECG's SNR value (table 22) is general terms acceptable, permitting the noticeable distinction between signal and noise.

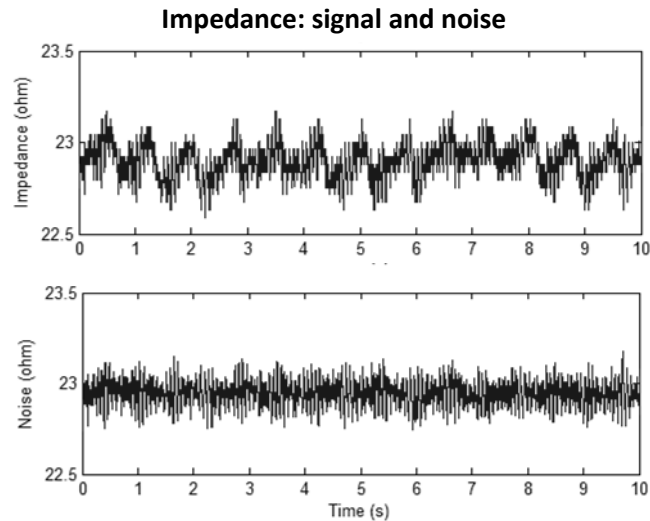


Figure 56) Impedance signal without pre-processing and noise level obtained by applying a stop-band filter to the signal frequencies. The DC level is relevant in the impedance case. The signal was acquired at a sampling frequency of 400 Hz, using the anteroposterior configuration, without the ECG parallel acquisition, while applying an excitatory AC current with a frequency of 50 kHz on subject #3.

The identified noise includes some physiological components not accounted in the process, for that reason it presents some periodicity similar to the cardiac impedance component. The amplitude relation between noise and signal is an intrinsic limitation from the ICG technic, which presents small varying amplitude when compared to the baseline value, resulting on similar amplitude of noise and signal, although with different frequencies.

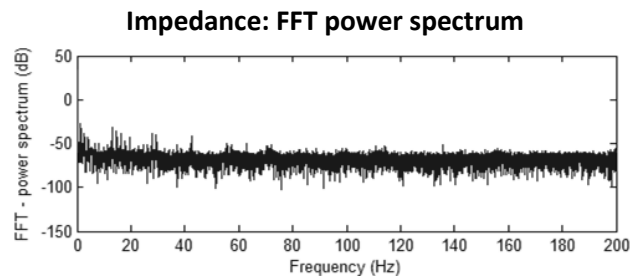


Figure 57) Impedance signal's power spectrum in dB.

The FFT (figure 57) shows noisy components throughout the spectrum, with an increased component around the origin, and the DC level correspondent to the baseline at 0 Hz.

Table 23) Impedance system's SNR. The presented values result in each case from averaging the values of two acquisitions.

Electrode configuration	F (kHz)	SNR (dB)	
		Specified	Mean
Anteroposterior	50	50.58	51.44
	100	51.73	
Posterolateral	50	51.73	52.45
	100	52.69	

The SNR value from the impedance system is higher at higher excitation frequencies and in average is higher for the posterolateral configuration. The SNR presents an acceptable value, since the mean value is a relevant part of the signal.

6.2.2. Thoracic impedance signal

The thoracic impedance signal components were evaluated in terms of their average values and the cardiac and respiratory components were explored in terms of their amplitude and resistance variation in order to verify its accordance to the reference values and verify which configuration would suffer less from the breathing modulation, respectively.

The impedance signals presented in this section were acquired on subject #3 following the same acquisition procedure on the methods section. Although extra acquisitions were performed with the ECG electrodes unplugged, after every simultaneous acquisition to maintain the same exact ICG electrode configuration and proportionate the reference thoracic impedance signal that is presented here.

Table 24) Thoracic impedance average (Z_0) values from the calibrated curves obtained from two acquisitions at each frequency.

Electrode configuration	F (kHz)	L (cm)	$ Z_0 $ (Ω)	Θ_0 ($^\circ$)	R_{20} (Ω)	X_{20} (Ω)
Anteroposterior	50	26 ± 1	22.90 ± 0.46	-6.04 ± 0.42	22.77 ± 0.46	-2.41 ± 0.17
	100		22.16 ± 0.46	-9.40 ± 0.42	21.86 ± 0.45	-3.62 ± 0.18
Average	-	-	22.53 ± 0.26	-7.72 ± 1.19	22.32 ± 0.32	-3.01 ± 0.43
Posterolateral	50	36 ± 1	27.33 ± 0.46	-5.04 ± 0.42	27.23 ± 0.46	-2.40 ± 0.20
	100		26.18 ± 0.46	-5.38 ± 0.42	26.06 ± 0.46	-2.46 ± 0.20
Average	-	-	26.76 ± 0.41	-5.21 ± 0.12	26.64 ± 0.41	-2.43 ± 0.02

According to the results on table 24, the average magnitude and resistance are always inside the reference interval (15-45 Ω). The absolute value of the averaged phase angle is below the expected values for the posterolateral configuration (6.4-10.92 $^\circ$), but fairly close.

The difference between the amplitude and real impedance components is also contained in the error interval, indicating that the use of one or another in the calculation will

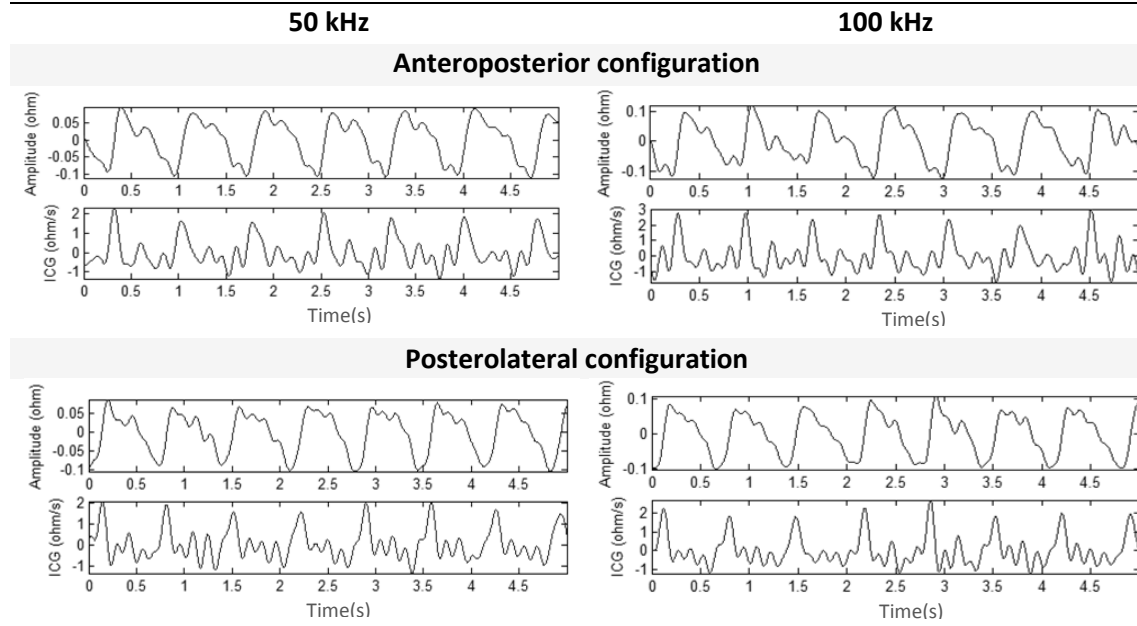
not show an important difference. The thoracic reactance compared to the resistance value is small (11%, and 9% for the anteroposterior and posterolateral configuration, respectively), and as foreseen can be ignored. Since the human body only presents capacitive components the reactance presents a negative signal.

As expected, the impedance amplitude and real component both decrease with the frequency of the excitation ac-current, presenting though a very small variation across frequencies, contained in the error interval. Although, the phase angle relative to the positive x-axis decreases, causing the absolute value of the imaginary component to increase, resulting on a higher absolute reactance at higher frequency. The added component in the imaginary part of the impedance is probably due to a leakage current that adds the impedance of the sensing electrodes to the impedance of the chest, which the calibration process could not avoid, introducing an unbalanced correction. The increased error in the reactive part of the impedance seems to be a common problem and is usually attributed to stray capacitances [20, 17].

Both configurations show in general similar results in the relevant parameters, with the posterolateral configuration presenting higher impedance amplitude related to the increased distance between the sensing electrodes.

The cardiac impedance signal, obtained from filtering the thoracic impedance amplitude and real component, and its first derivative were evaluated in terms of their peak values using an algorithm for peak-detection on Matlab®. The graphical presentation of the cardiac impedance signal (figure 58) based on amplitude and resistance presented no visual difference, for such reason and to avoid redundancy only the waves derived from the amplitude evaluation are shown.

Cardiac impedance component

Figure 58) Cardiac impedance de-noised signals: impedance (ΔZ_c) and ICG (dZ_c/dt).

The signals produced by the anteroposterior configuration seem more stable at 50 kHz. The opposite is verified for the posterolateral configuration, although in this case the impedance signal at both frequencies produced ICG signals with less fidelity. The ICG signals present in either cases, low resolution, with relatively distinctive B and Y notches, while the other points are almost unidentifiable thanks to several inflections around their expected location.

The literature suggests that the cardiac activity is better recognized at lower frequencies, [20], which in part relates to these results.

Table 25) Peak-to-peak values of the de-noised cardiac impedance component (ΔZ_c) obtained from the thoracic impedance curves. The uncertainties were estimated using the standard error of the mean.

Electrode configuration	F (kHz)	$\Delta Z_c (\Omega)$	$\Delta R_{Zc} (\Omega)$
Anteroposterior	50	0.20 ± 0.01	0.19 ± 0.01
	100	0.23 ± 0.02	0.23 ± 0.02
Average	-	0.21 ± 0.01	0.21 ± 0.01
% of the base value	-	0.95	0.95
Posterolateral	50	0.17 ± 0.01	0.17 ± 0.01
	100	0.19 ± 0.01	0.19 ± 0.01
Average	-	0.18 ± 0.01	0.18 ± 0.01
% of the base value	-	0.68	0.67

The variations in the base impedance related to the cardiac activity (table 25) are inside the range of accepted values (0.04-0.4 Ω , amplitude) for both configurations. The peak-to-peak values show in both cases an increase with frequency, although it is contained in the

error interval. The anteroposterior configuration presents more pronounced variations but the difference is not very significant.

It should be noticed that the absolute variations of the impedance components are smaller than the absolute error attributed to the system's measurement capability. This is a limitation intrinsic to the technic and one way to overcome this situation is by making several acquisitions and averaging the results. In the present case more than performing several acquisitions, performing them at different frequencies with different electrode configurations and verifying in general coherent results is enough to confer the reliability needed to this study.

Table 26) Maximum peak value of the first derivative of the cardiac impedance component (ICG). The uncertainties were estimated using the standard error of the mean.

Electrode configuration	F (kHz)	$(dZ/dt)_{\max}$ (Ω/s)	
		Z	R
Anteroposterior	50	1.96 ± 0.18	1.94 ± 0.18
	100	2.70 ± 0.16	2.62 ± 0.16
Average	-	2.33 ± 0.26	2.28 ± 0.24
Posterolateral	50	1.66 ± 0.22	1.65 ± 0.22
	100	2.15 ± 0.20	2.10 ± 0.20
Average	-	1.90 ± 0.17	1.88 ± 0.15

The maximum value of the first derivative of the cardiac impedance signals (table 26) is in average contained within the reference interval of normality (0.8-2.5 Ω/s). The expected effect of a narrow filtering band would be the decrease of the $(dz/dt)_{\max}$ value [51], which does not seem to happen since all the values are near the top of the reference interval. Also, the sitting posture would lead to the same observation. The contrary observation might be related to a real physiological particularity of the subject. There is a noticeable variation of $(dz/dt)_{\max}$, across frequencies showing increased values at 100 kHz and also across configurations with the anterolateral configuration presenting increased values.

The respiratory impedance signal, obtained from filtering the thoracic impedance amplitude and real component at lower frequencies, was also evaluated in terms of its peak values. Once more the amplitude is the only impedance component present since the signals present the same shape and overall magnitude.

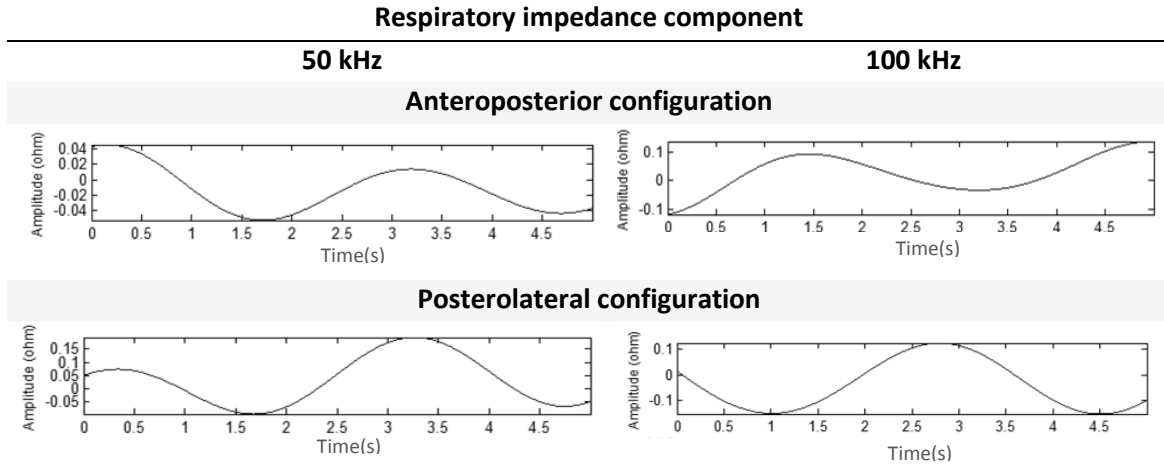


Figure 59) Respiratory impedance amplitude.

The resistance increases during inspiration [20], which was manifestly verified during the initial tests before the acquisitions (not presented), and shows a clean sinusoidal variation during the respiratory cycle.

Table 27) Peak-to-peak values of the de-noised respiratory impedance component (ΔZ_r) obtained from the thoracic impedance curves. The uncertainties were estimated using the standard error of the mean.

Electrode configuration	F (kHz)	$\Delta Z_r (\Omega)$	$\Delta R_{Z_r} (\Omega)$
Anteroposterior	50	0.08 ± 0.01	0.09 ± 0.01
	100	0.16 ± 0.04	0.17 ± 0.04
Average	-	0.12 ± 0.03	0.13 ± 0.03
% of the base value	-	0.54	0.58
Posterolateral	50	0.21 ± 0.02	0.22 ± 0.02
	100	0.25 ± 0.03	0.25 ± 0.03
Average	-	0.23 ± 0.01	0.23 ± 0.01
% of the base value	-	0.86	0.88

The respiratory component value (table 27) is far below from the expected values (0.675-2.025 Ω , amplitude), which only shows a weak influence of the respiratory signal on the signals recovered with the electrode configurations applied. The peak-to-peak value of the impedance is less than 1% of the base value and for the anteroposterior configuration this percentage is even lower than the cardiac component. The lower values are presented by the anteroposterior configuration at 50 kHz.

The posture is known to affect the amplitude of the respiratory signal [54], but this factor was not taken into account in the comparison. This way the conclusions established related to this component can vary while in supine.

From this analysis can be concluded that the values of interest for the ICG analysis present general accordance with the reference values. The signals returned by the anteroposterior configuration present better resolution for the ICG notches and seem to be more stable. Also this configuration is less affected by the respiratory modulation, which is easily justified by its sagittal electrode positioning.

The distinction between amplitude and resistance at this level does not seem to introduce great differences in the impedance values relevant to the ICG analysis.

6.2.2.1. ECG/ICG crosstalk influence

The crosstalk was first detected when the ECG signal would saturate and re-appear after the ECG electrode re-positioning, showing sometimes an increased noise level. Latter, it was noticed that the removal of the ECG ground would cause a noticeable variation of the impedance baseline, while none of the other electrodes would have any effect. This is justified by the flow of current through the path of less resistance to the ground: the impedance meter ground presents the electrode-skin interface plus the grounded resistance in the path, while the ECG ground only presents the electrode-skin interface.

Only the influence off the ECG on the impedance signal was studied, once the peak amplitude of the ECG signal is not relevant for the present study and the signal did not exhibit a noticeable distortion on the R peaks.

Since this problem lacks from a correction at the hardware level, is not relevant at this point to comparatively analyze the influence of the crosstalk on every detail of the impedance wave. This way, the relevant values for the cardiac evaluation - Z_0 , $(dz/dt)_{\max}$ – were compared in terms of their absolute difference in order to establish a suitable error margin for the results of the simultaneous acquisition based on the average difference of those values.

The posterolateral configuration was less affected in terms of the impedance baseline dislocation, but it suffered from a $(dz/dt)_{\max}$ alteration similar to the one verified on the other configuration. Also, the direction of the affectation was not equal for all the parameters on the two configurations. To simplify the error evaluation the mean absolute variation noticed is presented as the uncertainty value (table 28).

Table 28) Effect of the ECG/ICG crosstalk: mean absolute error and maximum error percentage introduced. The results were evaluated on the average of two acquisitions at each frequency for each configuration studied.

	$\Delta Z_0 (\Omega)$	$\Delta\theta_0 (^\circ)$	$\Delta R_{Z_0} (\Omega)$	$\Delta X_{Z_0} (\Omega)$	$\Delta(dZ/dt)_{\max} (\Omega/s)$	
					$ Z $	R
Mean abs.	1.38	1.88	1.43	0.66	0.44	0.43
Max. (%)	11.72	41.78	12.18	35.09	46.69	45.05

The original error introduced by the system was ignored in the following calculations since the effect of the crosstalk introduces a much higher uncertainty.

6.2.3. Impedance Cardiography signals and hemodynamic parameters

The comparative analysis of the averaged thoracic impedance components (Appendix H) did not show any relevant discrepancy in comparison with the analysis performed before, presenting the same inaccuracies. The only difference was the variation of phase and imaginary component with configuration, showing higher absolute values in the posterolateral configuration, reversing the first analysis. The comparative analysis between subjects was not conclusive since the variations are in most cases contained in the error interval.

The hemodynamic parameters were estimated at each frequency for each individual and for each configuration on two separated ensemble average processes, corresponding to two data acquisitions, and then the results were averaged. The ensemble average was sometimes performed on less than 20 beats for the same subject thanks to the low signal quality, which might affect the accuracy of the resultant averaged signal. The difference between the resistance and amplitude evaluations also has an inaccuracy introduced by the operator analysis since the resistance and amplitude curves were evaluated separately in what comes to the feature extraction. For such reason, even though the curves were similar and based on the same beats the characteristic points might have suffered small aleatory dislocations.

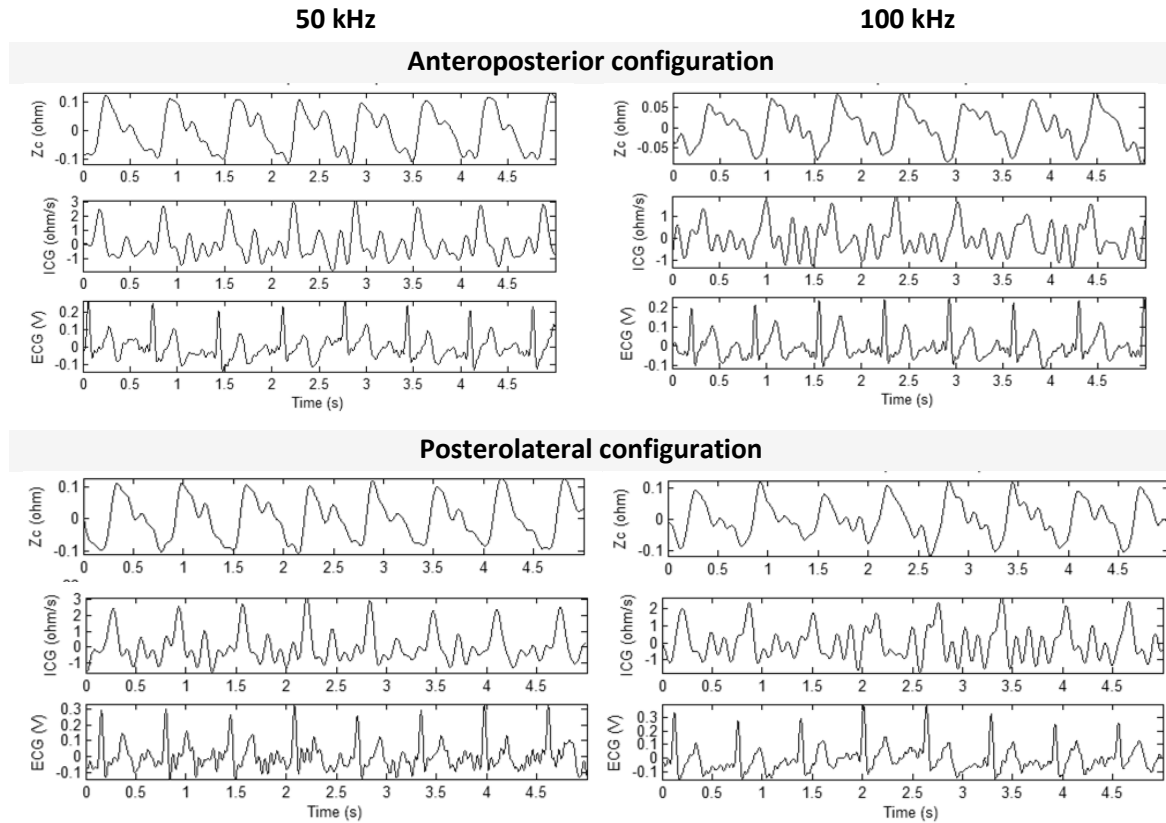


Figure 60) Impedance cardiography signals (cardiac impedance, ICG) and ECG. Results from both electrode configurations while applying an excitatory AC current with frequency of 50 and 100 kHz, respectively.

The impedance signals (figure 60) show increased instability at higher excitation frequencies, as noted before, producing a much distorted ICG wave. The posterolateral configuration presents signals with more distinctive features than those acquired on the same subject and without the ECG influence. It would be expected that the signal under the ECG influence would degrade, the fact that the contrary happens might indicate that the initial results probably have been originated from punctual influences. Anyway, this reflects less stability from this configuration. The averaged signals (graphically presented on Appendix I) showed in general more instability at 100 kHz.

In order to simplify the study, the results were averaged for the same electrode configuration, ignoring differences between subjects - not conclusive - and across excitation frequencies - although noticeable in the base values, should not affect the final hemodynamic parameters, introducing its most important effect in the signal stability, as already noticed.

Table 29) Average impedance values for the same electrode configuration, employed to calculate the hemodynamic parameters. The uncertainties are evaluated in terms of the standard error of the mean.

Electrode configuration	L (cm)	N beats	$Z_0' (\Omega)$		$(dz/dt)_{\max} (\Omega/s)$	
			Z	R	Z	R
Anterolateral	23 ± 1	218	17.94 ± 0.94	17.86 ± 0.94	1.75 ± 0.19	1.73 ± 0.19
Posterolateral	33 ± 1	192	27.21 ± 1.04	27.03 ± 1.03	1.74 ± 0.16	1.72 ± 0.16

The average values of thoracic impedance and $(dz/dt)_{\max}$ (table 29) are in accordance to the reference values (15-45 Ω and 0.8-2.5 Ω/s , respectively). The average base thoracic impedance is higher for the posterolateral configuration as expected from the increased distance between the electrodes, but the $(dz/dt)_{\max}$ is very close to those of the first configuration. Although the standard error of the mean shows accordance between the values, the uncertainties associated with the individual values of $(dz/dt)_{\max}$ correspond in average to 27% of the absolute value.

The difference between Z_0 and Z_0' was never higher than 0.5 %, which validates the procedure of considering only the base thoracic impedance of the averaged beats.

Table 30) Average hemodynamic parameters for the same electrode configuration. The uncertainties are evaluated in terms of the standard error of the mean.

Electrode configuration	HR (bpm)	PEP (s)		LVET (s)		SV (ml/beat)		CO (L/min)	
		Z	R	Z	R	Z	R	Z	R
Anterolateral	78.09 ± 3.06	0.11 ± 0.01	0.11 ± 0.01	0.29 ± 0.01	0.29 ± 0.01	124.00 ± 5.56	123.74 ± 5.51	9.70 ± 0.61	9.68 ± 0.61
Posterolateral	81.93 ± 3.45	0.11 ± 0.003	0.11 ± 0.003	0.27 ± 0.005	0.27 ± 0.005	100.09 ± 4.16	100.52 ± 4.03	8.24 ± 0.60	8.28 ± 0.59

The HR (table 30) is in accordance to the physiologically acceptable values (60-100 bpm). The individual variation from the initial direct HR measurement can be easily explained by assuming that during the long acquisition process this parameter naturally changed. The PEP value was sometimes higher than the reference values (0.05-0.12 s), but is always inside the interval of values while sitting (0.11-0.14 s), showing no variation with the electrode configuration. In average the value is acceptable. The LVET average value is inside the reference interval (0.25-0.35 s), as well as the individual values from each subject, presenting in average a lower value for the posterolateral configuration. The SV is above the reference values (60-100 mL), but is always inside the estimated interval for measurements while sitting (74.5-142.7 mL). The CO is also augmented in accordance to the reference (4-8 L/min), which is related to the SV value but also to the increased HR while sitting. The SV and CO values are closer to the expectable when using the posterolateral configuration.

The uncertainties presented on table 30, show acceptable accordance between the averaged values. Although, the individual values present much higher uncertainties (to assess

the specified values refer to Appendix H), with maximum error percentages of 67% for PEP, 32% for LVET, 45% for SV and 45% for CO.

The conclusions from this analysis can be resumed as follows:

- There are no relevant differences between values obtained from amplitude and resistance. This way the angle value is ignorable, and strange results in terms of the phase variation across frequencies are not relevant, especially since the ICG analysis is made at a single frequency.
- The influence of sitting is not very clear on the results, but the values seem to be in general accordance to those in the literature either for sitting or for the reference interval.
- The physiological variation of the studied parameters can justify some discrepancies between individual measurements. Nevertheless, for the same subject there are relevant and diverse alterations on the hemodynamic parameters across frequencies and also between configurations, which would not be naturally expected on healthy subjects.
- The most relevant point related to the excitation frequency is the wave form, that in general seems more stable and literature looked-alike for 50 kHz.
- The constant blood resistivity and the formula for obtaining the Q_{onset} for PEP turn these values into estimations that should not be used for accurate physiological evaluation purposes.
- For a question of signal fidelity and easier location of the electrode positioning spots the anteroposterior configuration seems the most appropriated.

This studies also shown that the system needs to be improved at the hardware level, especially because of the ECG and ICG influence on each other. The impedance SNR would benefit from an improvement, which would probably open other signal processing options, but the small amplitude of the ICG signals imposes an intrinsic limitation. Also, the de-noising process by applying a strong filtering is not the most correct and the narrow pass band around the heart rate might have uncovered some interesting features. The signal analysis and processing was a very consuming process that could only be carried out with a small study population, for larger populations it would be mandatory to develop automatized algorithms.

Both the lack of a reference process for the impedance measurement and for the physiological parameter calculation was limiting in terms of to the conclusions that could be assessed.

Chapter 7

Conclusions and Future Work

Contents

7.1.	General conclusions	102
7.2.	Future work	102

7.1. General conclusions

The work developed during this project managed to study the Impedance Cardiography in many of its facets.

The phantom set-up developed was more interesting for the purpose of understanding the impedance methods than to improve the present state of knowledge on the ICG area. The fact of being developed while the actual ICG system was not completely functional led to some improvisations that are not congruent with the actual ICG application.

The major goal of this project was to develop a functional system for ICG acquisitions. The prototype including hardware, firmware and software was built and tested on real ICG acquisitions on volunteers, showing overall acceptable performance of the impedance unit - capable of discerning small impedance fluctuations related to the cardiac activity -, but also the necessity to improve the ECG acquisition method at the hardware level. Furthermore, a simplified non-automated offline signal analysis cascade was applied to the recovered ICG and ECG signals in order to obtain parameters of physiological relevance. The results were in average inside the reference intervals, showing general accordance between measurements, despite several approximations and deficiencies spotted in the system's overall operation and the large percent errors associated with individual measurements. Though, the large uncertainties associated with the hemodynamic indicators, mostly related to the influence of the ECG on the impedance measurement, turns their use unreasonable to establish correct physiological correlations.

The developed prototype is although far from providing an accurate monitoring of the physiological data and caresses from improvements before the system can be of clinical utility but contributes with a good knowledge base to future works.

In general terms, the Impedance Cardiography proved to be an assessable method, but the accurate signal analysis seems to be an important challenge. Also, the limitation of the scientific basis in which the technic relies is an important weakness, but did not present any particular limitation to the developed work.

7.2. Future work

The correct and safe operation of the ICG acquisition system relies primarily on the hardware performance improvement.

Even though the system proved to perform well on the required impedance range, the need to develop a test circuit based on the stray impedances model remains. That would

allow performing the adjustment of the calibration procedure in the ICG range. This also relies on the need to obtain a reference method to establish the impedance measurement comparison.

The detected ECG/ICG crosstalk can be in part resolved by using an ECG circuit that does not grounds the patient - which proved to be the source of the ICG distortion -, connecting the right leg electrode to the output of an operational amplifier [99]. Also, such type of ECG system provides interference proof methods to improve the signal, relative to those that connect the subject ground to the ground of the system. The ICG system performance was superficially evaluated when acquiring the ECG with a third part developed system of such nature. The results showed no saturation of the ECG signal, only a slightly augmented noise level and the visual analysis of the impedance wave did not show any important alteration, although, this solution should be tested in more depth in relation to the ICG signal.

Other small improvements very specific to the developed system would include: the electrodes driven-shield; the use of high pass filters on the AD8220 entries to perform the AC-coupling of the residual bias-current, as shown in [71], which could improve the performance of the system with respect to the amplifier leakage current; improvement of the circuit that feeds 1.65 V to the instrumentation amplifier, to provide a stable reference, since the constant need to adjust its output would never be tolerated on a practical application. Also the AD5933 sensing resolution would probably benefit from an increased internal gain, causing the impedance measurement range of the system to decrease. These improvements could not be implemented during the time of the project for time constraints.

The signal analysis needs improved automated methods for signal processing, to eliminate possible affectations of the initial filtering and turn the remaining process more expeditious, in order to allow the beat-to-beat ICG analysis and the processing in real-time.

While performing measurements on a human being it is not possible to tell apart the regular variations due to physiological events, from the errors introduced by the measurement device. This way, the final validation of the physiological parameters returned from the system depends on the comparison with the results of simultaneous acquisition with other hemodynamic probes.

Bibliographic References

- [1] L. J. Vorvick, "Vital Signs", U.S. National Library of Medicine - National Institute of Health, 2013. [Online]. Available: <http://www.nlm.nih.gov/medlineplus/ency/article/002341.htm>. [Accessed 10 August 2013].
- [2] J. M. Van de Water, T. W. Miller, R. L. Vogel, B. E. Mount and M. L. Dalton, "Impedance Cardiography - The next vital sign technology?", *Chest*, vol. 123(6), pp. 2028-33, 2003.
- [3] C. J. Schuster and H. P. Schuster, "Application of impedance cardiography in critical care medicine.", *Resuscitation*, Vols. 11(3-4), pp. 255-74, 1984.
- [4] "Impedance Cardiography" in *Ambulatory impedance Cardiography – Systems and their applications*, Springer, 2011, pp. 7-33.
- [5] D. J. Wang and S. S. Gottlieb, "Impedance cardiography: more questions than answers.", *Curr Cardiol Rep*, vol. 8(3), pp. 180-6, 2006.
- [6] "How does the heart work?" [Online]. Available: <http://www.sorin.com/how-does-heart-work>. [Accessed 09 August 2013].
- [7] "Healthy and Living Women" [Online]. Available: http://www.livescript.com/health/a-z/conditions_a-z/conditions/a/aortic_coarctation.aspx. [Accessed 10 August 2013].
- [8] "Cardiac cycle," [Online]. Available: <http://goo.gl/02z70D>. [Accessed 09 August 2013].
- [9] D. Burkhoff, "Mechanical properties of heart and its interaction with vascular system.", *Cardiac physiology*, 2002.
- [10] T. C. Gillebert, J. De Sutter, N. Van De Veire and M. L. De Buyzere, "Time intervals and global cardiac function. Use and limitations.", *European Heart Journal*, vol. 25, pp. 2185-86, 2004.
- [11] M. Lavdaniti, "Invasive and non-invasive methods for cardiac output measurement.", *International Journal of Caring Sciences*, vol. 1(3), pp. 112-17, 2008.
- [12] J. D. Bronzino, *The biomedical Engineering Handbook Medical Devices and Systems*, 3rd ed., 2006.
- [13] J. Malmivuo and R. Plonsey, *Bioelectromagnetism - Principles and applications of bioelectric and biomagnetic fields*, Oxford University Press, 1995.
- [14] C. F. Babbs, "Anterior-Posterior impedance cardiography: a new approach to accurate, non-invasive monitoring of cardiac function.", *Cardiovasc Eng*, vol. 10, pp. 52-65, 2010.
- [15] W. H. Tang and W. Tong, "Measuring impedance in congestive heart failure: current options and clinical applications.", *Am Heart J*, vol. 157(3), pp. 402-11, 2009.
- [16] U. G. Kyle, I. Bosaeus, A. D. De Lorenzo, P. Deurengh, M. Ellia, J. M. Gómez, B. L. Heltmann, L. Kent-Smith, J. C. Melchior, M. Pirlich, H. Scharfetter, A. M. W. J. Schols and C. Pichard, "Bioelectrical impedance analysis - part I: review of principles and methods.", *Clinical Nutrition*, vol. 23, pp. 1226-43, 2004.
- [17] D. G. Abad, "Development of a capacitive bioimpedance measurement system.", 2009.
- [18] E. J. Berbari, "Principles of Electrocardiography" in *Biomedical Engineering Handbook*,

Bibliographic References

2nd ed., vol. I, 2000.

- [19] M. S. Thaler, *The only EKG you'll ever need*, Lippincott William and Wilkins, 2007.
- [20] A. Lozano, J. Rosell and R. Pallás-Areny, "Two-frequency impedance plethysmograph: real and imaginary parts.", *Med. and Biol. Eng. and Comput.*, vol. 23, pp. 38-42, 1990.
- [21] R. P. Patterson, "Possible technique to measure ventricular volume using electrical impedance measurements with and oesophageal electrode.", *Med and Biol Eng and Comput*, vol. 25, pp. 677-79, 1987.
- [22] E. N. Taka, "Transvarredura por bioimpedância: uma ferramenta para detecção precoce de câncer de mama em mulheres jovens.", 2008.
- [23] W. G. Kubicek and R. P. Patterson, "An electronic system for cardiac and metabolic evaluation.", *Journal of applied physiology*, vol. 19(1), pp. 153-156, 1964.
- [24] W. G. Kubicek, R. P. Patterson, J. N. Karnegis, D. A. Witsoe and R. H. Mattson, "Development and evaluation of an impedance cardiac output system.", *Aerosp Med*, vol. 37(12), pp. 1208-12, 1966.
- [25] W. G. Kubicek, R. P. Patterson and D. A. Witsoe, "Impedance Cardiography as a non-invasive method for monitoring cardiac function and other parameters of the cardiovascular system." in *Annals of the New York Academy of Sciences*, 1970.
- [26] A. Sherwood, "Methodological Guidelines for Impedance Cardiography.", *Journal of Psychophysiology*, pp. 1-23, 1990.
- [27] B. C. Penney, N. A. Patwardhan and H. B. Wheeler, "Simplified electrode array for impedance cardiography.", *Medical and Biological Engineering and Computing*, vol. 23, pp. 1-2, 1985.
- [28] M. Qu, Y. Zhang, J. Webster and W. J. Tompkins, "Motion Artifact from Spot and Band Electrodes During Impedance Cardiography.", *IEEE Transactions on Biomedical Engineering*, vol. 33 (11), pp. 1029 - 1036 , 1986.
- [29] K. H. Tan, F. O. Lai and N. C. Hwang, "Measurement of cardiac output using Physio Flow with different positions of electrode placement.", *Singapore Med J*, vol. 47(11), pp. 967-70, 2006.
- [30] NeuMedx, "PhysioFlow - Noninvasive Hemodynamics Redefined.", England, Britol, 2009.
- [31] Biopac, "Single Spot Electrodes for ICG", 2013. [Online]. Available: <http://www.biopac.com/single-spot-electrodes-for-icg>. [Accessed 8 July 2013].
- [32] D. P. Bernstein, "A new stroke volume equation for thoracic electrical bioimpedance: theory and rationale.", *Crit Care Med*, vol. 14(10), pp. 904-9, 1986.
- [33] H. H. Woltjer, B. W. G. J. Arntzen, H. J. Boogard and P. M. J. M. De Vries, "Optimalisation of the spot electrode array in impedance cardiography.", *Med and Bio Eng and Comput*, vol. 34, pp. 84-87, 1996.
- [34] P. K. Kauppinen, J. A. Hyttinen and J. A. Malmivuo, "Sensitivity distributions of impedance cardiography using band and spot electrodes analysed by three-dimensional computer model.", in *Annals of Biomedical Engineering*, 1998.
- [35] J. J. McGrath, W. H. O'Brien, H. Hassinger and P. Shah, "Comparability of spot versus band electrodes for impedance cardiography.", *Journal of Psychophysiology*, vol. 19(2),

Bibliographic References

- pp. 1-9, 2005.
- [36] "VU-AMS Ambulatory Monitoring System", Vrije Universiteit, 2013. [Online]. Available: http://www.vu-ams.nl/fileadmin/user_upload/manuals/VU-DAMS_manual_v1.1.pdf. [Accessed 01 July 2013].
 - [37] G. H. M. Willemsen, E. J. C. De Geus, C. H. A. M. Klaver, L. J. P. Van Doornen and D. Carrol, "Ambulatory Monitoring of The Impedance Cardiogram.", *Psychophysiology*, vol. 33, pp. 184-193, 1996.
 - [38] W. M. Portnoy and R. M. David, "Insulated ECG electrodes", 1973.
 - [39] J. Rosell, J. Colominas, P. Riu and R. Pallas-Areny, "Skin impedance from 1 Hz to 1MHz.", *Biomedical Engineering*, vol. 35(8), pp. 649-51, 1988.
 - [40] L. Wang and R. Patterson, "The effect of blood resistivity changes on impedance cardiography determined by 3D finite difference models of human thorax.", in *Engineering in Medicine and Biology Society, 1992 14th Annual International Conference of the IEEE*, Paris, France, 1992.
 - [41] S. N. Mohapatra, Non-invasive cardiovascular monitoring by electrical impedance technique, Pitman Medical, 1981.
 - [42] G. Cybulski, "Dynamic Impedance Cardiography - the system and its applications.", *Pol J Med Phys Eng*, vol. 11(3), pp. 127-209, 2005.
 - [43] R. P. Patterson, "Impedance cardiography: what is the source of the signal.", *J Phys Conf Ser*, vol. 224(1), 2010.
 - [44] J. Vedru, "Electrical impedance methods fro the measurement of stroke volume in man: state of art.", 2000.
 - [45] D. P. Bernstein, "Impedance cardiography: Pulsatile blood flow and the biophysical and electrodynamic basis for the stroke volume equations.", *J. Electr. Bioimp.*, vol. 1, pp. 2-17, 2010.
 - [46] D. W. Hill, Thompson and F. D., "The importance of blood resistivity in the measurement of cardiac output by the thoracic impedance method.", *Medical and Biological Engineering*, pp. 187-188, 1975.
 - [47] E. Spiridon and S. H. Fairclough, "Detection of anger with and without control of affective computing systems.", *IEEE*, 2009.
 - [48] I. Ovsyshcher and S. Furman, "Impedance cardiography for cardiac output estimation in pacemaker patients: review of the literature.", *Pacing Clin. Electrophysiol.*, vol. 16(7 pt.1), pp. 1412-22, 1993.
 - [49] V. S. Altés, "AD5933-Based system for transtoracic impedance measurements", 2012.
 - [50] V. K. Pandey and P. C. Pandey, "Cancellation of respiratory artifact in impedance cardiography." in *Proceeding of the 2005 IEEE Engineering in Medicine and Biology 27th Annual Conference*, 2005.
 - [51] B. E. Hurmitz, L.Y. Shyu, C.C. Lu, S. P. Reddy, N. Schneiderman and J. H. Nagel, "Signal fidelity requirements for deriving impedance cardiographic measured of cardiac function over a broad heart rate range.", *Biological Psychology*, vol. 36, pp. 3-21, 1993.
 - [52] E. J. Freeman, M. Lalli, A. Karcz, A. Panasyuk, R. Bokhenik and M. G. Bock, "Impedance

Bibliographic References

- measuring devices and methods for emergency cardiovascular care.". US Patent US20130023781 A1, 2013.
- [53] J. M. Ernst, D. A. Litvack, D. L. Lozano, J. T. Cacioppo and G. G. Berntson, "Impedance pneumography: noise as signal in impedance cardiography.", *Psychophysiology*, vol. 36, pp. 333-338, 1999.
 - [54] J. H. Houtvenn, P. F. Groot and E. J. C. de Geus, "Validation of thoracic impedance derived respiratory signal using multilevel analysis.", *International Journal of Psychophysiology*, vol. 59, pp. 97-106, 2006.
 - [55] Z. Lababidi, D. A. Ehmke, R. E. Durnin, P. E. Leaverton and R. M. Lauer, "The first derivative thoracic impedance cardiogram.", *Circulation*, vol. 41, pp. 651-8, 1970.
 - [56] "Clinical applications of bioelectricity." in *Biomedical Engineering Desk Reference*, Academic Press, 2009, pp. 347-49.
 - [57] S. Rush, A. J. Abildskov and R. McFee, "Resistivity of body tissues at low frequencies.", *Circulation Research*, vol. 12, pp. 40-50, 1963.
 - [58] E. Borges, M. Sequeira, A. F. V. Cortez, H. C. Pereira, T. Pereira, V. Almeida, J. Cardoso and C. Correia, "Assessment of Physiological States of Plants in situ - An Innovative Approach to the use of Electrical Impedance Spectroscopy." in *BIOTECHNO 2013*, 2013.
 - [59] "Biological tissue-equivalent phantoms usable in broadband frequency range." *Thechnical Journal*, vol. 7 (4), pp. 61-65, 2006.
 - [60] H. Kato and T. Ishida, "Development of an agar phantom adaptable for simulation of various tissues in the range 5-40 MHz.", *Phys. Med. Biol.*, vol. 32 (2), pp. 221-226, 1987.
 - [61] S. A. Solazzo, Z. Liu, M. Ahmed, A. U. Hines-Peralta, R. E. Lenkinski, S. M. Lobo and S. N. Goldberg, "Radiofrequency ablation: importance of background tissue electrical conductivity - an agar phantom and computer modeling study.", *Radiology*, vol. 236, pp. 495-502, 2005.
 - [62] Analog Devices, *AD5933: 1 MSPS, 12-Bit Impedance Converter, Network Analyzer - Datasheet*, Analog Devices, 2011, pp. 1-36.
 - [63] Analog Devices, *Eval-AD5933EB: Evaluation Board for the 1 MSPS 12-Bit Impedance Converter Network Analyzer - Preliminary Technical Data*, Analog Devices, 2007, pp. 1-28.
 - [64] Philips Semiconductors, *The I2C-bus and how to use it (including specifications)*, 1995.
 - [65] E. Murphy and C. Slattery, "All about digital synthesis.", *Analog Dialog*, vol. 38(8), 2004.
 - [66] C. Margo, J. Katrib, M. Nadi and A. Rouane, "A four-electrode low frequency impedance spectroscopy measurement system using the AD5933 measurement chip.", *Physiol. Meas.*, vol. 34, pp. 391-405, 2013.
 - [67] J. Hoja and G. Lentka, "Portable analyzer for impedance spectroscopy.", in *XIX IMEKO World Congress - Fundamental and Applied Metrology*, 2009.
 - [68] A. A. Pena, "A feasibility study of the suitability of an AD5933-based spectrometer for EBI applications.", Sweden, 2009.
 - [69] H. Berney and J. O'Riordan, "Impedance Measurement Monitors Blood Coagulation.", *Analog Dialogue*, vol. 42, pp. 1-3, 2008.
 - [70] J. Ferreira, F. Seoanne, A. Ansele and R. Bragos, "AD5933-based Spectrometer for

Bibliographic References

- Electrical Bioimpedance.", *IICEB*, pp. 1-4, 2010.
- [71] S. Brennan, "Measuring a grounded impedance profile using the AD5933 - application note", 2012.
 - [72] S. Brennan, "Measuring a loudspeaker impedance profile using the AD5933 - application note," 2007.
 - [73] Analog Devices, "High accuracy impedance measurements using 12-bit impedance converters - circuit note", 2011.
 - [74] H. Berney and J. O'Riordan, "Impedance measurement monitors blood coagulation.", *Analog Dialog*, vol. 42(8), 2008.
 - [75] Texas Instruments, *TLC070, TLC071, TLC072, TLC073, TLC074, TLC075, TLC07xA Family of wide-bandwidth high-output-drive single supply operational amplifiers*, 2004.
 - [76] Texas Instruments, *OPA860 - Wide bandwidth operational transconductance amplifier (OTA) and buffer*, 2008.
 - [77] S. Armstrong and D. Jennings, "Current injection electrodes for electrical impedance tomography.", *Physiol. Meas.*, vol. 25, pp. 797-802, 2004.
 - [78] P. Bertemes, "Tissue characterisation using an impedance spectroscopy probe.", 2002.
 - [79] R. Bragós, J. Rosell and P. Riu, "A wide band AC-coupled current source for electrical impedance tomography.", *Physiol. Meas.*, 1994.
 - [80] Analog Devices, *AD8220 - JFET input instrumentation amplifier with rail-to-rail output in MSOP package*, 2010.
 - [81] Y. Laaziri, F. Mounaim, E. Elzayat, M. Sawan and M. M. Elhilali, "Electrode-tissues interface: Modelling and acute experiments on dogs.", in *10th Annual Conference of the International FES Society*, 2005.
 - [82] 100RandomTasks, "ECG front end" [Online]. Available: <http://www.100randomtasks.com/ecg-front-end>. [Accessed 5 August 2013].
 - [83] Y. Matsuzaka, T. Ichihara, T. Abe and H. Mushiake, "Bio-amplifier with Driven Shield Inputs to Reduce Electrical Noise and its Application to Laboratory Teaching of Electrophysiology.", *JUNE*, vol. 10(2), pp. 118-124, 2012.
 - [84] M. Schmidt and H. Lipson, "Eureqa (Version 0.98 beta) [Software]", 2013. [Online]. Available: <http://www.eureqa.com/>.
 - [85] B. C. Penney, N. A. Patwardhan and H. B. Wheeler, "Simplified electrode array for impedance cardiography.", *Medical and Biological Engineering and Computing*, vol. 23, pp. 1-2, 1985.
 - [86] P. Konrad, "ABC of EMG - A practical introduction to Kinesiological Electromiography.", 2005.
 - [87] L. Churchill, "Electrocardiography", 2000. [Online]. Available: http://web.squ.edu.om/med-Lib/MED_CD/E_CDs/anesthesia/site/content/v03/030343r00.HTM. [Accessed 09 August 2013].
 - [88] J. Pan and W. Tompkins, "A real-time QRS detection algorithm.", *IEEE trans Biomed Eng*, vol. 32(3), pp. 230-236, 1985.

Bibliographic References

- [89] M. A. Rahman and S. Rahman, "Assessment of reliability of Hamilton-Tompkins algorithm to ECG parameter detection." in *Proceedings of the 2012 International Conference on Industrial Engineering and Operations Management Istanbul*, Istanbul, 2012.
- [90] S. M. M. Naidu, P. C. Pandey and V. K. Pandey, "Automatic detection of characteristic points in Impedance Cardiography." in *Computing Cardiology*, 2011.
- [91] P. Carvalho, R. P. Paiva, J. Henriques and M. Antunes, "Robust characteristic points for ICG: definition and comparative analysis." in *Biosignals - International Conference on Bio-inspired Systems and Signal Processing*, 2011.
- [92] R. Van Lien, N. M. Schutte, J. H. Meijer and E. J. C. De Geus, "Estimated pre-ejection period (PEP) based on the detection of the R-wave and dZ/dt-min peaks does not adequately reflect the actual PEP across a wide range of laboratory and ambulatory conditions.", *International Journal of Psychophysiology*, vol. 87, pp. 60-69, 2013.
- [93] G. G. Berntson, D. L. Lozano, Y.-J. Chen and J. T. Cacioppo, "Where to Q in PEP.", *Psychophysiology*, vol. 41, pp. 333-337, 2004.
- [94] Biopac, "Cardiac output measurement using EBI100C and LEAD110S.", 2008.
- [95] H. Zhang and J. K. J. Li, "Noninvasive monitoring of transient cardiac changes with impedance cardiography.", *Cardiovasc Eng*, vol. 8, pp. 225-31, 2008.
- [96] M. Kanani and M. Elliot, "A change in posture." in *Applied Surgical Physiology Vivas*, Cambridge University Press, 2004.
- [97] A. Sherwood, J. McFetridge and J. S. Hutchseson, "Ambulatory impedance cardiography: a feasibility study.", *J Appl Physiol*, vol. 85, pp. 2365-69, 1998.
- [98] M. J. E. Parry and J. McFetridge-Durdle, "Ambulatory impedance cardiography - a systematic review.", *Nursing Research*, vol. 55(4), pp. 283-91, 2006.
- [99] N. Townsend, "ECG instrumentation", 2001.
- [100] B. H. Brown, D. C. Barber, A. H. Morice and A. D. Leathard, "Cardiac and respiratory related electrical impedance changes in the human thorax.", *IEEE Transactions on Biomedical Engineering*, vol. 41(8), pp. 729-34, 1994.
- [101] R. N. Baumgartner, W. C. Chumlea and A. F. Roche, "Bioelectric impedance phase angle and body composition.", *Am. J. Clin. Nutr.*, vol. 48, pp. 16-23, 1988.
- [102] L. J. Vorvick, "Pulse", U.S. National Library of Medicine - National Insitute of Health, 2013. [Online]. Available: <http://www.nlm.nih.gov/medlineplus/ency/article/003399.htm>. [Accessed 10 August 2013].

Appendix

Contents

Appendix A: Reference Values for Thoracic Impedance.....	113
Appendix B: Reference values for Hemodynamic Parameters.....	115
Appendix C: Circuit Schematics	117
Appendix D: Current evaluation on board	121
Appendix E: Calibration model fitting curves	123
Appendix F: Uncertainties of the automated calibration procedure.....	125
Appendix G: Relevant parameters from the signal analysis and respective uncertainties ...	129
Appendix H: Impedance data resume from simultaneous acquisitions of impedance and ECG	131
Appendix I: Averaged ICG waves	137

Appendix A: Reference Values for Thoracic Impedance

The typical values of thoracic impedance were compiled from different sources in the literature in order to serve as a reference for comparison, the results are presented in table 31. The interval of impedance values can be considered to incorporate good estimates for the accepted range of frequencies for ICG applications.

Table 31) Thoracic impedance typical values: compilation from several sources.

Parameter	Interval of reference values	References
Base thoracic impedance (Z_0)	Male: 20 – 30 Ω Female: 25 – 35 Ω 15 – 45 Ω	Biopac Systems, 2008 [94] Cybulski, 2011 [4] Brown et al., 1994 [100] Bernstein et al., 2010 [45]
Base thoracic phase shift (Θ_0)	Male: 7.71 – 13.21° Female: 6.4 – 10.92°	Baumgartner et al., 1988 [101] Cybulski, 2011 [4]
Respiratory component amplitude (ΔZ_r)	0.675 – 2.025 Ω	Brown et al., 1994 [100] Lozano et al., 1990 [20]
Cardiac component amplitude (ΔZ_c)	0.04 – 0.4 Ω	Brown et al., 1994 [100] Cybulski, 2011 [4] Lozano et al. 1990 [20] Bernstein et al., 2010 [45] Bronzino, 2006 [12]
(dZ/dt)_{max}	0.8 – 2.5 Ω/s	Biopac Systems, 2008 [94] Bronzino, 2006 [12]

Appendix B: Reference values for Hemodynamic Parameters

The typical values for the hemodynamic parameters that can be determined by ICG's signal analysis are presented in table 32. The hemodynamics tend to be affected by the body posture, that way its relevant to indicate the values in the reference position (supine) and those reported while sitting, to make a more accurate comparison with the results of the acquisitions during this project. The heart rate is only indicated for completeness, since the values resulting from the signal analysis were directly compared with measurements on the subjects with an arm cuff.

Table 32) Hemodynamic parameters reference values compilation [94, 102] and interval of reported values while sitting [97, 98].

Parameter	Interval of reference values	Interval of reported values while sitting
Heart Rate (HR)	60 – 100 bpm	-
Left Ventricular Ejection Time (LVET)	0.25 – 0.35 s	0.26 - 0.31
Pre-ejection Period (PEP)	0.05 – 0.12 s	0.11 - 0.14
Stroke Volume (SV)	60 - 100 mL/beat	74.5 - 142.7
Cardiac Output (CO)	4 - 8 L/min	-

Appendix C: Circuit Schematics

Impedance meter unit

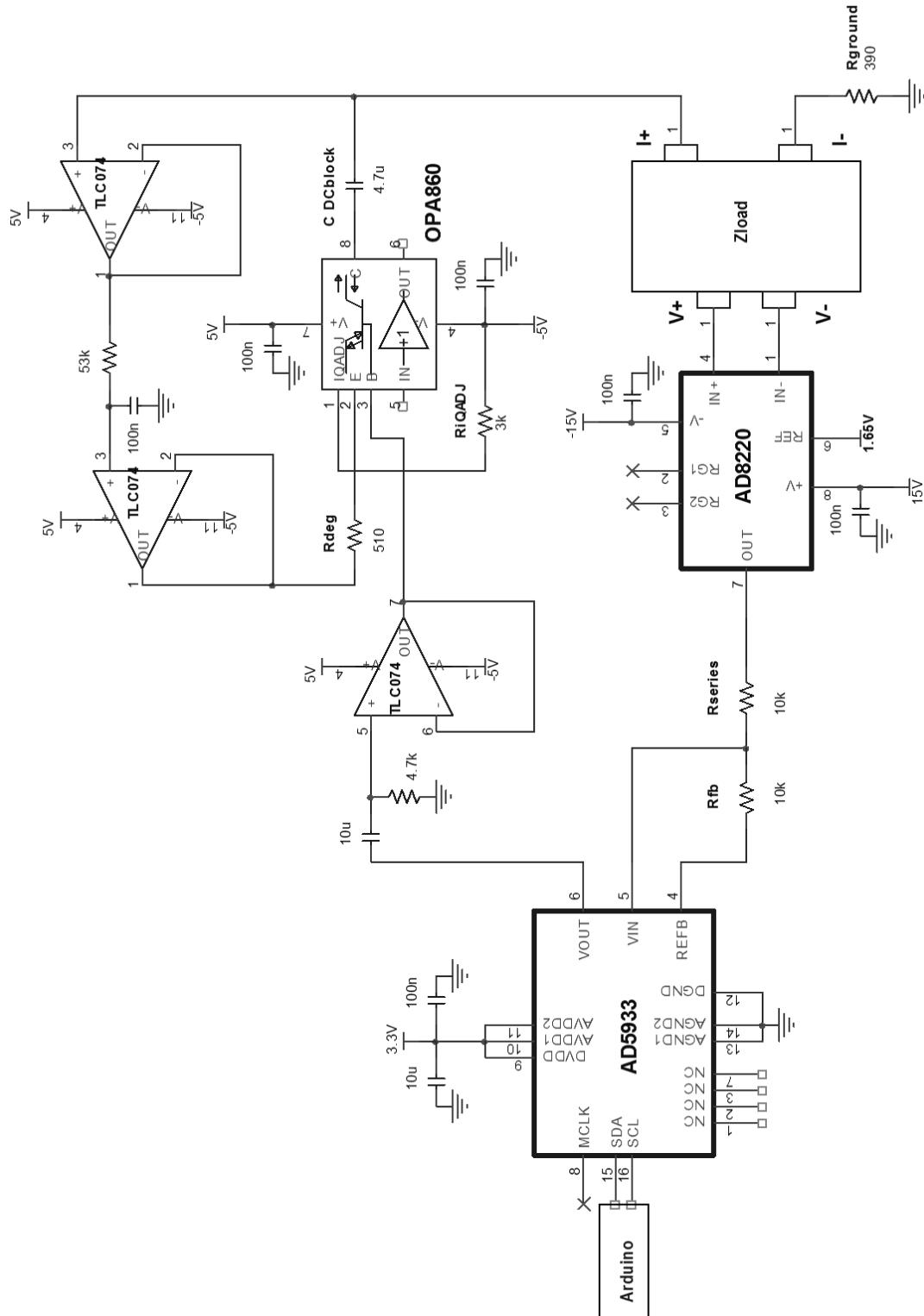


Figure 61) Signal conditioning circuit schematic. All the resistor values are in units of ohm (Ω) and the capacitors in farads (F).

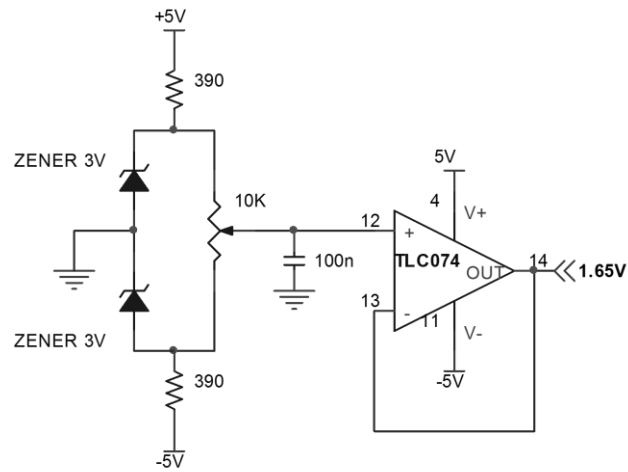


Figure 62) AD8220 reference generation circuit. The resistors values are presented in units of ohm (Ω) and the capacitors values are in farad (F).

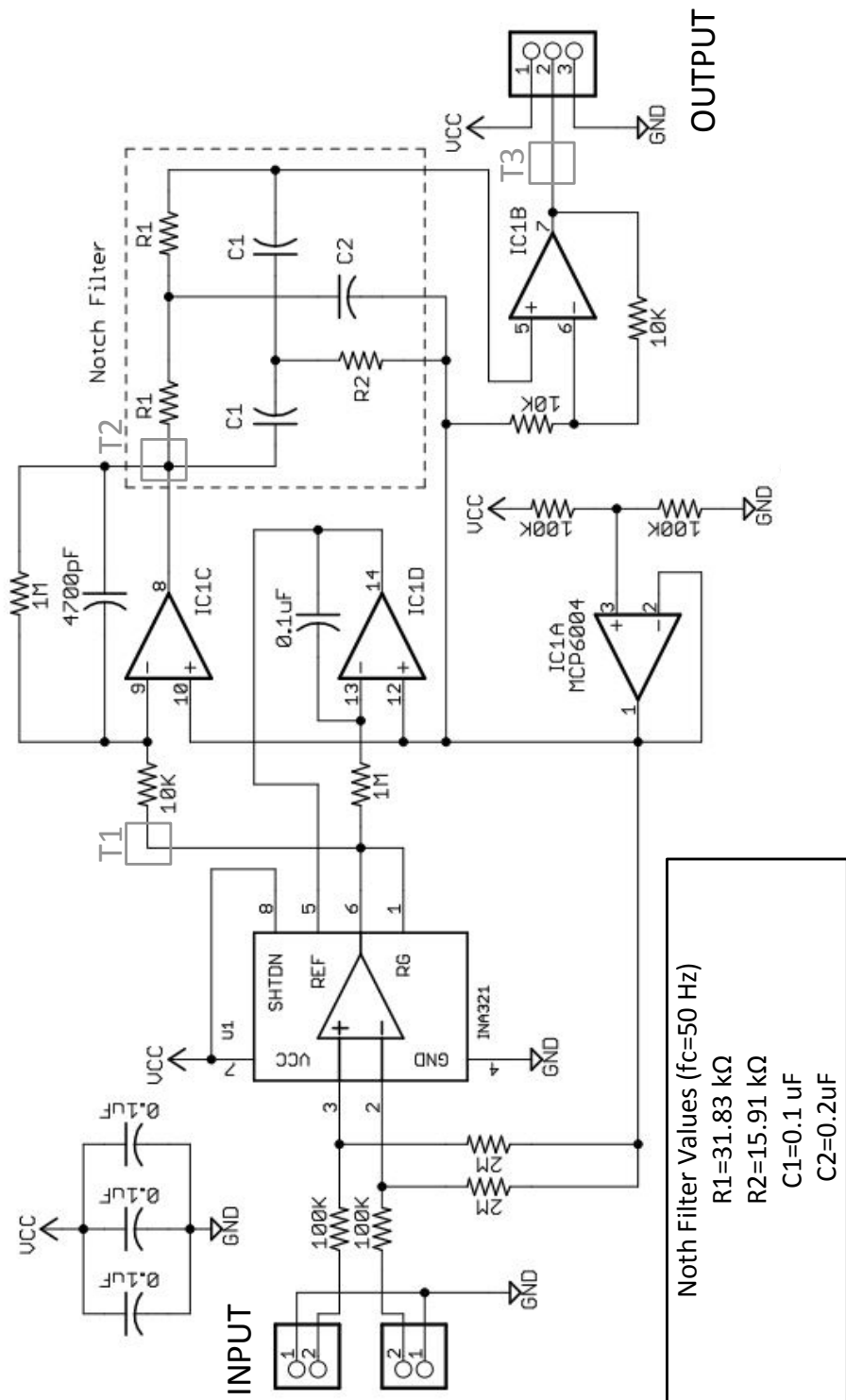


Figure 63) ECG front-end circuit scheme [82], directly extracted from the producers web page. The squares represent test points (T1, T2, T3).

Appendix D: Current evaluation on board

The evaluation of the current output presented on section 5.2 was extended and other tests were conducted based on the principles described there. The current after the blocking capacitor was studied based on an estimative of the total resistance in the current path equal to the load plus the grounded resistor value – also resulting in a systematic error for excess.

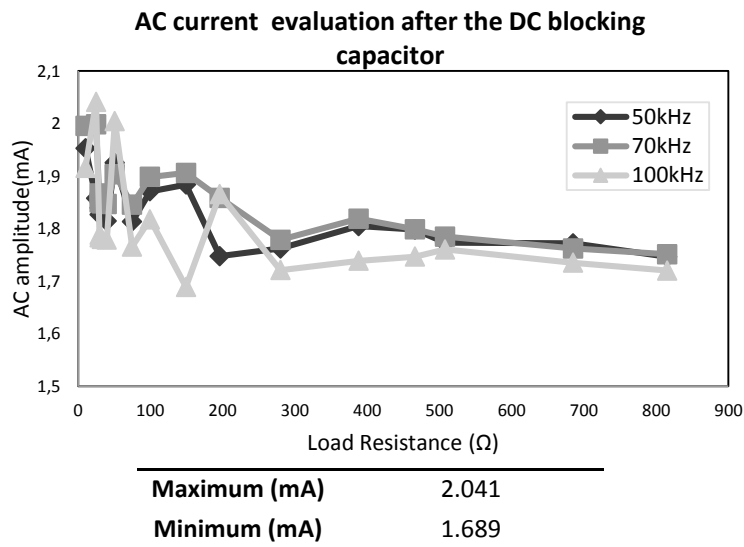


Figure 64) PCB: Current amplitude through the path to the ground on the DC blocking capacitor output.

The current amplitude is inside the safe range proposed for the ICG applications (<2.5 mA as the most limitative value at 50 kHz, section 2.4.1).

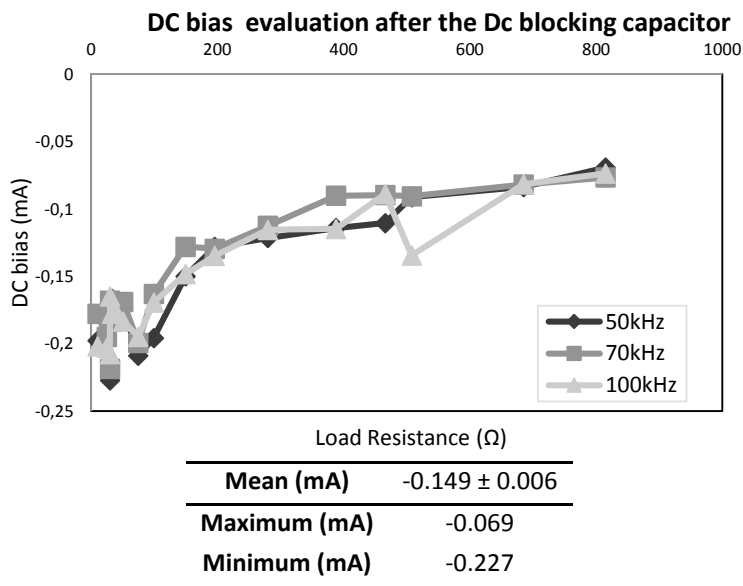


Figure 65) PCB: DC bias current through the path to the ground on the DC blocking capacitor output.

The DC bias results are below the human sensibility limit (<0.6 mA in module, section 2.4.1).

Appendix E: Calibration model fitting curves

The calibration models were established as a result of a fitting procedure to obtain the description of the calibration parameters as a function of the raw amplitude. Those models were chosen based on the ratio of accuracy to complexity, avoiding the model over fitting to the train data.

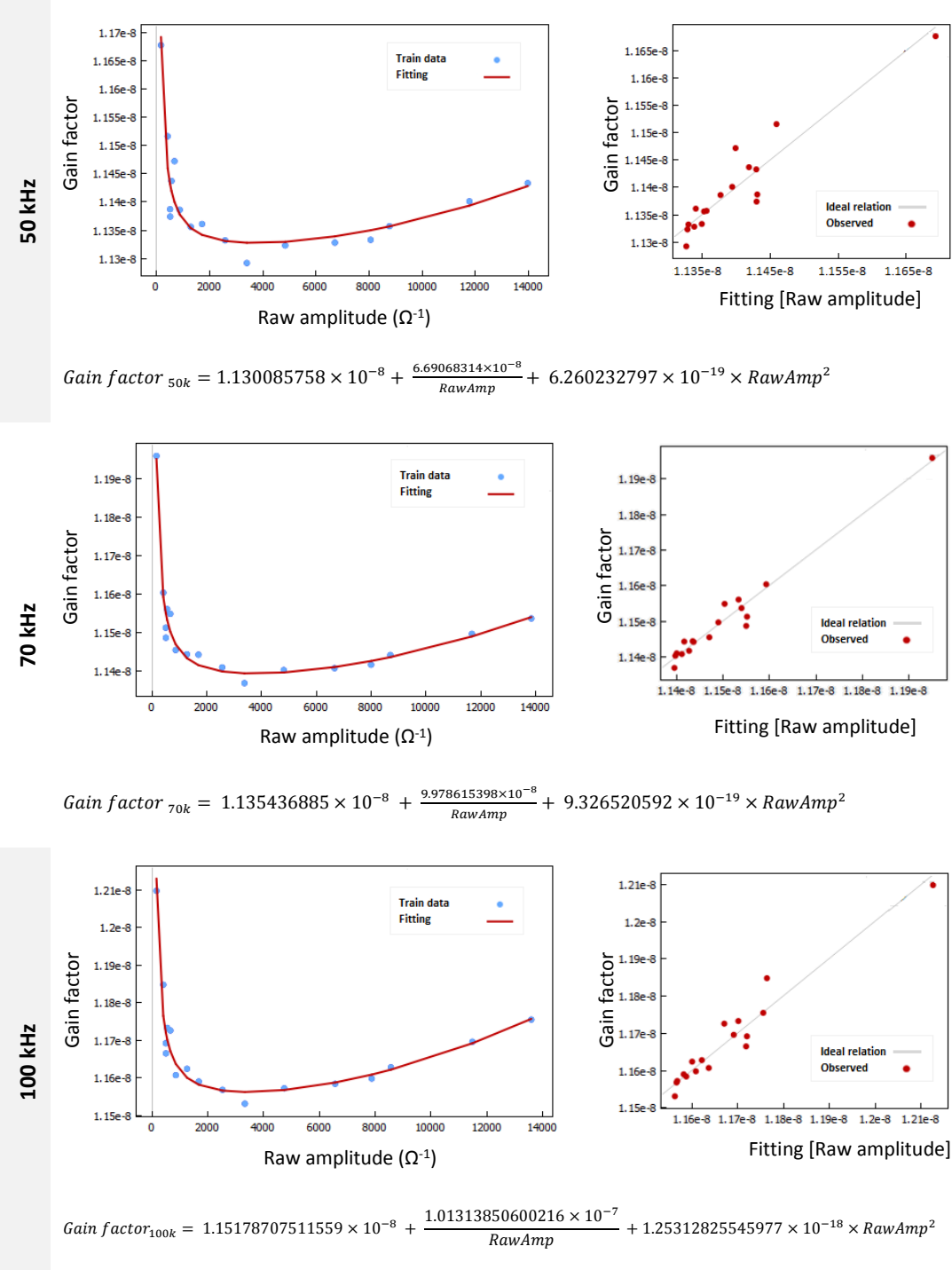


Figure 66) Gain factor at 50, 70 and 100 kHz: fitting results from Eureka mathematical software (left) and the relation between the real gain factor and the result from the model (right). The mathematical expression for each frequency is presented.

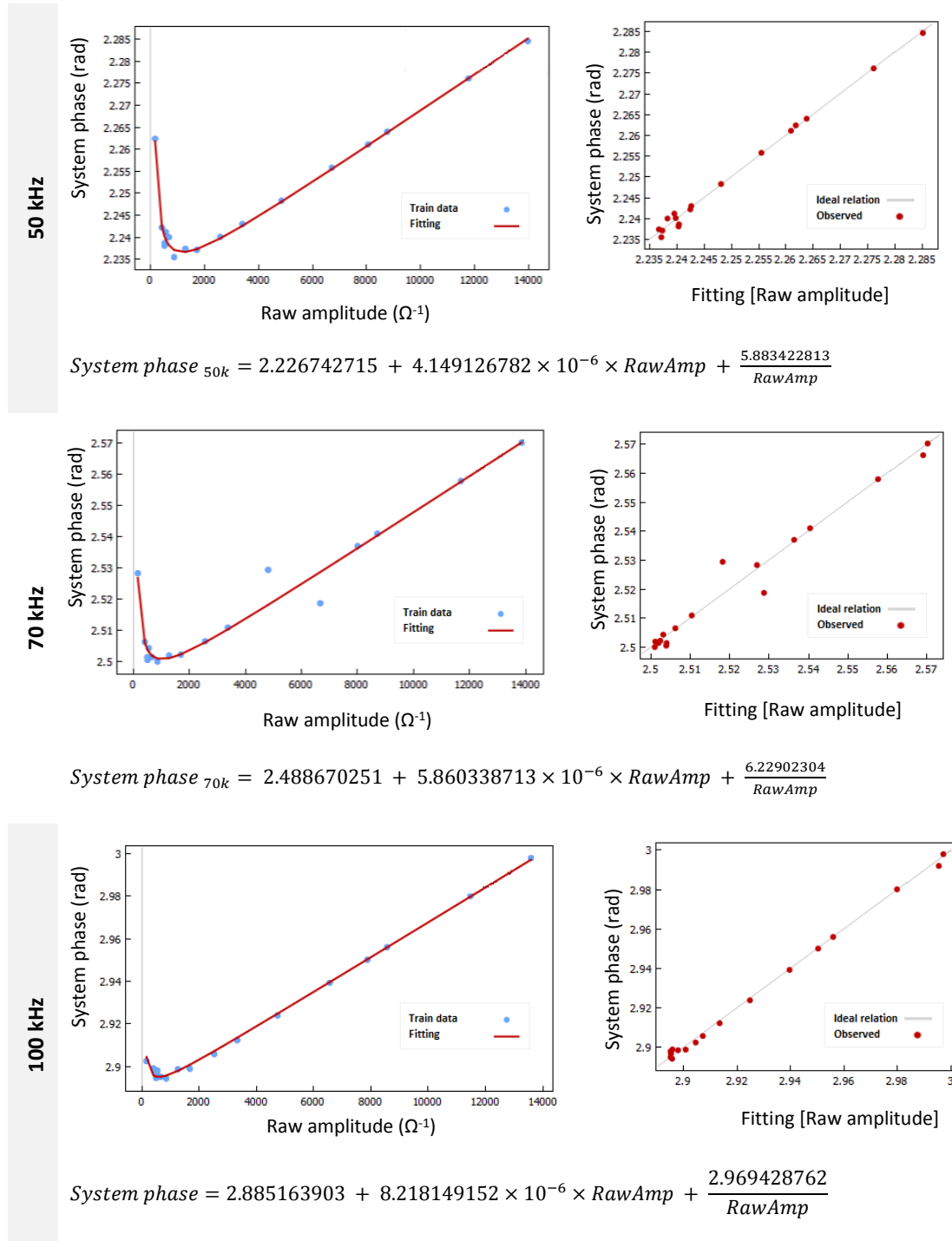


Figure 67) System phase at 50, 70 and 100 kHz: fitting results from Eureqa mathematical software (left) and the relation between the real gain factor and the result from the mode (right). The mathematical model for each frequency is presented and are defined in radians.

The results are defined and presented in radians, since the user interface performs calculations that way.

The fitting results showed enough complexity to provide calibration parameters with overall accordance to the original ones, without overfitting the data.

Appendix F: Uncertainties of the automated calibration procedure

To study how a single pair of calibration values to correct a varying impedance would affect the results a few tests were carried out. The evaluation was made based on the mean, maximum and minimum non-calibrated amplitude of 2 sets of thoracic data at each of the working frequencies. The data was collected on subject # 3 (Chapter 6) using a configuration with two electrodes vertically aligned on the left side of the neck and other two on the left side of the thorax near the end of the rib cage, the outside electrodes applied the current while the inner electrodes sensed the voltage, as presented on [33]. This configuration was not used during the acquisitions. In this case the impedance was unknown, so the reference was the mean amplitude and phase calibrated by the parameters obtained from the model expressions (Appendix E) based on the mean raw amplitude of the whole acquisition. The analysis was then made in comparative terms. The mean, maximum and minimum designations related to the phase are only indicative, since they correspond to the mean, maximum and minimum raw amplitude.

Table 33) Data set resume: average calibrated reference values from two data sets and standard error of the mean.

Frequency (kHz)	Amplitude (Ω)			Phase ($^{\circ}$)		
	Mean Amplitude	Maximum Amplitude	Minimum Amplitude	Mean phase	Maximum phase	Minimum phase
50	44.207 \pm 0.393	45.157 \pm 0.443	42.967 \pm 0.121	-10.927 \pm 0.106	-11.334 \pm 0.122	-10.461 \pm 0.068
70	41.878 \pm 0.040	42.818 \pm 0.064	40.656 \pm 0.331	-11.016 \pm 0.087	-11.386 \pm 0.064	-10.544 \pm 0.166
100	39.441 \pm 0.136	40.211 \pm 0.190	38.703 \pm 0.083	-10.752 \pm 0.047	-11.063 \pm 0.017	-10.432 \pm 0.059

First, by comparing the raw amplitude determined from the 10 s initial period to the raw data from the whole acquisition, was estimated that a 10 s period would determine the mean raw amplitude during the whole measurement with a maximum error of 2 %. The effect of the error propagation to the calibration factors and its influence on the final measurement was directly simulated by introducing a ± 2 % variation in the raw amplitude, calculating the resultant calibration parameters and using them to correct the mean raw amplitude and raw phase from the whole set of measurements. The absolute difference between the values in either case was still very small (table 34).

Table 34) Maximum discrepancy of the data calibrated using the simulated 10 second period influence of $\pm 2\%$ on the raw amplitude relative to the reference amplitude and phase.

Maximum relative errors of the mean amplitude and phase			
Correction based on +2% Raw Amplitude		Correction based on -2% Raw Amplitude	
Amplitude (Ω)	Phase ($^\circ$)	Amplitude (Ω)	Phase ($^\circ$)
0.0101	0.0052	0.0105	0.0056

The maximum and minimum raw amplitude and raw phase values of each set were used to verify the effect of the constant correction value on the extremes, by first calculating the calibration parameters based on the raw amplitude on the extreme situations and using them to obtain the calibrated values and also simulating the $\pm 2\%$ of the raw amplitude. These values were then compared to the ones obtained with the calibration values from the mean and from the variation of $\pm 2\%$.

Table 35) Maximum discrepancy between the maximum raw values of the data set calibrated using maximum raw amplitude and those same values calibrated using the mean raw amplitude. Also the 10 second period influence of $\pm 2\%$ of the raw amplitude was simulated in both cases and compared.

Maximum relative errors on the maximum amplitude and phase					
Correction based on +2% Raw Amplitude		Correction based on -2% Raw Amplitude		Correction based on Raw Amplitude	
Amplitude (Ω)	Phase ($^\circ$)	Amplitude (Ω)	Phase ($^\circ$)	Amplitude (Ω)	Phase ($^\circ$)
0.0017	0.0008	0.0224	0.0112	0.0119	0.0058

Table 36) Maximum discrepancy between the minimum raw values of the data set calibrated using minimum raw amplitude and those same values calibrated using the mean raw amplitude. Also the 10 second period influence of $\pm 2\%$ of the raw amplitude was simulated in both cases and compared.

Maximum relative errors on the minimum amplitude and phase					
Correction based on +2% Raw Amplitude		Correction based on -2% Raw Amplitude		Correction based on mean Raw Amplitude	
Amplitude (Ω)	Phase ($^\circ$)	Amplitude (Ω)	Phase ($^\circ$)	Amplitude (Ω)	Phase ($^\circ$)
0.0308	0.0168	0.0224	0.0109	0.0213	0.0118

The conclusion from this analysis is that using a calibration based on the mean raw amplitude of a 10 s period has little influence over the values near the mean value around which the oscillation occurs and such abstraction does not show a significant difference from correcting the limit values with the calibration values deduced from the mean raw amplitude.

Table 37) Maximum overall discrepancy detected by studying the effect of a single pair of calibration values based on a 10 second period. This table resumes the last three tables.

Overall maximum discrepancy	
Amplitude (Ω)	Phase ($^\circ$)
0.0308	0.0168

The evaluated errors are none the less small, being an order of magnitude inferior to the errors evaluated on the calibration procedure performance test with resistors.

Appendix G: Relevant parameters from the signal analysis and respective uncertainties

Table 38) Hemodynamic parameters and resume of relevant values for their calculation, with the associated uncertainties.

Category	Parameter	Description	Expression	Uncertainty estimation
Basic values	L (cm)	Distance between the sensing electrodes	-	±1
		Mean thoracic impedance over the periods accepted for ICG averaging	-	Error associated with the system performance (section 5.3.2)
	Z ₀ ' (Ω)			
	ρ (Ω.cm)	Blood resistivity	C ^{ie} = 147	-
Signal features	R _t (s)	R peak ordinate	-	$\delta R_t = \frac{\sum_{i=1}^{n-1} S_t(i) - Q_t(i)}{2 \times n}$, S _t and Q _t are the ordinates of the S and Q ECG waves
	RR (s)	Average R-R interval	$RR = \frac{\sum_{i=1}^{n-1} R_t(i+1) - R_t(i)}{n}$	δRR = standard error of the mean
	B _t (s)	B point ordinate	-	$\delta B_t = \frac{Bmin_t(i) - C_t(i)}{2}$, B _{min} is the local minimum before C.
	X _t (s)	X point ordinate	-	$\delta X_t = \frac{X_t(i) - C_t(i)}{3}$
	(dz/dt) _{max} (Ω/cm)	C point abscissa	-	δ(dz/dt) _{max} = standard error of the mean of ensemble averaged samples at C _t
Rate	HR (bpm)	Heart rate	$HR = \frac{60}{RR}$	$\delta HR = \frac{60}{RR^2} \delta RR$
Systolic Times	PEP (s)	Pre-ejection time	$PEP = B_t - R_t + 0.048$	$\delta PEP = \sqrt{\delta B_t^2 + \delta R_t^2}$
	LVET (s)	Left ventricular ejection time	$LVET = X_t - B_t$	$\delta LVET = \sqrt{\delta X_t^2 + \delta B_t^2}$
Cardiac volumes	SV (mL/beat)	Stroke volume	$SV = \rho \times (dz/dt)_{max} \times LVET \times \left(\frac{L}{Z_0}\right)^2$	$\delta SV = \rho \frac{L}{Z_0^2} \sqrt{(LVET \times L \times \delta(dz/dt)_{max})^2 + ((dz/dt)_{max} \times L \times \delta LVET)^2 + (2 \times (dz/dt)_{max} \times LVET)^2 \times \left(\delta L^2 + \left(\frac{L}{Z_0'} \delta Z_0'\right)^2\right)}$
	CO (L/min)	Cardiac output	$CO = SV \times 10^{-3} \times HR$	$\delta CO = \sqrt{(HR \times \delta SV)^2 + (SV \times \delta HR)^2} \times 10^{-3}$

Appendix H: Impedance data resume from simultaneous acquisitions of impedance and ECG

The data resume from the simultaneous acquisitions of impedance and ECG on 3 subjects is presented, relative to the thoracic impedance, cardiac component and respiratory component. These results are under the influence of the ECG/ICG crosstalk. These values in general terms are near the ones obtained without the ECG simultaneous acquisitions, but present distinct influences as a function of the AC-current frequency and electrode configuration. For that reason were used only to evaluate the maximum error introduced by this crosstalk.

Anteroposterior configuration

Table 39) Thoracic impedance average (Z_0) values obtained from two acquisitions at each frequency for the anteroposterior configuration. The uncertainties for the amplitude and phase are the constants determined on section 5.3.2, in the case of the real and imaginary values an error propagation was performed.

#	F (kHz)	L (cm)	$ Z_0 $ (Ω)	Θ_0 ($^\circ$)	R_{Z_0} (Ω)	X_{Z_0} (Ω)
1	50	25 \pm 1	18.30 \pm 1.38	-4.64 \pm 1.88	18.24 \pm 1.38	-1.48 \pm 0.61
	100		17.48 \pm 1.38	-7.65 \pm 1.88	17.33 \pm 1.37	-2.33 \pm 0.60
2	50	21 \pm 1	15.47 \pm 1.38	-4.21 \pm 1.88	15.43 \pm 1.38	-1.14 \pm 0.52
	100		14.84 \pm 1.38	-5.18 \pm 1.88	14.78 \pm 1.38	-1.34 \pm 0.50
3	50	24 \pm 1	21.24 \pm 1.38	-3.80 \pm 1.88	21.20 \pm 1.38	-1.41 \pm 0.70
	100		20.17 \pm 1.38	-5.27 \pm 1.88	20.09 \pm 1.38	-1.85 \pm 0.67
Average	-	23 \pm 1	17.92 \pm 0.94	-5.13 \pm 0.51	17.84 \pm 0.94	-1.59 \pm 0.16

Table 40) Peak-to-peak values of the de-noised cardiac impedance component (ΔZ_c) obtained from the thoracic impedance signal for the anteroposterior configuration. The uncertainties were estimated from the standard error of the mean.

#	F (kHz)	$\Delta Z_c $ (Ω)	ΔR_{Z_c} (Ω)
1	50	0.18 \pm 0.01	0.18 \pm 0.01
	100	0.18 \pm 0.01	0.18 \pm 0.01
2	50	0.15 \pm 0.01	0.15 \pm 0.01
	100	0.13 \pm 0.01	0.13 \pm 0.01
3	50	0.21 \pm 0.01	0.21 \pm 0.01
	100	0.16 \pm 0.01	0.16 \pm 0.01
Average	-	0.17 \pm 0.01	0.17 \pm 0.01
% of the base value	-	0.95	0.61

Table 41) Peak-to-peak values of the de-noised respiratory impedance component (ΔZ_r) obtained from the thoracic impedance waves for the anteroposterior configuration. The uncertainties were estimated from the standard error of the mean.

#	F (kHz)	$\Delta Z_r (\Omega)$	$\Delta R_{Z_r}(\Omega)$
1	50	0.05 ± 0.02	0.05 ± 0.02
	100	0.06 ± 0.01	0.06 ± 0.01
2	50	0.23 ± 0.03	0.23 ± 0.03
	100	0.19 ± 0.03	0.19 ± 0.03
3	50	0.20 ± 0.02	0.16 ± 0.02
	100	0.22 ± 0.02	0.19 ± 0.03
Average		-	0.16 ± 0.03
% of the base value		-	0.88
			0.83

Table 42) Values used to calculate the hemodynamic parameters from the anteroposterior configuration.

#	F (kHz)	L (cm)	N beats	$Z_0'(\Omega)$		$(dZ/dt)_{\max}(\Omega/s)$	
				Z	R	Z	R
1	50	25 ± 1	61	18.29 ± 1.38	18.23 ± 1.43	1.82 ± 0.44	1.80 ± 0.43
	100		39	17.51 ± 1.38	17.36 ± 1.43	1.52 ± 0.44	1.49 ± 0.43
2	50	21 ± 1	43	15.47 ± 1.38	15.43 ± 1.43	1.33 ± 0.44	1.31 ± 0.43
	100		14	14.92 ± 1.38	14.86 ± 1.43	1.43 ± 0.44	1.41 ± 0.43
3	50	24 ± 1	50	21.25 ± 1.38	21.20 ± 1.43	2.75 ± 0.44	2.73 ± 0.43
	100		11	20.20 ± 1.38	20.12 ± 1.43	1.66 ± 0.44	1.63 ± 0.43
Average		23 ± 1	218	17.94 ± 0.94	17.86 ± 0.94	1.75 ± 0.19	1.73 ± 0.19

Table 43) Hemodynamic parameters from the anteroposterior configuration.

#	F (kHz)	HR (bpm)	PEP (s)		LVET (s)		SV (ml/beat)		CO (L/min)	
			Z	R	Z	R	Z	R	Z	R
1	50	79.93 ± 0.02	0.13 ± 0.07	0.13 ± 0.07	0.28 ± 0.09	0.28 ± 0.09	139.49 ± 60.09	137.66 ± 59.42	11.15 ± 4.80	11.00 ± 4.75
		75.84 ± 0.05	0.11 ± 0.09	0.11 ± 0.09	0.31 ± 0.10	0.31 ± 0.10	138.95 ± 66.85	140.07 ± 67.42	10.54 ± 5.07	10.62 ± 5.11
	100	68.28 ± 0.05	0.10 ± 0.07	0.10 ± 0.07	0.30 ± 0.09	0.30 ± 0.09	108.76 ± 53.92	108.68 ± 53.75	7.46 ± 3.68	7.46 ± 3.67
		70.07 ± 0.04	0.13 ± 0.06	0.13 ± 0.06	0.29 ± 0.09	0.29 ± 0.09	120.73 ± 57.64	119.60 ± 57.20	8.45 ± 4.04	8.37 ± 4.01
2	50	88.29 ± 0.04	0.11 ± 0.06	0.11 ± 0.07	0.25 ± 0.08	0.25 ± 0.08	130.96 ± 49.77	131.06 ± 49.85	11.56 ± 4.39	11.57 ± 4.40
		86.10 ± 0.03	0.09 ± 0.08	0.08 ± 0.10	0.31 ± 0.10	0.31 ± 0.10	105.12 ± 46.39	105.40 ± 46.34	9.05 ± 3.99	9.07 ± 3.99
	100		0.08 ± 0.01	0.08 ± 0.01	0.10 ± 0.01	0.10 ± 0.01				
Average		78.09 ± 3.06	0.11 ± 0.01	0.11 ± 0.01	0.29 ± 0.01	0.29 ± 0.01	124.00 ± 5.56	123.74 ± 5.51	9.70 ± 0.61	9.68 ± 0.61

The HR (table 43) is in accordance to the physiological acceptable values (60-100 bpm). The individual variations from the initial direct HR measurement (table 21) that can be easily explained by assuming that during the long acquisition process this parameter naturally changed. The PEP value was sometimes higher than the reference values (0.05-0.12 s), but is always inside the interval of values while sitting (0.11-0.14 s). The LVET average value, as well as all the values from all subjects, is inside the reference interval (0.25-0.35 s). The SV is above the reference values (60-100 mL), but is always inside the estimated interval for measurements while sitting (74.5-142.7 mL). The CO is also augmented in accordance to the reference (4-8 L/min) but in average presents a close value, which is related to the SV value but also to the increased heart rate while sitting.

Posterolateral configuration

Table 44) Thoracic impedance average (Z_0) values from the calibrated curves obtained from two acquisitions at each frequency for the posterolateral configuration. The uncertainties for the amplitude and phase are the constants determined on section 5.3.2, for the real and imaginary values an error propagation was made.

#	F (kHz)	L (cm)	$ Z_0 $ (Ω)	Θ_0 ($^\circ$)	R_{Z0} (Ω)	R_{Z0} (Ω)
1	50	36 \pm 1	29.88 \pm 1.38	-6.95 \pm 1.88	29.66 \pm 1.37	-3.61 \pm 0.99
	100		27.43 \pm 1.38	-7.74 \pm 1.88	27.18 \pm 1.37	-3.70 \pm 0.91
2	50	30 \pm 1	24.38 \pm 1.38	-6.98 \pm 1.88	24.20 \pm 1.37	-2.96 \pm 0.81
	100		23.43 \pm 1.38	-4.89 \pm 1.88	23.35 \pm 1.38	-2.00 \pm 0.78
3	50	33 \pm 1	29.86 \pm 1.38	-5.70 \pm 1.88	29.72 \pm 1.38	-2.97 \pm 0.98
	100		28.31 \pm 1.38	-6.70 \pm 1.88	28.11 \pm 1.37	-3.31 \pm 0.94
Average	-	33 \pm 1	27.22 \pm 1.02	-6.49 \pm 0.38	27.04 \pm 1.01	-3.09 \pm 0.23

Table 45) Peak-to-peak values of the de-noised cardiac impedance component (ΔZ_c) obtained from the thoracic impedance signal for the posterolateral configuration. The uncertainties were estimated from the standard error of the mean.

#	F (kHz)	$\Delta Z_c $ (Ω)	ΔR_{Zc} (Ω)
1	50	0.16 \pm 0.01	0.16 \pm 0.01
	100	0.15 \pm 0.01	0.15 \pm 0.01
2	50	0.15 \pm 0.01	0.15 \pm 0.01
	100	0.13 \pm 0.01	0.13 \pm 0.01
3	50	0.20 \pm 0.01	0.20 \pm 0.01
	100	0.20 \pm 0.01	0.19 \pm 0.01
Average	-	0.17 \pm 0.01	0.17 \pm 0.01
% of the base value	-	0.61	0.61

Table 46) Peak-to-peak values of the de-noised respiratory impedance component (ΔZ_r) obtained from the thoracic impedance signal for the posterolateral configuration. The uncertainties were estimated from the standard error of the mean.

#	F (kHz)	$\Delta Z_r (\Omega)$	$\Delta R_{Z_r}(\Omega)$
1	50	0.18 ± 0.02	0.19 ± 0.03
	100	0.16 ± 0.03	0.16 ± 0.03
2	50	0.21 ± 0.01	0.22 ± 0.01
	100	0.18 ± 0.06	0.18 ± 0.06
3	50	0.47 ± 0.04	0.46 ± 0.06
	100	0.45 ± 0.05	0.43 ± 0.06
Average		-	0.28 ± 0.05
% of the base value		-	1.02
			1.00

Table 47) Values used to calculate the hemodynamic parameters from the posterolateral configuration.

#	F (kHz)	L (cm)	N beats	$Z_0'(\Omega)$		$(dZ/dt)_{\max}(\Omega/s)$	
				$ Z $	R	$ Z $	R
1	50	36 ± 1	49	29.87 ± 1.38	29.65 ± 1.43	1.55 ± 0.44	1.54 ± 0.43
	100		55	27.42 ± 1.38	27.17 ± 1.43	1.46 ± 0.44	1.45 ± 0.43
2	50	30 ± 1	19	24.35 ± 1.38	24.17 ± 1.43	1.54 ± 0.44	1.52 ± 0.43
	100		27	23.35 ± 1.38	23.27 ± 1.43	1.30 ± 0.44	1.29 ± 0.43
3	50	33 ± 1	25	29.88 ± 1.38	29.73 ± 1.43	2.43 ± 0.44	2.40 ± 0.43
	100		17	28.36 ± 1.38	28.17 ± 1.43	2.14 ± 0.44	2.11 ± 0.43
Average		33 ± 1	192	27.21 ± 1.04	27.03 ± 1.03	1.74 ± 0.16	1.72 ± 0.16

Table 48) Hemodynamic parameters from the posterolateral configuration.

#	F (kHz)	HR (bpm)	PEP (s)		LVET (s)		SV (ml/beat)		CO (L/min)	
			$ Z $	R	$ Z $	R	$ Z $	R	$ Z $	R
1	50	87.01 ± 0.05	0.12 ± 0.07	0.12 ± 0.07	0.27 ± 0.09	0.27 ± 0.09	88.10 ± 39.32	88.93 ± 39.35	7.67 ± 3.42	7.74 ± 3.42
	100	86.47 ± 0.03	0.12 ± 0.08	0.12 ± 0.08	0.26 ± 0.09	0.26 ± 0.09	95.88 ± 44.61	97.12 ± 45.01	8.29 ± 3.86	8.40 ± 3.89
2	50	69.38 ± 0.04	0.12 ± 0.06	0.12 ± 0.06	0.28 ± 0.08	0.28 ± 0.08	96.26 ± 41.86	96.93 ± 42.08	6.68 ± 2.90	6.73 ± 2.92
	100	70.73 ± 0.05	0.11 ± 0.08	0.11 ± 0.08	0.29 ± 0.09	0.29 ± 0.09	92.46 ± 44.70	92.35 ± 44.57	6.54 ± 3.16	6.54 ± 3.15
3	50	88.54 ± 0.08	0.10 ± 0.06	0.10 ± 0.06	0.26 ± 0.08	0.26 ± 0.08	112.28 ± 41.66	112.78 ± 41.82	9.94 ± 3.69	9.99 ± 3.70
	100	89.41 ± 0.07	0.10 ± 0.07	0.10 ± 0.07	0.27 ± 0.08	0.27 ± 0.08	115.56 ± 44.95	115.03 ± 44.62	10.34 ± 4.02	10.29 ± 3.99
Average		81.93 ± 3.45	0.11 ± 0.003	0.11 ± 0.003	0.27 ± 0.005	0.27 ± 0.005	100.09 ± 4.16	100.52 ± 4.03	8.24 ± 0.60	8.28 ± 0.59

The heart rate (Table 48) between acquisitions (corresponding to different configurations) shows accordance for the same subject. The PEP average value shows no variation between configurations, a close analysis shows that all the values are inside the reference interval. The average LVET is smaller than the one determined for the first

configuration, but is still inside the reference interval. The SV and the CO are in average smaller than those for the first configuration being closer to the reference values.

In both configurations the final values present high uncertainties mostly caused by the error propagation derived from the ECG/ICG crosstalk.

Appendix I: Averaged ICG waves

The ensemble averaged ICG waves obtained from the simultaneous acquisition of impedance and ECG on 3 subjects are presented to illustrate the general influence of the excitation frequency and configuration on the final result. Only the impedance amplitude based waves are presented to avoid redundancy, since the resistance based curves shown the same information. The correspondent cardiac impedance and ECG waves were also averaged to use as visual reference and no parameters were derived from them after averaging. The signals present different total lengths since they were averaged for the minimum R-R period verified within the beat samples selected.

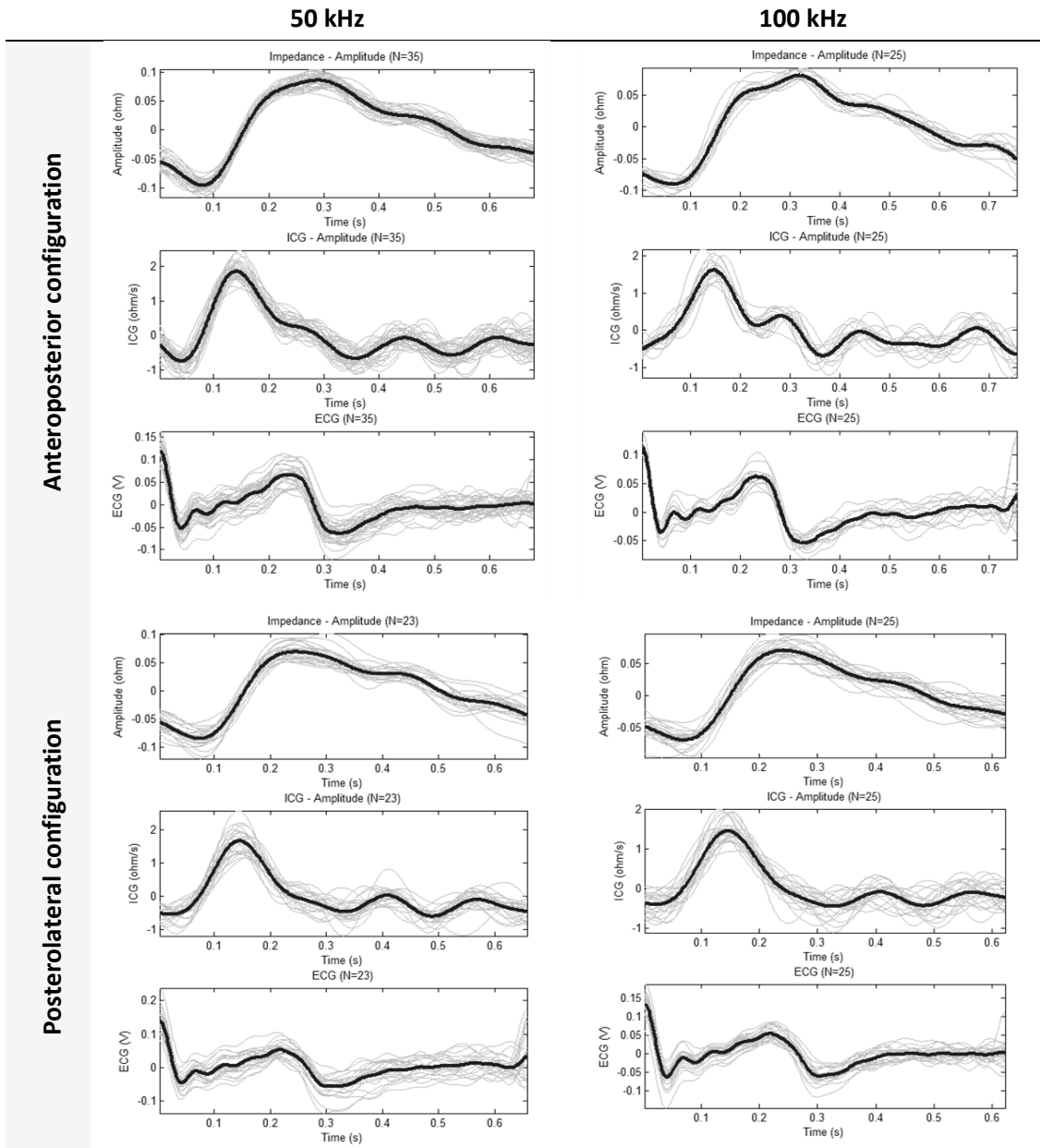


Figure 68) Averaged ICG waves based on the impedance amplitude, for different configurations and different frequencies of the excitatory AC current applied on subject #1.

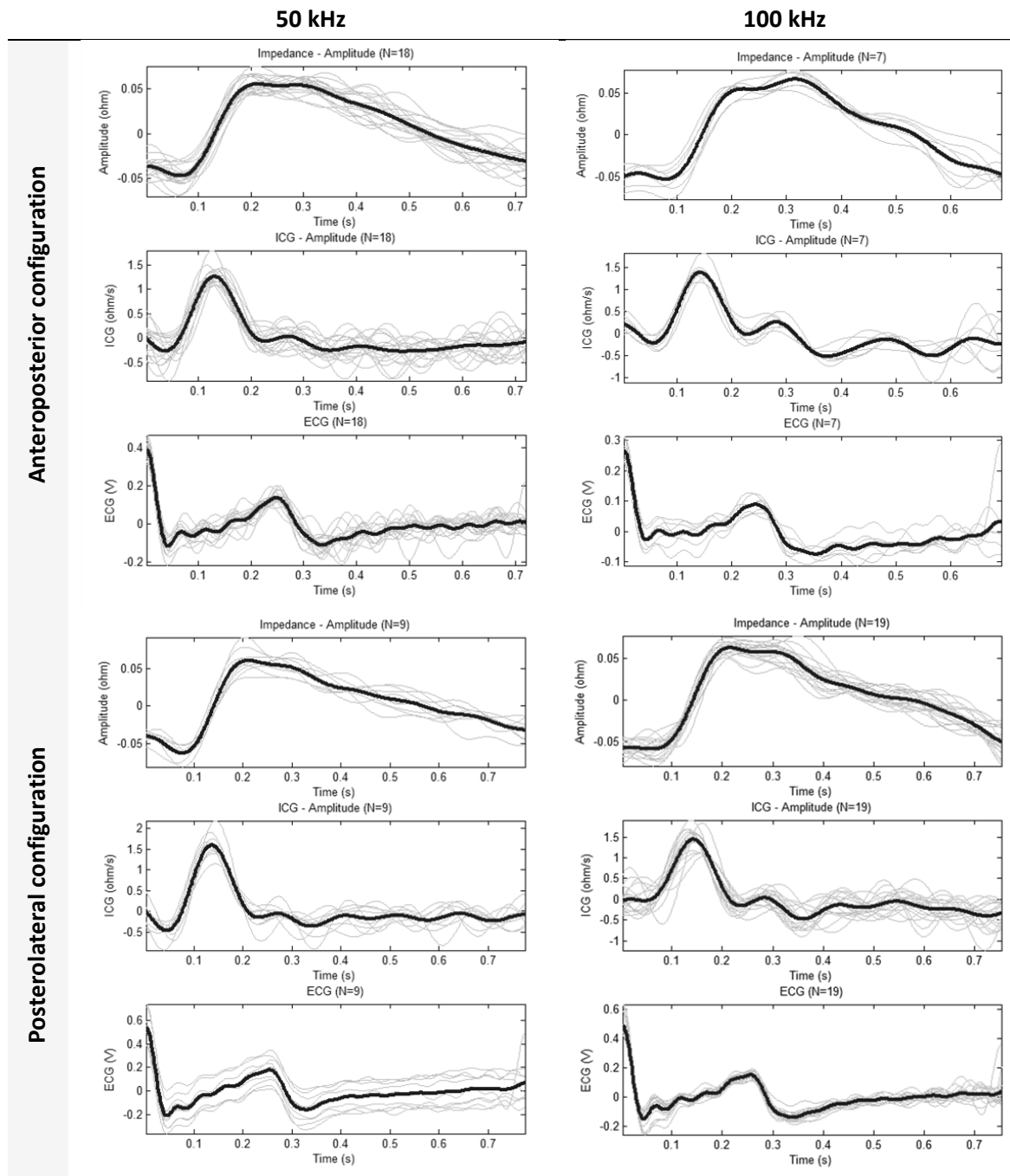


Figure 69) Averaged ICG waves based on the impedance amplitude, for different configurations and different frequencies of the excitatory AC current applied on subject #2.

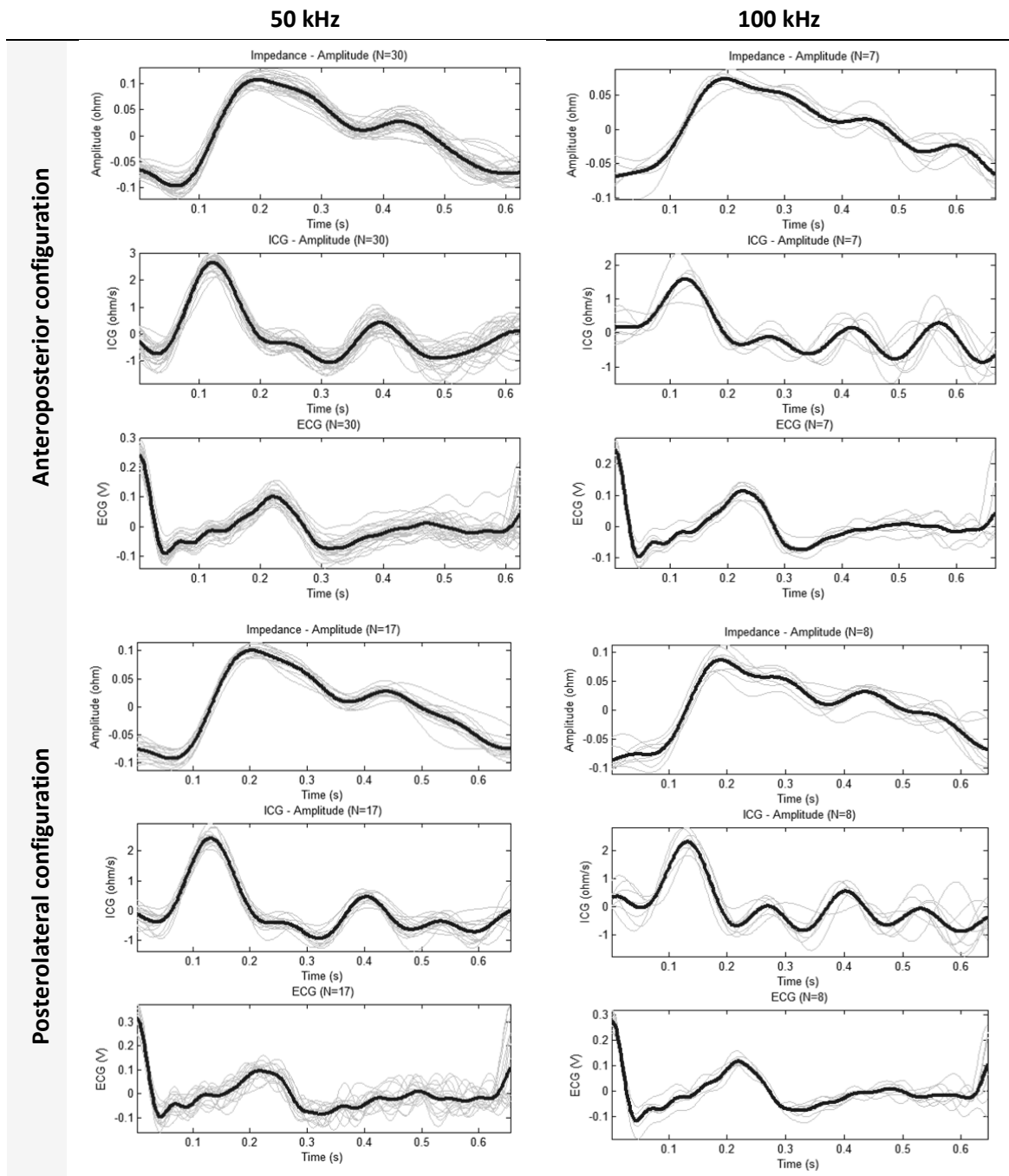


Figure 70) Averaged ICG waves based on the impedance amplitude, for different configurations and different frequencies of the excitatory AC current applied on subject #3.